

Department of Precision and Microsystems Engineering

Utilizing manufacturing-induced stresses for obtaining non-monostable compliant mechanisms

Jonathan Linsen

Report no : 2022.060
Coach : Dr.ir. G. Radaelli
Professor : Prof.dr.ir. J.L. Herder
Specialisation : Mechatronic System Design
Type of report : Thesis
Date : 19-10-2022

Utilizing manufacturing-induced stresses for obtaining non-monostable compliant mechanisms

by

Jonathan Linssen

to obtain the degree of Master of Science
at the Delft University of Technology,
to be defended publicly on Wednesday October 19, 2022 at 10:00 AM.

Student number: 4473272
Project duration: June, 2021 – October, 2022
Thesis committee: Dr. ir. G. Radaelli, TU Delft, supervisor
Prof. dr. ir. J. L. Herder, TU Delft, chair
Dr. M. J. Mirzaali, TU Delft

An electronic version of this thesis is available at <http://repository.tudelft.nl/>.

Preface

This master thesis project marks the end of my time as a student at the Delft University of Technology. And what an amazing time it has been! Over the past couple of years I experienced academic and personal growth, I built valuable friendships and I discovered that determination and perseverance can get you anywhere you want. The latter point most certainly applied to last year, during which the thesis work proved to be extremely challenging by times. I do however look back on the process with due pride. It is with this same pride that I present to you the result of my academic career via this report.

Along the way I received tremendous help and support from many people. Firstly, I would like to thank Giuseppe for all the guidance he has consistently provided over the last year. During our progress meetings many insightful discussions took place that helped us in thoroughly exploring and understanding the topics that are presented in this work. Secondly, I would like to thank the PME supporting staff for their considerable help and flexibility during the last year. Moreover, I would also like to thank my fellow students and other members of the ShellSkeletons group, who always showed interest in my work and tried to think along with the problems I encountered. Finally, I would like to thank my family and friends for their incredible support.

*Jonathan Linssen
Delft, October 2022*

Contents

1	Introduction	1
2	A study into heat-induced shrinkage of FFF printed parts for obtaining bistability	3
3	The contribution of crystallization to heat-induced shrinkage of FFF printed parts	17
4	Discussion	27
5	Conclusion	29
A	Review on the stress inducing potential of different manufacturing methods	31
A.1	Introduction	31
A.2	Method	31
A.3	Results	34
A.4	Manufacturing process assessment and selection.	36
B	The shrinkage measurement device PI-stage tests	39
B.1	The setup	39
B.2	Spring stiffness	39
B.3	Friction	40
C	The demonstrator in detail	42
C.1	Design choices & design iterations	42
C.2	APDL simulation	45
C.3	APDL code	46
C.4	Building procedure	49
C.5	Testing procedure.	49
C.6	Possible further extension of the demonstrator	50
D	G-code layer stacking in Matlab	54
D.1	Requirement of stacking file	54
D.2	Usage of the code	54
D.3	The layer_stacking.m code	55
D.4	The g-code from layer_stacking.m	59
E	Preliminary study on heat-induced material shrinkage	65
E.1	Method	65
E.2	Results	69
E.3	Differences between Prusa and Creality printers	69
F	X-Ray Diffraction diffractograms	71

1

Introduction

Compliant mechanisms (*CMs*) are flexible mechanisms in which the transmission of force, energy or motion occurs by the virtue of elastic deformations within the system. When comparing *CMs* to conventional multi-part mechanisms some considerable benefits can be found. These benefits are, amongst others, absence of backlash, absence of internal wear, high attainable precision, no need for lubrication and increased reliability [1]. *CMs* have already shown their potential in different fields of research, with the likes of aerospace engineering [2], precision engineering [3] and medical engineering [4] at the leading edge of these innovations.

CMs can show different types of stability behaviour depending on the number of static equilibrium positions that are present over the range of motion. The existence of stable positions over this range directly relates to the potential energy profile of the system; local energetic minima represent stable static equilibrium positions. The number of energetic minima over the range of motion indicates the type of the stability profile. Most *CMs* show only one such minimum. These systems are said to be *monostable*. Mechanisms with multiple stable points exist as well, e.g. *bistable* or *multi-stable* systems. A peculiar class of *CMs* is formed by mechanisms that remain in continuous equilibrium during deformation of the system. *CMs* that show this kind of behaviour are called *neutrally stable* compliant mechanisms (*NSCM*). Over the neutrally stable range these systems show no tendency of snapping into a preferred position. Rather, each position is equally favoured. During a configurational change of *NSCMs*, the total amount of potential energy remains equal. The change in configuration thus does not require any external work [5]. Due to this characteristic behaviour *NSCMs* can well be utilized as motion-facilitating devices, both on the micro [6] and macro scale [7]. All mechanisms that show more than one stable static equilibrium position over their range of motion are referred to as *non-monostable* systems in this work.

NSCMs require an internal prestress field to propagate their neutral stability [7]. Also other types of stability behaviour (e.g. some types of bistable systems) require such stress fields for their specific stability profile. The application of prestress to *CMs* during assembly is found to be almost exclusively induced by manual actions [7–9]. These manual operations have a negative influence on both the production consistency as well as the production throughput. As indicated in literature, functional prestress proves to be a difficult factor to incorporate in mass production processes [10]. Moreover, this manual way of applying prestress poses problems onto the geometrical freedom that designed parts can have. Current methods of applying prestress are found to be very case specific and they do not show much flexibility towards application in other geometries [11]. The manual way of prestress application furthermore poses implication on the dimensional scalability of parts. This is especially prevalent when going to small scales; hand-operated prestressing actions are only feasible up to a certain scale and size. *CMs* with a tailored stability profile could be of tremendous relevance for developments within the precision industry [12]. Dimensional scalability is hereto evidently an important contributing factor.

From the above mentioned remarks a desire arises to have an accurate and scalable method with which a prestress profile can be imposed onto a monostable *CM*. With this imposed prestress, the structure could then permanently be morphed into a mechanism with non-monostable stability behaviour. To solve the

aforementioned issues, additional prerequisites for this new prestressing method entail a sufficient degree of design freedom and the ability to operate at different dimensional scales. A possible solution to this is formed by utilization of inherent features of the manufacturing method with which a part is created. Accuracy, repeatability and design freedom will then be directly dictated by the limits of the production method, rather than by limits of the designer or the assembly process. The feasibility of utilizing manufacturing-induced stresses for obtaining non-monostable compliant mechanisms is investigated in this thesis project. In conventional production methods the introduction of stresses during manufacturing is generally considered to be a negative by-effect of the process [13–15]. In this work the existence of these stress-inducing mechanics will rather be exploited to add functionality to the parts that are produced. From a preliminary study, which is included in appendix A of this report, Fused Filament Fabrication (*FFF*) appeared to be an especially suitable production method in this regard. By using *FFF*, significant stresses (and therewith strains) can be obtained when introducing heat to the parts after printing. This project therefore specifically focusses on imposing prestress onto parts that are created with the *FFF* production method. The prestress field will solely be acquired by the combination of adjusting process parameters, together with the introduction of heat to the part after printing. The goal of this thesis is to build the foundation for a method with which systems can acquire a predefined internal stress field. This stress field is ought to permanently change the stability behaviour from monostability into non-monostability. The results of this project should form the onset for the further creation of multi- and neutrally stable compliant mechanisms in different geometrical form factors and on different dimensional scales.

In chapter 2 the use of heat introduction as a means to obtain variable thermal shrinkage strain in *FFF* printed parts is presented. This variable thermal material shrinkage is, when applied properly, able to induce prestress to selected regions of the part. Herewith a change in the stability profile of the systems under consideration can be achieved. In chapter 3 a more fundamental approach to the polymer mechanics that cause the heat-induced material shrinkage is presented. By understanding what mechanics contribute to this shrinkage behaviour, the prestress inducing method can be tailored with a focus on the factors that are of major influence on the shrinkage behaviour. Chapter 3 mainly serves the purpose of broadening the general understanding of the principles at play. In chapters 4 and 5 the discussion and conclusion are presented respectively. In the appendices supplementary material to chapters 2 and 3 is provided. Also a review on the (pre)stress inducing potential of different manufacturing methods is included in the appendix.

2

A study into heat-induced shrinkage of FFF
printed parts for obtaining bistability

A study into heat-induced shrinkage of FFF printed parts for obtaining bistability

Jonathan Linssen

Giuseppe Radaelli

Just Herder

Abstract - When a PLA Fused Filament Fabrication (FFF) printed part is exposed to a temperature higher than the glass transition temperature, it will show significant material shrinkage. Moreover, over this shrinkage range the PLA is able to deliver mechanical work. This phenomenon can be used as a method to induce prestress onto a printed part. Herewith a compliant mechanism with a bistable or neutrally stable stability profile can be obtained from a monostable part. The shrinkage magnitude and the delivered work are both directly dependent on several design parameters. In this paper the influence of the printing speed, geometric variables and the post-process heating time and temperature on the shrinkage behaviour is investigated. All parameters are found to show increasing shrinkage magnitudes for increasing parameter values. Maximum attainable shrinkage values of over 20% are found. When subjected to a resisting force, shrinkage values of 2% could still be obtained. Practical applicability of this method is shown by realising a permanent monostable-to-bistable stability switch in a demonstrator mechanism.

Index terms - Fused Filament Fabrication, compliant mechanism, stability, shrinkage, PLA

1. Introduction

Compliant mechanisms (CMs) are flexure-based mechanisms in which the transmission of force, energy or motion occurs by the virtue of elastic body deformations. CMs can show different types of mechanical stability behaviour. This behaviour is oftentimes monostable [1–4], but it can e.g. be bistable [5–7], multi-stable [8–10] or neutrally stable [11–13] as well. This stability notion directly refers to the number of possible system configurations in which the system sits in a local energetic minimum. As long as the system statically resides in such a minimum there is no tendency to leave its current configuration; the local energetic minimum presents a stable static equilibrium position. For a monostable system only a single energetic minimum can be found over the allowable range of motion. For bistable systems two such minima are found. The numeral stability prefix thus indicates the amount of energetic minima that are present over the range of motion.

Obtaining a neutrally stable stability profile or a bistable stability profile in which the two energetic minima are of equal magnitude (from here onwards called *symmetrically bistable*) within the realm of CMs requires the presence of an internal or external prestress profile. Moreover, to enable shifting through the different stable positions, a system is ought to have the geometrical freedom and compliance to al-

low for the deformational motion that accompanies this shift. The latter factor can well be designed for. The former factor on the contrary poses a problem of implementation; prestress generally is a complex factor to controllably add to mass fabrication processes [14]. The plethora of available literature on non-monostable CMs shows that, during assembly, prestress is nearly exclusively applied in a manual manner [11, 13, 15].

Additive manufacturing (AM) methods, also known as 3D printing methods, are an often used technique for producing CMs [16–20]. Benefits of AM in comparison to conventional subtractive manufacturing methods such as milling and lathing are, amongst others, the freedom of design, the minimization of waste material and the low production cost of customized parts and prototypes [21]. AM comprises of many very different production methods. Of these methods Fused Filament Fabrication (FFF), also known by the commercial name Fused Deposition Modelling™ (FDM), is an especially popular method. FFF is used both for rapid prototyping purposes as well as for industrial production purposes [22]. Its grand popularity is underlined by the fact that FFF held a total market share of 31% amongst all AM technologies in 2021 [23]. FFF is a melt extrusion based printing method in which a thermoplastic polymeric filament is melted and deposited onto a print bed. After deposition the material swiftly re-solidifies [24]. By letting the printing nozzle sequentially move in the three Cartesian directions, a 3-dimensional geometry can be composed in a layer-by-layer fashion.

Parts that are produced by FFF have mechanical and thermal material properties that are inferior to the bulk material properties [25–28]. A way of significantly improving these material properties is by post-process annealing of the workpieces [29, 30]. Besides improving mechanical and thermal properties due to this annealing, as a side-effect also significant material shrinkage is observed [31–33]. As the shape, dimensions and tolerances of the workpiece are strongly affected by annealing, this post-processing step should only be considered when the improvement of material properties is of higher priority than the correctness of geometrical tolerances. Although the occurrence of heat-induced shrinkage for FFF printed parts is often unwanted, it also presents an interesting opportunity for thermally induced shape-shifting behaviour. New engineering domains such

as 4D printing delve deeper into the possibilities of adding stimulus responsive elements to 3D printed parts with the goal of adding time-dependency to the printed workpieces [34]. In the work by Rajkumar and Shanmugam [35] the possibility of applying a thermally actuated shape-transformation in several FFF printed thermoplastics is explored. These shape-transformations cover both 1D to 2D and 2D to 3D transformations successfully. In this work a qualitative relation between the printing speed, printing direction and the thermally induced shrinkage strain is found. This very relation is also mentioned in the work by Zhang et al. [36,37]. Zhang et al. attribute the specific shrinkage behaviour to the combination of shape memory capabilities of polymeric materials, together with filament-nozzle interactions that come into play when printing these materials. In their work a bi-layer material, consisting of sheet paper and FFF printed Polylactic Acid (PLA), is presented that is able to deform from a planar sheet into a 3D geometry. Shape-shifting is activated by an elevated temperature that makes only the PLA layer shrink. Since the paper remains as is, the result is out-of-plane bending of the bi-layer material. Wang and Li [38] successfully created a computational simulation of the pre-programmed shape memory behaviour of FFF printed PLA by utilizing a 1D shape memory polymer (*SMP*) constitutive model. To underline the simulation's quality, several actual temperature-induced folding origami structures are created for comparison. These structures showed strong correspondence to the simulation results. Van Manen et al. [39] use temperature changes as a trigger to alter the shape of flat material into a pre-programmed 3D shape. The parameters used to dictate the magnitude and form of the shape-shift are the directional stacking of printed layers as well as the width and thickness of the printed strips.

Kačergis et al. [40] researched the influence of several FFF process parameters on the shape-shifting behaviour of PLA and TPU structures. When exposed to heated water, the shape memory of these structures is activated, consequently resulting in the shape-shift. Variations to the printing speed, the build plate temperature and the number of active layers were made. All three parameters showed an increasing shrinkage magnitude for increasing parameter values. Also An et al. [41] showed the direct influence of printing speed as a determining factor for the magnitude of heat-induced shrinkage of FFF printed parts.

All of the aforementioned literature finds common ground in the occurrence of (partial) material deformation when exposed to heat. Although shrinkage figures of up to 25% [36] are reported on, and even though the overall shrinkage potential seems rather significant, all literature that is found on this topic is limited to deformational paths in which only the gravitational field of the structure itself needs to be

overcome. This oftentimes is not more than just the weight of a thin sheet of polymeric material. This gives rise to the question whether the true and full potential of thermally-induced material shrinkage of FFF printed parts has yet been established. When material shrinkage can deliver significant amounts of work, combined with the possibility of imposing variable shrinkage magnitudes over the volume of a workpiece, predefined prestress profiles could be imposed onto FFF printed parts. With this method at hand, neutrally stable and symmetrically bistable compliant mechanisms can be produced in which no manual prestressing step is required during assembly. This will evidently result in both increased production consistency of the mechanisms, as well as an increased production throughput. When successful, this technique will prove itself useful to a whole variety of compliant mechanisms with tailored stability behaviour.

The objective of the current work is therefore to identify both the maximally attainable material shrinkage, as well as the maximum force-delivering potential of FFF printed material that is heated. To investigate how both factors can be maximized, the influence of multiple design parameters on the heat-induced shrinkage magnitude of FFF printed parts is examined. From this investigation an optimum parameter set will follow with which a maximum shrinkage yield can be obtained. The eventual goal of the here investigated method is to utilize heat-induced material shrinkage as a means to apply prestress to monostable systems, such that they permanently morph into neutrally stable or symmetrically bistable compliant mechanisms. To emphasize the strong focus on applicability, included in this work is the demonstration of a permanent monostable-to-bistable stability alteration for a rotational compliant mechanism.

2. Method

The material that is used throughout this study is PLA. It is a cheap, accessible and easy to print biodegradable material that possesses the required *SMP* property. Due to its semi-crystalline nature, PLA has pronounced transition points for both the glassy-to-rubbery state transition (glass transition temperature T_g of around 50°C - 60°C [42]) as well as for the rubbery-to-rubbery liquid state transition (melting temperature T_m of about 170°C - 180°C [42]). These relatively sharp transition points will show their usefulness for enabling ($T > T_g$) or disabling ($T < T_g$) the shape memory effect.

Several tests are performed to investigate the shrinkage behaviour of FFF printed PLA in reaction to post-print material heating. The testing goals are twofold; the results are ought to reveal the importance of a variety of design parameters on the shrinkage behaviour, as well as showing the potential of this shrinkage behaviour as a means to apply prestress to a

mechanism. Following this dual research objective the current investigation is split up into two sections. In section 2.1 the influence of several design parameters on the PLA shrinkage magnitude is analysed. Section 2.2 builds upon the results of section 2.1; here the gained knowledge is used to transform a monostable geometry into a symmetrically bistable compliant mechanism by application of shrinkage-induced prestress.

2.1. Parameter testing

The influence of 4 different parameters on the heat-induced shrinkage magnitude and the force-delivering potential of PLA is investigated. Testing is done through parameter variations on FFF printed samples. The parameters that are examined are the printing speed, the heating temperature, the heating time and the cross-sectional area of the printed samples. Cross-combinations of parameter variations are not explicitly explored.

2.1.1 Measuring device

To measure the shrinkage of each sample in a consistent manner, a slider mechanism is created. This mechanism functions as a guiding frame for the shrinking samples. Moreover, the mechanism allows for easy shrinkage measurements. To this slider mechanism compression springs can be attached to provide stiffness in the axial direction. The slider mechanism, both with and without springs, is shown in figure 1. Also the name convention used to indicate the three perpendicular shrinkage directions with respect to this measuring device is shown in the figure.

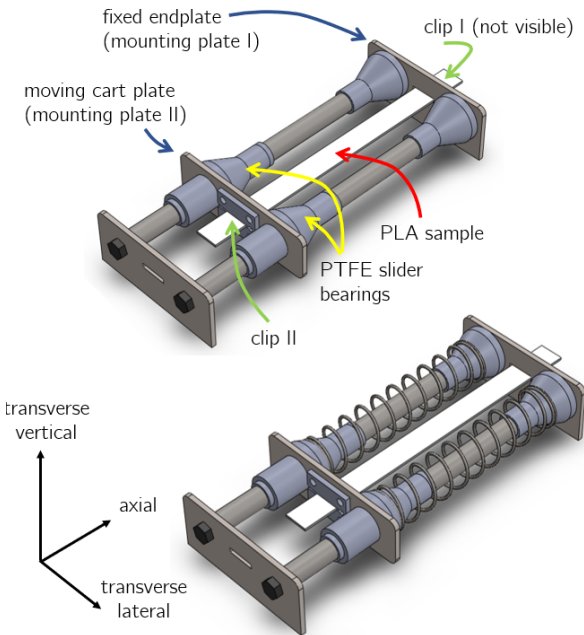


Figure 1: Shrinkage measurement test device, without attached springs (top) and with attached springs (bottom).

In the slider mechanism samples are clamped be-

tween a fixed steel endplate and the steel sliding cart, see figure 1. These two plates will be referred to as the *mounting plates* from here onwards. Clamping is realised by adding steel clips with a slightly undersized slit to both ends of the PLA sample on the outside of both mounting plates. Friction between the sample and the clip holds the sample in place, even under heat-induced deformation. Since the cart slides over the steel guiding rails, sleeve bearings are added to the system. These bearings should provide low amounts of both static and dynamic friction. Furthermore they should withstand temperatures that can go as high as the melting point of PLA (170°C), above which no measurements will be performed. PTFE matches both requirements and is chosen as the bearing material. The PLA samples are inserted in the test device such that they pull the cart in its exact centreline. This minimizes the risk of mechanical jamming. Springs of various diameters can be mounted on the conical spring beds that are present at both mounting plates.

Any functional non-monostable compliant mechanism that will be prestressed in the way as proposed in this work will experience internal forces that originate from the in compression loaded (prestressed) members. These forces are transferred internally and impose tension on the shrinking members of the mechanism. The magnitude of the exerted tensile force is dependent on the geometric design of the to be prestressed members, as well as on the Young's moduli of the materials used. To include the effect of exerted forces on the shrinking PLA samples in the measurement test device as well, compression springs can be attached to the test device to provide a linear force profile directed oppositely to the shrinkage direction. The springs that are used during testing have an equivalent parallel spring stiffness of 0.158 N/mm . This stiffness is chosen such that it roughly corresponds to the axial buckling stiffness of the demonstrator model that will be introduced in section 2.2. Both the linearity and the stiffness of the springs have been validated by tests on a PI M-505 translational stage (Physik Instrumente GmbH & Co. KG, Karlsruhe, Germany) combined with a LSB200 low capacity load cell (FUTEK Advanced Sensor Technology, Inc., Irvine, CA, USA).

When a sample is inserted in the measurement test device, a lengthwise measurement prior to heating is done. With this measurement the normal distance between the opposing inside faces of the mounting plates is measured with a digital calliper. After this measurement, the shrinkage measurement device (including sample) is put in a preheated oven for a duration that matches the duration of the respective test. When the total heating time has passed, the device is taken out of the oven and a post-heating measurement is performed in the same manner as the pre-heating measurement. This measurement is done directly af-

ter heating, i.e. the system has not cooled down yet. When no springs are attached to the test device, the distance between the mounting plates is the only distance that needs to be measured post-heating. When springs are attached there might be the possibility of a partial retraction of the cart due to the push back force exerted by the springs. As heating of polymeric material to a temperature higher than T_g generally weakens the material’s stiffness significantly [43], the system might reach a turning point within its heating time at which the spring force exceeds the sample’s contracting force. This then results in re-stretching of the shrunk material. At the end of the heating cycle this yields a net observed shrinkage that is lower than the maximally attainable shrinkage. To be able to keep track of the maximum achieved shrinkage, additional sliding rings are added to the guiding rails on both sides of the cart. These rings are shown in figure 2. The rings are pushed to the extreme positions of the cart. There is only a coupling in the pushing direction. The rings will therefore remain in the extreme positions, even though the cart may have moved backwards. To report on both the maximally attained shrinkage and the net observed shrinkage, `shrinkage max` and `shrinkage net` (see figure 2) are both recorded. The sliding rings are not directly pushed forward by the mounting plates, but rather by the extended sleeve bearings. This distance must be corrected for as to convert the shrinkage values to the actual sample shrinkage values.

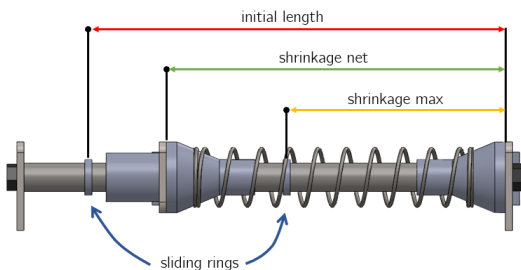


Figure 2: Measurement indicators: sliding rings indicate extreme values (i.e. initial length and shrinkage max).

2.1.2 Samples

All samples are printed with an Ender 3 Pro 3D printer (Shenzhen Creality 3D Technology Co, Ltd., Shenzhen, China). The default flexible print bed is interchanged for a tempered glass print bed. This is done to both enhance the bed levelling procedure as well as increasing filament adhesion. To fully exclude the potential influence of colouring agents on the shrinkage behaviour a natural 1.75 mm PLA filament type is used (DAS FILAMENT, Emskirchen, Germany). Generation of the g-code of the bottom layer of the sample is done in PrusaSlicer (version 2.4.2 - Prusa Research, Prague, Czech Republic). To obtain the g-code that corresponds to the complete sample, a self-build Matlab script is used that copies and stacks

the g-code of this first layer for a set amount of instances. The resulting g-code corresponds to a sample of rectangular shape. The infill pattern is set to *parallel rectilinear* such that all filament lines are deposited collinearly. From literature it has become evident that deposited filament lines have one dominant shrinkage direction when being exposed to heat. This direction is referred to as the *major shrinkage direction*. The shrinkage magnitude of this direction far exceeds the shrinkage magnitudes of the two other directions (the *minor shrinkage directions*). The major shrinkage direction of a filament line is collinear with the print direction [31]. For this reason it must be ensured that the rectilinear printing pattern is set parallel to the axial direction (i.e. the only degree of freedom in the measuring device), as defined in figure 1. During measurements only the shrinkage corresponding to the major shrinkage direction is recorded.

Each sample has a variation in one of the 4 parameters that are considered in this work. All parameter variations are applied to a baseline sample design of which the design parameters are shown in table 1. The geometric baseline parameters are chosen such that the samples properly fit in the test device. The printing parameters are set according to the default PLA printing values as provided by the PrusaSlicer software. The heating parameters are chosen based on preliminary test results.

Table 1: Baseline sample design parameters.

Parameter	Value
Width	10 mm
Height	2 mm
Length	130 mm
Printing speed	60 mm/s
Bed temperature	60°C
Nozzle temperature	215°C
Infill density	100%
Infill pattern	parallel rectilinear
Fan speed	0%
Heating time	75 s
Heating temperature	110°C

2.1.3 Testing

Heating of the samples is done in a Silvercrest 9-in-1 Airfryer. This heating device is chosen for its broad operational temperature range (40°C to 200°C). This low-budget oven does not provide an external temperature readout, hence a digital oven thermometer (Hot-loop, Chongqing Lainike Network Technology Co., Ltd.) is added to monitor, and if necessary manually adjust, the oven temperature.

The parameter variation is split up in 4 separate sequences. The varied parameters and the setpoints per test sequence are shown in table 2. The upper and lower limits for the printing speed parameter are based both on limits provided by the printer manufacturer, as well as on observations regarding print quality done during preliminary testing. The range

of the heating temperature is prescribed by the PLA T_g at the lower limit and the T_m at the upper limit. The heating time starts at a value of 30 seconds and is roughly doubled for each subsequent setpoint in order to capture both short-time heating effects as well as long-time heating effects. The cross-sectional area starts at a value of 1 mm^2 . As small cross-sectional areas are of most interest for this study, the focus is on areas $\leq 20 \text{ mm}^2$. To also capture shrinkage behaviour of larger cross-sectional areas two additional setpoints of 50 mm^2 and 100 mm^2 are included. As the samples corresponding to the latter two areas have a significantly longer thermal penetration depth, samples with these areas are kept in the oven for as long as shrinkage is visually observed. This differs from the default heating time as presented in table 1. To still be able to draw general conclusions about the influence of the cross-sectional area, only **shrinkage max** (see figure 2) will be reported on. By not accounting for **shrinkage net**, the heating time-dependence is automatically excluded from the results.

Table 2: Variations on the baseline sample design (see table 1) per test sequence. The values shown in **bold** correspond to the baseline default values.

Seq.	Variation	Setpoints
1	Printing speed [mm/s]	5, 15, 30, 45, 60 , 75, 90, 105
2	Heating temperature [$^{\circ}\text{C}$]	50, 80, 110 , 140, 170
3	Heating time [s]	30, 75 , 150, 300, 600, 1200, 2400
4	Cross section [mm x mm]	1x1, 5x1, 10x1, 10x2 , 10x5, 10x10

Each setpoint as shown in table 2 will be tested both with and without springs attached to the testing device separately. This is done to give insight in the maximum attainable shrinkage of the material as well as showing the realistic shrinkage one can obtain when prestressing a system that has a linear stiffness profile. The axial shrinkage of the PLA samples is directly calculated from the pre- and post-heating measurements. In order to get statistically sound results a minimum of 4 samples per setpoint is used over which the results are averaged.

2.2. Demonstrator

To show that heated FFF printed material indeed has the ability to induce prestress onto a compliant mechanism such that the stability behaviour is altered, a demonstrator mechanism is here proposed. This mechanism should demonstrate a permanent transformation of its stability profile from monostable to bistable, solely obtained by heat-induced shrinkage of a PLA member.

2.2.1 The demonstrator design

Switching through stability states by using active materials has been researched by Ahmad [44]. The demonstrator used in the current study is based on the CANS-J prototype as mentioned by Ahmad. Modifications are made to this design to improve both its

general behaviour as well as making it comply with the requirements and boundaries of the current study.

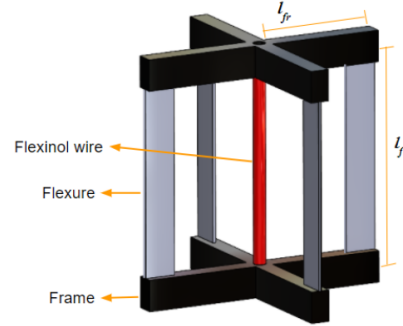


Figure 3: The CANS-J prototype as proposed by Ahmad [44]

The CANS-J prototype is shown in figure 3. In this design both ends of 4 separate leaf flexures are glued onto two FFF printed PETG cross-like rigid frames. Between both crosses' centres, a flexinol wire is mounted that is able to contract under the influence of electric current. When contracting, the flexinol wire exerts a compressive force onto the leaf flexures via the frame. If this force surpasses the critical buckling load of the 4 combined leaf flexures, simultaneous buckling of the flexures will occur. As a result a relative rotational motion between the two crosses around the centreline is observed.

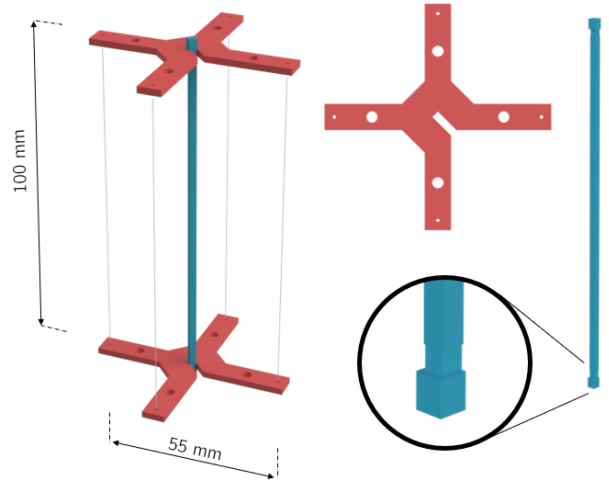


Figure 4: L: CAD render of the demonstrator - steel laser cut crosses in red, wire flexures in black, PLA beam in blue. M: Top view of laser cut steel cross. R: PLA sample with magnified view of the extruded end.

PETG is a polymeric material which means that it loses stiffness when heated above its T_g of roughly 80°C [45]. To exclude potential influences of heat-induced structural weakening when putting the demonstrator in the oven, the PETG crosses are replaced by laser cut steel crosses of thickness 2 mm. These steel crosses are indicated by the red areas in figure 4. In the centre of these crosses a slit is cut in which a printed PLA beam sample (blue in figure 4) can be inserted. The PLA samples are printed

parallelly rectilinear in the longitudinal direction of the sample, such that the major shrinkage direction aligns with this longitudinal direction. The PLA sample has widened extrusions at both ends such that the sample does not slide through the slit during material shrinkage. The leaf flexures of the CANS-J have been substituted for spring steel wire flexures of length 0.1 m and diameter 0.3 mm. By this substitution the rotational resistance under buckling of the demonstrator reduces due to the axisymmetric shape of the wire flexures, herewith eliminating a specific preferred buckling orientation. To prevent temperature-induced glue failure from happening, heat resistant cyanoacrylate glue is used that has an operational range up to at least 135°C (MESA products, Almelo, The Netherlands).

The spring stiffness of 0.158 N/mm that is used in the shrinkage measurement test device of section 2.1 approximates the secant buckling stiffness of 4 parallelly connected spring steel wire flexures of length 0.1 m and diameter 0.3 mm. From finite element modelling, on which an elaboration can be found in section 2.2.3, this secant stiffness is found to be 0.195 N/mm. Due to limited availability of compression springs in this stiffness range, a parallelly connected spring combination with an equivalent spring stiffness of 0.158 N/mm was deemed the best option for the measuring device.

2.2.2 Testing

Before testing of the demonstrator takes place, first the printing and heating parameters will need to be chosen. This choice will be based on the results of the parameter testing. The goal is to find the combination of design parameters that yields the highest bistable range of motion (i.e. highest axial PLA shrinkage), while still having sufficient compliance to allow for the rotational motion. When parameter values are determined, the PLA samples can be printed and inserted into the demonstrator. The longitudinal sample length is also measured in this step. Hereafter the demonstrator is put upright in a preheated oven for a heating time that also follows from the parameter testing. To prevent tipping over during heating, the demonstrator is put in a cylindrical glass with a slightly larger internal diameter than the outer diameter of the crosses. When the heating time has passed, the demonstrator is removed from the oven and both the sample length as well as the now existing relative rotation angle between the crosses is recorded. As a next step the demonstrator is put in a ZwickRoell Z005 torsion machine (ZwickRoell GmbH & Co. KG, Ulm, Germany) with which the moment-angle curve of the system is measured. The complete procedure is executed for a second -identical- PLA sample as well. The demonstrator as clamped in the torsion machine is shown in the left picture of figure 5.

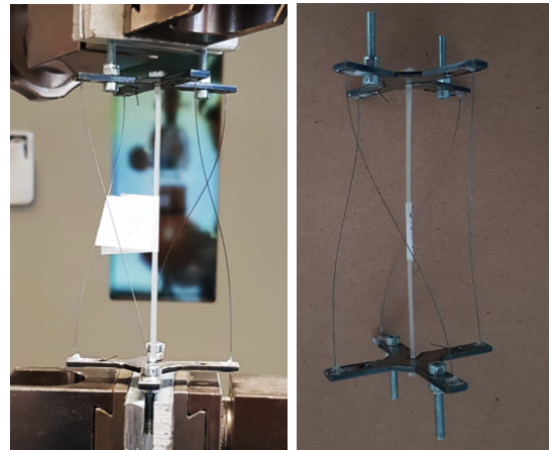


Figure 5: L: Demonstrator clamped in the ZwickRoell Z005 torsion test machine. N.B. the white paper label contains the sample number and is not functional. R: The demonstrator when taken out of the oven.

2.2.3 Finite element simulation

A finite element (FE) simulation of the shrinkage behaviour and the bistable snap-through path of the demonstrator is made. This simulation allows for a comparison between the results from the torsion tests and the FE results. Moreover, it will provide a means to establish the secant buckling stiffness, and it can be used to predict the general kinematic behaviour of the demonstrator. The simulation is done in the ANSYS APDL software (version 2021 R2 - Ansys, inc., Canonsburg, PA, USA).

The goal of this simulation is not to model the polymer shrinkage behaviour on a fundamental level, as is for instance done in [46]. Instead, the material shrinkage is imposed on the PLA middle beam, hereby forcing a relative rotational motion between the top and bottom crosses. In this manner the kinematic demonstrator behaviour is simulated. The simulation is performed fully in the mechanical domain. Heat-induced PLA shrinkage is realised by assigning a coefficient of thermal expansion (CTE) to the PLA alone; for the steel parts the CTE is set to 0. In the first simulation step the ambient temperature is lowered, resulting in PLA shrinkage only. As a consequence of the PLA shrinkage, the wire flexures will be prestressed. This results in flexure buckling when the critical buckling load is exceeded. After buckling the simulation proceeds to the next step, where the rotational snap-through behaviour of the now bistable demonstrator is simulated.

In this simulation 2-node beam elements (BEAM188 elements) are used. Geometric non-linearity is accounted for while the materials are assumed to be linear. Even though the geometry does allow for the use of symmetry planes to reduce computational time, the full geometry is modelled as the computation time was not significant. The assigned material properties and a depiction of the

FE model are shown in figure 6. The steel elements are modelled isotropically whereas the printed PLA element is modelled as a transversely isotropic material, adhering to the constitutive relation as given by Yao et al. [47]. Material properties for PLA are obtained from the work by Song et al. [48]. KeyPoint 1 in figure 6 is constrained in all translational and rotational directions. KeyPoint 2 has freedom in both the translational and rotational Z-direction. All other degrees of freedom are constrained for this point. The indicated CTE values for PLA (α_x , α_y and α_z) are calculated values with which a desired PLA shrinkage magnitude is obtained during the simulation. These values do not correspond to the actual CTE values of PLA.

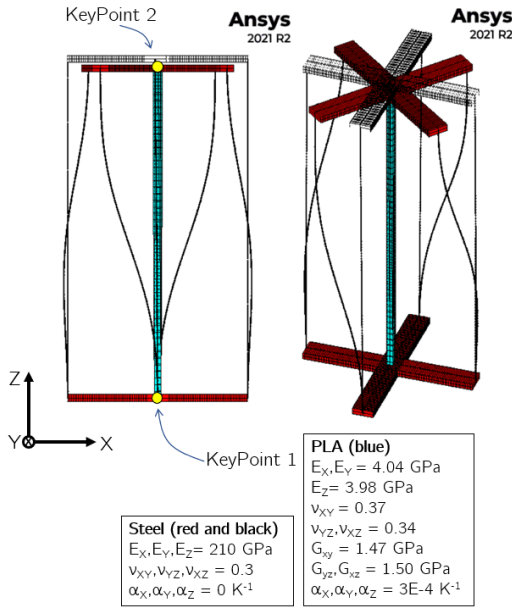


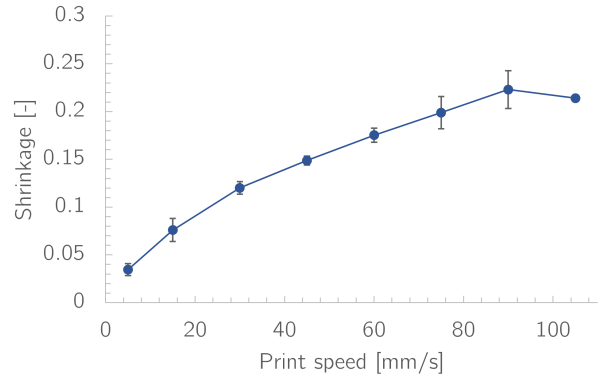
Figure 6: The undeformed (wireframe) and deformed (solid) ANSYS simulation results of the demonstrator model. L: side view of model. R: Oblique view of the model. B: Material properties used in the model - E_i = Young's Modulus, ν_{ij} = Poisson's ratio, G_{ij} = shear modulus, α_i = CTE.

3. Results

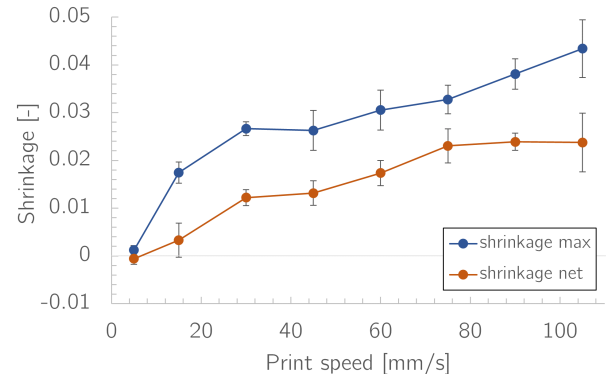
3.1. Parameter testing

The first parameter that is varied is the printing speed. In figure 7 the results are shown for both the case where no springs are attached (i.e. not loaded - figure 7a) as well as the case where springs are attached (i.e. loaded - figure 7b). For the latter case two separate result sequences are shown; **shrinkage max** and **shrinkage net**. As already briefly explained in section 2.1 **shrinkage max** shows the maximum shrinkage that is attained over the course of heating. This can be considered to be the upper limit of the shrinkage potential of the PLA when an equivalent spring stiffness of 0.158 N/mm is attached. **Shrinkage net** shows the eventual shrinkage at the end of the heating cycle. Here re-elongation due to the combined effect of temperature induced stiffness

reduction and an applied stretching force may have lowered the shrinkage value. In figure 7b it is observed that the error bars increase significantly at a print speed of 105 mm/s. During the printing process it is observed that samples printed with this print speed show significantly worse layer-to-bed and layer-to-layer adhesion. Moreover, printing speeds of over 100 mm/s are, albeit technically possible, discouraged by the manufacturer of the used 3D printer. The increase in shrinkage magnitude scatter at 105 mm/s is not visible for the case where no springs are attached (figure 7a). The maximum **shrinkage max** value in loaded configuration occurs at either 90 mm/s or 105 mm/s. Due to the overlapping $\pm\sigma$ no single highest value can be appointed here. The shrinkage value at 90 mm/s does have a significantly lower spread than the results at 105 mm/s. Based on the results there seems to be a clear correlation between an increasing print speed and the increase in resulting axial shrinkage magnitude for both the cases with and without attached springs. For both **shrinkage max** and **shrinkage net** this trend becomes more ambiguous from a printing speed of 30 mm/s onwards; even though the average shrinkage values still increase, the $\pm\sigma$ of these results increase in size and start overlapping. When comparing the **shrinkage max** values of the loaded case with the shrinkage values of the not loaded case, the shrinkage magnitude is roughly a factor 5 lower for all setpoints.



(a) Shrinkage without added spring stiffness - i.e. not loaded



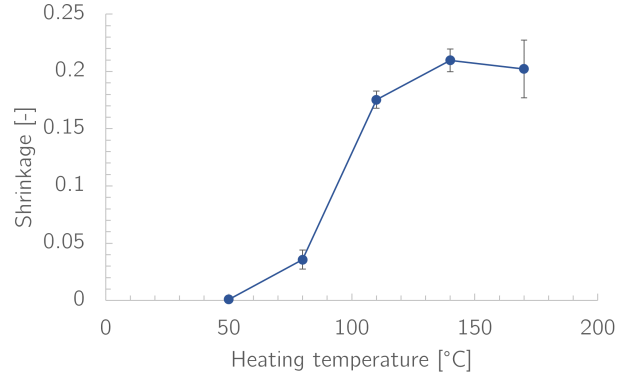
(b) Shrinkage with added spring stiffness - i.e. loaded

Figure 7: Axial material shrinkage as a function of the printing speed.

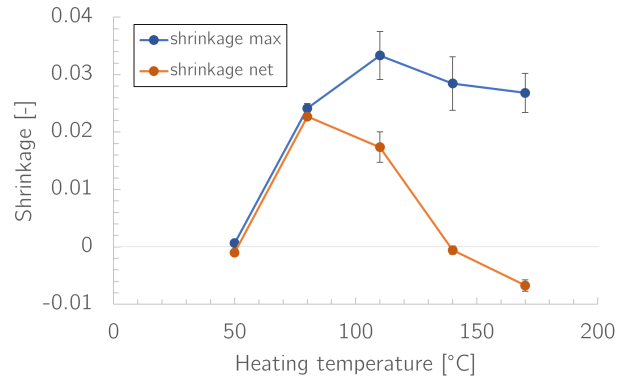
Figure 8 shows the results that are obtained by varying the heating temperature. During this process it is observed that samples that are heated up to 170°C are at the upper limit of the rubbery range. As the samples are close to the turning point of becoming a rubbery liquid polymer, extreme sag is observed under the influence of its own weight. It can be seen that this state change around 170°C has influence on the scatter of the shrinkage magnitude in figure 8a. The **shrinkage net** in figure 8b is found to be lower than 0 for a heating temperature of 170°C . This negative shrinkage is also attributed to the extreme sag during the heating cycle. First, the force delivered by the springs re-stretches the shrunk PLA sample to a net shrinkage of 0. As the increasingly sagging material hereafter starts to touch the oven's bottom plate, the moving cart is pushed slightly further than the zero shrinkage point, yielding a negative shrinkage. This negative shrinkage is thus no result of internal polymer interactions. In the loaded setting the maximum **shrinkage max** is found at 110°C . For **shrinkage net** it can be observed that at 140°C the shrinkage goes back to 0. At 50°C no shrinkage is observed for the cases both with and without attached springs as this temperature is most likely still below T_g , albeit marginally. At this temperature the material does not enter the rubbery state and the shape memory is not activated. Both in the loaded and not loaded case there is an increasing shrinkage magnitude for an increasing heating temperature. From 110°C onwards a plateau is observed within the $\pm\sigma$ ranges, indicating that the maximum attainable shrinkage was reached. For temperatures higher than 80°C , **shrinkage net** values start to deviate from the **shrinkage max** values. When comparing shrinkage of the not loaded case with **shrinkage max** of the loaded case, it is observed that the mutual relationships are more intricate than for the printing speed results. Here no single scaling factor can be appointed that approximately relates the shrinkage results of each mutual setpoint in both cases.

In figure 9 the results from the variation in heating time can be found. Maximum shrinkage in the not loaded case can be found after 150 s, after which the results seem to reach a plateau. In the loaded case **shrinkage max** also is at its maximum after 150 s of heating time. The data points higher than 30 s of heating time show a strong reduction in **shrinkage net** magnitude. The heating time thus seems to be an important parameter to set correctly in order to obtain and maintain a maximum shrinkage yield.

Figure 10 presents the results for variations in the cross sectional dimensions. In figure 10b **shrinkage net** is not displayed. The reason for this is provided in section 2.1.3. In figure 11 the shrinkage magnitude results are shown again, now grouped on their minor cross-sectional dimension. For the unloaded case, as shown in figure 10a, initially the shrinkage strongly



(a) Shrinkage without added spring stiffness - i.e. not loaded



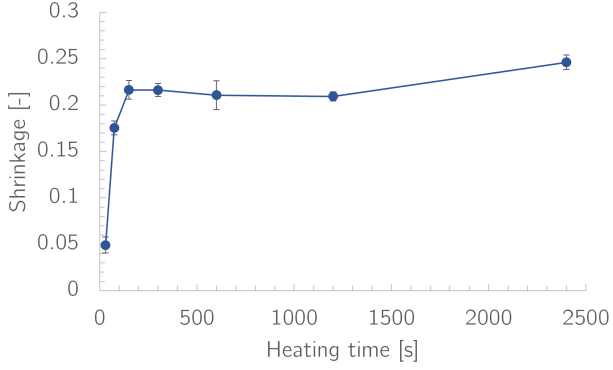
(b) Shrinkage with added spring stiffness - i.e. loaded

Figure 8: Axial material shrinkage as a function of the heating temperature.

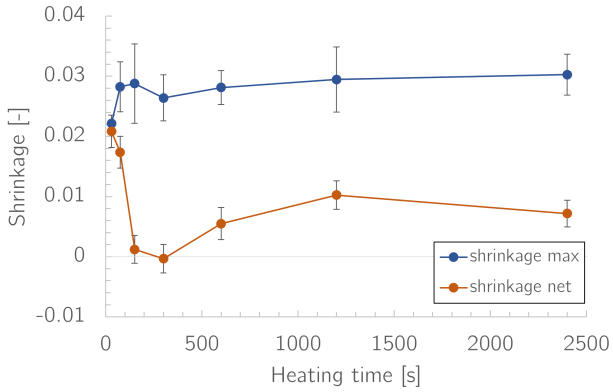
increases up to a maximum point of just over 20% shrinkage for a cross-sectional area of 10 mm^2 . After this point, a gradual decline of the shrinkage magnitude for increasing cross-sectional areas is visible. For the loaded case it can be seen that the maximally attainable shrinkage increases monotonically for an increasing cross-sectional area. When grouping the results on their minor cross-sectional dimension, the results are effectively grouped on their shortest thermal penetration depth. By doing this, insights regarding the influence of the major cross-sectional dimension might become visible. In figure 11a it can be seen that by keeping the minor dimension at 1 mm, an increasing major dimension gives a higher shrinkage value. Maximum shrinkage is observed for $1 \times 10\text{ mm}^2$. When reducing the aspect ratio while further increasing the total cross-sectional area, the maximum attainable shrinkage reduces slightly. In the loaded case (figure 11b) the aspect ratio between the major and minor cross-sectional dimensions seems to matter less than the total cross-sectional area; shrinkage monotonically increases with the cross-sectional area regardless of this aspect ratio.

3.2. Demonstrator

Based on the results of section 3.1 design parameters for the demonstrator samples are established. For the printing speed a value of 90 mm/s is chosen as



(a) Shrinkage without added spring stiffness - i.e. not loaded



(b) Shrinkage with added spring stiffness - i.e. loaded

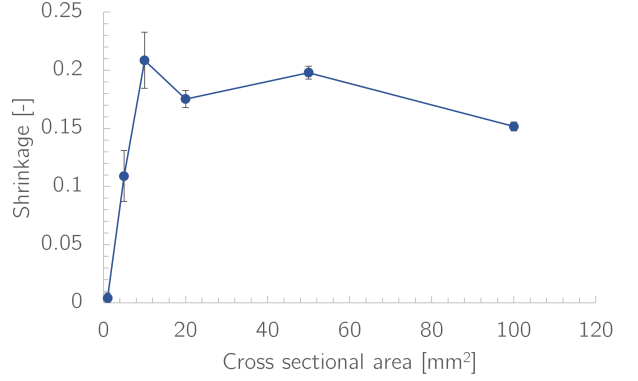
Figure 9: Axial material shrinkage as a function of the heating time.

the print quality at this speed is still sufficient while also giving a close-to-maximum **shrinkage max**. For the heating temperature the setpoint corresponding to the largest **shrinkage max** values is taken. For the heating time the setpoint with the largest **shrinkage net** is chosen. The cross-sectional area of the PLA middle beam directly influences the rotational stiffness and as such, when picking a too large value, it could obstruct the demonstrator's rotation during flexure buckling. A square cross-section is therefore chosen that has a corresponding area of 10 mm^2 . This gives the design parameters as presented in table 3.

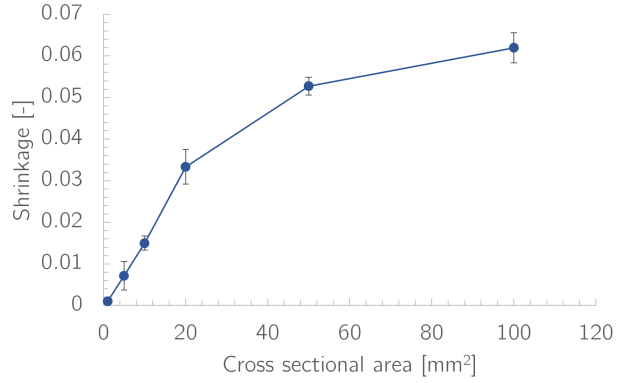
Table 3: Design parameters chosen for the demonstrator samples.

Parameter	Value
Width	3.2 mm
Height	3.2 mm
Length	100 mm
Printing speed	90 mm/s
Bed temperature	60°C
Nozzle temperature	215°C
Infill density	100%
Infill pattern	parallel rectilinear
Fan speed	0%
Heating time	30 s
Heating temperature	110°C

The post-heating measurements of the axial shrinkage and the rotation angle for the two demonstrator samples are shown in table 4. In figure 12a 3



(a) Shrinkage without added spring stiffness - i.e. not loaded



(b) Shrinkage with added spring stiffness - i.e. loaded

Figure 10: Axial material shrinkage as a function of the cross sectional area.

instances of the bidirectional bistable moment-angle curve for the first sample are plotted. In this plot also the ANSYS result for this particular PLA shrinkage magnitude is plotted as reference. In figure 12b the same information is shown for the second demonstrator sample. Both samples show correspondence with the ANSYS model both in their respective extreme torque values as well as in the range of motion. The torque-angle curves all show a slight amount of hysteresis.

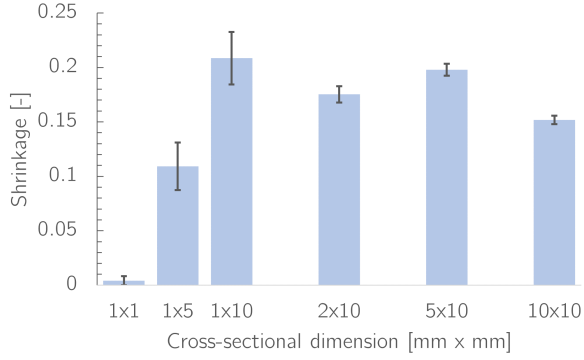
Table 4: Shrinkage and rotation angle results for the 2 demonstrator samples.

	Sample 1	Sample 2
Axial shrinkage [-]	-0.056	-0.051
Range of motion [rad]	-1.09/+1.10	-1.04/+1.05

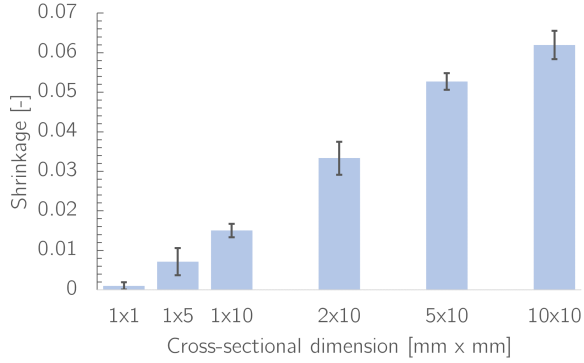
4. Discussion

4.1. Parameter study

In the parameter study both **shrinkage max** and **shrinkage net** are reported on. As the heating time as stated in table 1 was set beforehand, it was expected that a discrepancy between **shrinkage max** and **shrinkage net** might occur due to the complex interplay between heating time, heating temperature and the time-dependent nature of the temperature penetration. As found in the results that are



(a) Shrinkage without added spring stiffness - i.e. not loaded



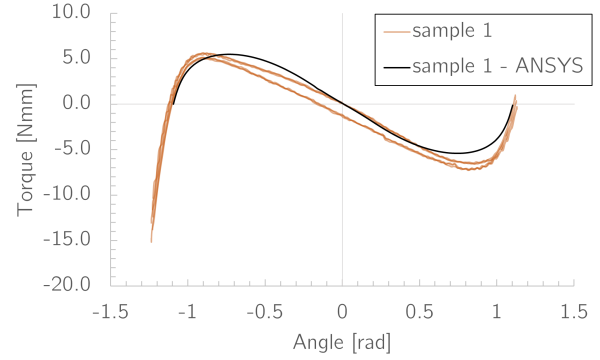
(b) Shrinkage with added spring stiffness - i.e. loaded

Figure 11: Axial material shrinkage as a function of the cross sectional area, grouped on the minor cross-sectional dimension.

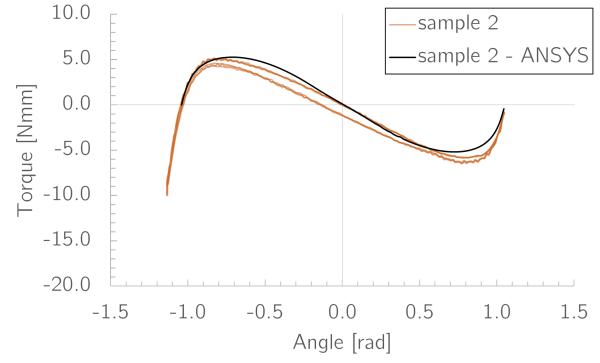
presented in section 3, this discrepancy indeed was found. To obtain the maximum shrinkage as indicated by `shrinkage_max` without having to deal with re-elongation of the material, the heating duration should be kept relatively short. This is also confirmed by the lowest two setpoints in figure 8b, where the difference between `shrinkage_max` and `shrinkage_net` remains relatively small.

The selection of relevant parameters for the parameter study is based both on the mentioning of parameters in literature (section 1), as well as on results from a preliminary parameter study of which the results are not included in this paper. Parameters with significant influence on the shrinkage behaviour were selected to be investigated further. Significant shrinkage is here defined as $>10\%$ of additional shrinkage with regard to the smallest shrinkage value that is obtained by the sole variation of the parameter under investigation. This criterion is defined for the setting where no springs are attached to the sample. Parameters that failed said criterion are the extrusion multiplication factor (1.2% shrinkage), the cooling fan speed (5.4% shrinkage) and the heated bed temperature (0% shrinkage).

For examination of the influence of the cross-sectional area, discrete steps in the width and height of the cross-section are made to increase this area. An increase in cross-sectional area did however not necessarily correspond to a variation of only 1 dimension (e.g. 1×5 versus 2×10). Different cross-sectional



(a) Demonstrator sample 1



(b) Demonstrator sample 2

Figure 12: Torque-angle graphs for the two demonstrator samples.

areas might still have an equal temperature penetration time, as this time directly relates to the smallest geometrical dimension. Geometries with an equal smallest geometrical dimension (e.g. 1×1 and 1×10) all experience an almost equal internal temperature progression, making it valid to compare these results to each other directly. Geometries with a non-equal smallest geometrical dimension have a different internal temperature progression, potentially resulting in a cross-sectional area fraction that has a temperature above T_g and an area that has not yet reached this temperature. Above T_g the material will tend to shrink whereas below T_g the material is stiff and solid. This might lead to an internal shrinkage conflict, resulting in a lower shrinkage yield. As shown in figure 11, where the shrinkage results are grouped on their respective smallest geometrical dimension, this effect seems visible in the not loaded case (figure 11a). Here an increase of the minor geometrical dimension yields a lower shrinkage value. In the loaded case (figure 11b) this effect seems to be limited; here the shrinkage is monotonically increasing for an increasing surface area, also when the minor geometrical dimension increases. A possible explanation here is that the inclusion of the springs vastly reduces the shrinkage rate, hereby leaving relatively more time for homogeneous heating of the system whilst not yet experiencing an internal shrinkage conflict.

4.2. Demonstrator

A crackling noise originating from the wire flexures was heard during rotation of the bistable demonstrator in the torsion machine. This noise might indicate one or more failed glue connections, posing some degree of rotational freedom to the flexures. Attempted tests to confirm this rotational wire freedom were inconclusive. By the same tests it was however confirmed that no longitudinal play was present in the glued connection points. As can be seen in figures 12a and 12b, the torque-angle curve for the clockwise motion is somewhat different than the curve for the anti-clockwise motion, revealing a small amount of hysteresis. Failed glue connections might have contributed to this hysteresis.

During heating of the demonstrator, the PLA centre beam is found to permanently rotationally deform. In the oven the PLA enters the rubbery state in which the material can be easily deformed. A twist deformation is imposed on the middle beam due to the combination of the axial PLA shrinkage and the geometrical constrains provided by the wire flexures. When taken out of the oven the system re-enters the glassy state, hereby freezing the twist in the centre beam. This effect is not accounted for in the APDL simulation. In the simulation the twisting motion during axial shrinkage is modelled to be an elastic deformation. Moreover, PLA tends to get stiffer when it has been heated [49]. This temperature dependent effect is also not included in the ANSYS model. These factors might contribute to the differences between the modelled torque-angle curves and the measured ones.

With the parameter values that are chosen for the demonstrator, a shrinkage of about 2% was expected based on the `shrinkage_max` values from the parameter study. In section 3.2 it is observed that the axial shrinkage for the demonstrator samples sits between 5% - 6%, which is a significantly higher value. A first reason for this might be in the fact that the demonstrator is put upright in the oven. When the demonstrator would be orientated sideways, the steel crosses would sit on the oven's bottom plate, requiring extra frictional force to be overcome by the PLA middle beam during shrinkage. In the upright position this effect does not occur, which is deemed to be a better situation. In this position the weight of the steel top cross does however still influence the resulting axial PLA shrinkage. As gravity and the axial shrinkage direction are parallelly orientated, gravity assists the shrinking PLA in buckling of the wire flexures. Based on perspective this might either be considered to be a benefit or a disadvantage of the method. It was observed that the weight of the steel crosses alone did not result in flexure buckling. This observation emphasizes the necessity of the PLA shrinkage effect for obtaining bistability. A second reason for the relatively high shrinkage values might be in the fact that all design parameters are chosen at their opti-

mum point of influence. When combining these optimum settings, this potentially results in an amplified shrinkage magnitude.

In the here presented work a symmetrically bistable mechanism is obtained from an initially monostable structure. In section 1 it is indicated that also neutrally stable compliant mechanisms may benefit from the here proposed prestressing method. Neutral stability can be acquired from a symmetrically bistable profile by adding a certain amount of parallel positive stiffness to the system. In figure 13 the bistable torque-angle curve for sample 1 of the demonstrator is shown, together with the by APDL obtained torque-angle curve of the monostable stage of the demonstrator. By depicting the bistable curve relative to the monostable curve, one might argue that the bistable mechanism already qualifies as a quasi-neutrally stable mechanism.

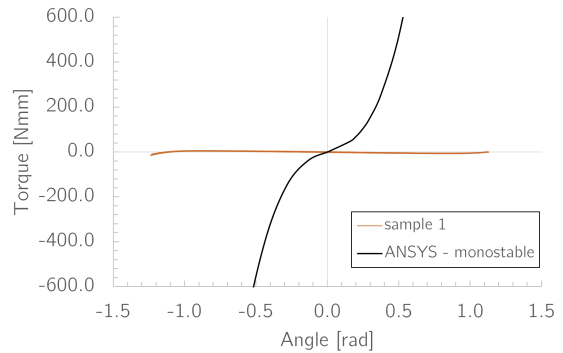


Figure 13: The torque-angle curve for demonstrator sample 1, together with the torque-angle curve of the monostable stage of the demonstrator as obtained with APDL.

4.3. Future research

Based on the here discussed topics some suggestions for future research can be made. Firstly the (in)dependence of design parameters should be investigated into more depth. Following from the results, a suspicion towards cross-correlations between thermal and spatial variables has been risen. Moreover, the influence of other design variables (e.g. the heated bed temperature and the fan speed) could be researched as to obtain an even higher shrinkage yield. Finally, as an extension to this work, focus could be put on dual-material FFF printing. When two materials with sufficiently different T_g s are used, the here presented techniques could be applied to induce prestress to members of fully FFF-printed geometries.

5. Conclusion

In this work the influence of 4 different parameters on the heat-induced shrinkage potential of FFF printed PLA is investigated. This is done to assess the applicability of heat-induced shrinkage as a prestressing method for obtaining non-monostable compliant mechanisms. It is found that the printing speed, heating temperature, heating time and cross-sectional area all are of major influence on the obtainable

shrinkage magnitude of the tested samples. In the case where the samples do not need to overcome a resisting force, a shrinkage magnitude of up to 20% can be achieved with all parameters individually. When the samples experience a linear stiffness profile that is equivalent to the secant stiffness of 4 buckling wire flexures, a more realistic representation of a prestressing case is presented. By adding such a linear stiffness profile to the test setup it is found that all individual parameters are able to give a maximally attainable shrinkage value of over 2%. To further prove the usefulness of this prestressing technique, a permanent monostable-to-bistable system alteration is successfully demonstrated through the use of a compliant demonstrator mechanism. Parameters for this demonstrator are based on the parameter study. A resulting PLA shrinkage of over 5% is found for this demonstrator model. This result exceeds the expectations from the parameter study and it further underlines the potential of this technique for utilization as a prestressing method for obtaining non-monostable compliant mechanisms.

References

- [1] M. Ceccarelli, editor. *On the Classification of Compliant Mechanisms*, Proceedings of EUCOMES 08, Dordrecht, 2009. Springer.
- [2] *Design of an Underactuated Finger With a Monolithic Structure and Largely Distributed Compliance*, volume Volume 2: 34th Annual Mechanisms and Robotics Conference, Parts A and B of *International Design Engineering Technical Conferences and Computers and Information in Engineering Conference*, Montreal, Quebec, Canada, 2010. The American Society of Mechanical Engineers.
- [3] J.A. Cronin, M.I. Frecker, and A. Mathew. Design of a compliant endoscopic suturing instrument. *Journal of Medical Devices*, 2(2):025002, 2008.
- [4] B.P. Trease, Y. Moon, and S. Kota. Design of large-displacement compliant joints. *Journal of Mechanical Design*, 127(4):788–798, 2004.
- [5] L.L. Howell, S.S. Rao, and A. Midha. Reliability-based optimal design of a bistable compliant mechanism. *Journal of Mechanical Design*, 116(4):1115, 1994.
- [6] M.A. Pucheta and A. Cardona. Design of bistable compliant mechanisms using precision–position and rigid-body replacement methods. *Mechanism and Machine Theory*, 45(2):304–326, 2010.
- [7] N.D. Masters and L.L. Howell. A self-retracting fully compliant bistable micromechanism. *Journal of Microelectromechanical Systems*, 12(3):273–280, 2003.
- [8] Y.S. Oh and S. Kota. Synthesis of multistable equilibrium compliant mechanisms using combinations of bistable mechanisms. *Journal of Mechanical Design*, 131(2):021002, 2009.
- [9] H. Zhang, B. Zhu, and X. Zhang. Origami kaleidocycle-inspired symmetric multistable compliant mechanisms. *Journal of Mechanisms and Robotics*, 1(1):011009, 2018.
- [10] *Development of a Tristable Compliant Mechanism*, The 12th World Congress in Mechanism and Machine Science, Besançon, France, 2007. International Federation for the Promotion of Mechanism and Machine Science.
- [11] *A Novel Actuated Composite Tape-Spring for Deployable Structures*, Proceedings of 45th AIAA/ASME/ASCE/AHS/ASC Structures, Structural Dynamics & Materials Conference, Palm Springs, California, USA, 2012. AIAA.
- [12] S.D. Guest, E. Kebabzadeh, and S. Pellegrino. A zero-stiffness elastic shell structure. *Journal of Mechanics of Materials and Structures*, 6(1-4):203–212, 2011.
- [13] E.L. Starostin and G.H.M. van der Heijden. The shape of a möbius strip. *Nature Materials*, 6:563–567, 2007.
- [14] J. Qiu and J.H. Lang. A curved-beam bistable mechanism. *Journal of microelectromechanical systems*, 13(2):137–145, 2004.
- [15] M.G. de Jong, W.P.J. van de Sande, and J.L. Herder. Properties of twofold tape loops: The influence of the subtended angle. *Journal of Mechanisms and Robotics*, 11(2), 2019.
- [16] L. Kiener, H. Saudan, F. Cosandier, G. Perruchoud, and P. Spanoudakis. Innovative concept of compliant mechanisms made by additive manufacturing. *MATEC Web Conf.*, 304:07002, 2019.
- [17] R. Mutlu, G. Alici, M. in het Panhuis, and G. Spinks. Effect of flexure hinge type on a 3d printed fully compliant prosthetic finger. In *2015 IEEE International Conference on Advanced Intelligent Mechatronics (AIM)*, pages 790–795. IEEE, 2015.
- [18] M.C.M. Hisham, R. Mutlu, and G. Alici. 3d printing of a thin-wall soft and monolithic gripper using fused filament fabrication. In *2017 IEEE International Conference on Advanced Intelligent Mechatronics (AIM)*, pages 442–447. IEEE, 2017.
- [19] P. Kumar, C. Schmidleithner, and N.B. Larsen. Topology optimization and 3d printing of large deformation compliant mechanisms for straining biological tissues. *Structural and Multidisciplinary Optimization*, 63:1351–1366, 2020.
- [20] G. Radaelli. Reverse-twisting of helicoidal shells to obtain neutrally stable linkage mechanisms. *International Journal of Mechanical Sciences*, 202-203:106532, 2021.
- [21] T.D. Ngo, A. Kashani, G. Imbalzano, K.T.Q. Nguyen, and D. Hui. Additive manufacturing (3d printing): A review of materials, methods, applications and challenges. *Composites Part B: Engineering*, 143:172–196, 2018.
- [22] T. Sathies, P. Senthil, and M.S. Anoop. A review on advancements in applications of fused deposition modelling process. *Rapid Prototyping Journal*, 26(4):669–687, 2020.
- [23] FACT.MR. 3d printing materials market outlook (2021–2031), 2022.
- [24] A. Dey, I.N.R. Eagle, and N. Yodo. A review on filament materials for fused filament fabrication. *Journal of Manufacturing and Materials Processing*, 5, 2021.
- [25] S. Ahn, M. Montero, D. Odell, S. Roundy, and P.K. Wright. Anisotropic material properties of fused deposition modeling abs. *Rapid Prototyping Journal*, 8(4):248–257, 2002.
- [26] S.R. Rajpurohit and H.K. Dave. Analysis of tensile strength of a fused filament fabricated pla part using an open-source 3d printer. *The International Journal of Advanced Manufacturing Technology*, 101:1525–1536, 2019.
- [27] X. Gao, S. Qi, X. Kuang, Y. Su, J. Li, and D. Wang. Fused filament fabrication of polymer materials: A review of interlayer bond. *Additive Manufacturing*, 37:101658, 2021.
- [28] H. Prajapati, D. Ravoori, R.L. Woods, and A. Jain. Measurement of anisotropic thermal conductivity and interlayer thermal contact resistance in polymer fused deposition modeling (fdm). *Additive Manufacturing*, 21:84–90, 2018.
- [29] R. Rane, A. Kulkarni, H. Prajapati, R. Taylor, A. Jain, and V. Chen. Post-process effects of isothermal annealing and initially applied static uniaxial loading on the ultimate tensile strength of fused filament fabrication parts. *Materials*, 13(2):352, 2020.
- [30] R.M. Dunn, K.R. Hart, and E.D. Wetzel. Improving fracture strength of fused filament fabrication parts via thermal annealing in a printed support shell. *Progress in Additive Manufacturing*, 4:233–243, 2019.
- [31] J. Butt and R. Bhaskar. Investigating the effects of annealing on the mechanical properties of fff-printed thermoplastics. *Journal of Manufacturing and Materials Processing*, 4(38), 2020.
- [32] Y. Zhang and S.K. Moon. The effect of annealing on additive manufactured ultem 9085 mechanical properties. *Materials*, 14(11), 2021.
- [33] B. Wijnen, P. Sanders, and J.M. Pearce. Improved model and experimental validation of deformation in fused filament fabrication of polylactic acid. *Progress in Additive Manufacturing*, 3:193–203, 2019.
- [34] F. Momeni, S.M. Mehdi Hassani, X. Liu, and J. Ni. A review of 4d printing. *Materials & Design*, 122:42–79, 2017.

- [35] A.R. Rajkumar and K. Shanmugam. Additive manufacturing-enabled shape transformations via fff 4d printing. *Journal of Materials Research*, 33(24):4362–4376, 2018.
- [36] Q. Zhang, D. Yan, K. Zhang, and G. Hu. Pattern transformation of heat-shrinkable polymer by three-dimensional (3d) printing technique. *Sci Rep*, 5:8936, 2015.
- [37] Q. Zhang, K. Zhang, and G. Hu. Smart three-dimensional lightweight structures triggered from a thin composite sheet via 3d printing technique. *Sci Rep*, 6:22431, 2016.
- [38] Y. Wang and X. Li. An accurate finite element approach for programming 4d-printed self-morphing structures produced by fused deposition modeling. *Mechanics of Materials*, 151:103628, 2020.
- [39] T. van Manen, S. Janbaz, and A.A. Zadpoor. Programming 2d/3d shape-shifting with hobbyist 3d printers. *Materials Horizons*, 4(6):935–1202, 2017.
- [40] L. Kačergis, R. Mitkus, and M. Sinapius. Influence of fused deposition modeling process parameters on the transformation of 4d printed morphing structures. *Smart Materials and Structures*, 28:105042, 2019.
- [41] *Telemorph: Democratizing 4D Printing of Self-Folding Materials and Interfaces*, CHI Conference on Human Factors in Computing Systems, Montréal, QC, Canada, 2018. Association for Computing Machinery.
- [42] C. Chen, J. Chueh, H. Tseng, H. Huang, and S. Lee. Preparation and characterization of biodegradable pla polymeric blends. *Biomaterials*, 24(7):1167–1173, 2003.
- [43] M. Grazzo, L. Azzouz, P. Ruiz-Hincapie, M. Zarrelli, and G. Ren. Effect of temperature on the mechanical properties of 3d-printed pla tensile specimens. *Rapid Prototyping Journal*, 24(8):1337–1346, 2018.
- [44] H. Ahmad, G. Radaelli, and J. Herder. *Design and fabrication of a compliant joint with activatable pre-stress to switch between a stiff and a neutrally stable state*. Master’s thesis, Delft University of Technology, 2022.
- [45] R.B. Dupaix and M.C. Boyce. Finite strain behavior of poly(ethylene terephthalate) (pet) and poly(ethylene terephthalate)-glycol (petg). *Polymer*, 46(13):4827–4838, 2005.
- [46] T. Wang, J. Xi, and Y. Jin. A model research for prototype warp deformation in the fdm procethe international journal of advanced manufacturing technology. 33:1087–1096, 2007.
- [47] T. Yao, Z. Deng, K. Zhang, and S. Li. A method to predict the ultimate tensile strength of 3d printing polylactic acid (pla) materials with different printing orientations. *Composites Part B: Engineering*, 163:393–402, 2019.
- [48] Y. Song, Y. Li, W. Song, k. Yee, K.-Y. Lee, and V.L. Tagarielli. Measurements of the mechanical response of unidirectional 3d-printed pla. *Materials and Design*, 123:154–164, 2017.
- [49] *Influence of Annealing and Printing Directions on Mechanical Properties of PLA Shape Memory Polymer Produced by Fused Deposition Modeling*, volume Proceedings of the 6th International Congress of Serbian Society of Mechanics of *International Congress of Serbian Society of Mechanics*, Tara, Mountain Tara, Serbia, 2017.

3

The contribution of crystallization to heat-induced shrinkage of FFF printed parts

The contribution of crystallization to heat-induced shrinkage of FFF printed parts

Jonathan Linssen

Giuseppe Radaelli

Just Herder

Abstract - Parts that are produced by the FFF 3D printing method generally show inferior material properties compared to the bulk material. Post-print annealing is way to improve upon these material properties. As a by-effect of annealing significant material shrinkage occurs. In literature the origin of this shrinkage is either fully attributed to a change in crystallinity of the material, or fully to the activation of the shape memory effect. In the current work the contribution of crystallization-induced shrinkage to the total shrinkage figures of heated PLA is investigated in order to establish which of the two phenomena is more likely to be the main cause of the shrinkage. It is found that crystallinity changes only result in minor shrinkage magnitudes, making this principle unlikely to be the originator of the observed total shrinkage.

Index terms - crystallization, polymer, x-ray diffraction, shrinkage

1. Introduction

Fused Filament Fabrication (*FFF*) is a production technique in which polymeric filament material is sequentially deposited in a 3D build volume. In a layer-by-layer fashion a 3-dimensional geometry is hereby constructed. FFF as a production technique is widely used for rapid prototyping purposes. In recent years it has also gained popularity as a means to produce industrial-grade parts and components [1]. Parts that are produced with FFF show reduced mechanical and thermal properties in comparison to the bulk base material. Properties that are affected by the FFF process are, amongst others, the ultimate tensile strength, the yield strength and the Young's modulus [2–5]. An often used method to re-improve upon the material properties of a printed part is thermal annealing [6, 7]. By thermal annealing the part is homogeneously heated to an annealing temperature T_a for a duration that can vary from a few minutes to several hours [8–10]. The T_a generally lies within the rubbery range of the respective polymer, i.e. between the glass transition temperature (T_g) and the melting temperature (T_m). By setting T_a to a value within this rubbery range, the interlaminar toughness increases [11], the crystallinity rises [8] and interlayer bonding strengthens [12]. Consequently, the aforementioned material properties increase significantly, resulting in a part that is of better mechanical and thermal quality.

An observation that is repeatedly reported on during heat introduction to printed parts is the significant anisotropic shrinkage of the printed geometry [13–15].

This shrinkage is of such magnitude that geometric tolerances are strongly influenced. The major shrinkage direction is reported to be collinear with the local print direction. Both directions perpendicular to this print direction show shrinkage figures that are significantly lower than the shrinkage of the major direction. A second observation that is done in literature is the existence of a direct relation between the printing speed and the shrinkage magnitude that follows from heat introduction. A low printing speed results in relatively small shrinkages whereas a high printing speed gives relatively large shrinkages [16–20].

When reviewing literature on the topic of heat-induced shrinkage of FFF printed parts, at least two different hypotheses for this shrinkage behaviour can be distinguished. The first hypothesis relates the material shrinkage to an increase in the crystallinity fraction of the annealed material. The second hypothesis seeks an explanation in the shape memory property that can be found in several polymeric materials.

1.1. Crystallization shrinkage

In semi-crystalline polymers the amorphous material phase and the crystalline material phase are co-existing. The mass ratio in which these two phases are present in the material define the crystallinity fraction (*CF*) [21]. A *CF* of 0% implies a fully amorphous material whereas a *CF* of 100% would imply a fully crystalline material. Generally a *CF* of 100% is not attainable. Due to the existence of polymer cross-links and chain entanglements, crystallization of amorphous regions is only limitedly possible. The *CF* of semi-crystalline materials thus almost always lies below 100%. The maximum attainable degree of crystallinity for PLLA lies for example around 60% [22]. As the polymer chains in the crystalline phase are more orderly and densely packed than in the amorphous phase, an increase in crystallinity fraction generally gives a relative reduction of the total volume [23]. This volumetric reduction results in material shrinkage. The crystallinity fraction of semi-crystalline polymeric material is able to increase by cold crystallization [24]. Cold crystallization occurs when the material temperature is elevated from sub- T_g to a temperature that sits in the range between T_g at the lower bound and T_m at the upper bound [25, 26]. The rubbery amorphous polymeric chains now have an attained mobility that allows the chains to form the more energetically favourable or-

dered crystal structure [27]. For temperatures lower than T_g the polymer chains are said to be frozen; in this state the chains have zero mobility. For temperatures higher than T_m the molecular crystal arrangement is destroyed, giving an effective CF of zero [23]. With a change in crystallinity also mechanical material properties such as the stiffness, the yield point and the tensile strength are improved [28].

Cunha and O. Robbins [29] discuss the existence of flow-induced molecular alignment in polymers. FFF printers force viscoelastic heated filament through a narrowing nozzle which can result in flow-induced polymer alignment [30]. Due to polymer alignment crystal nucleation sites in the filament can also align along the extrusion direction [31,32]. When the material is annealed after printing, the crystallization-induced shrinkage may therefore show a direction dependence.

1.2. Shape memory induced shrinkage

The second principle with which heat-induced shrinkage can possibly be explained finds its fundamentals in the shape memory property that some polymeric material have. A shape memory polymer (*SMP*) is a material that is able to switch between a deformed shape and an original shape. This state switch is often triggered by thermal input, but it can also originate from other stimuli such as electric current, magnetic fields or moisture [33]. The thermally-triggered shape memory effect works based on the change in polymer mobility that occurs when the material's temperature surpasses the memory activation temperature. For most thermally-triggered SMPs this activation temperature is the T_g [34]. It is also above this T_g where the memory must be imposed onto the material. When residing in the rubbery state, the material's stiffness is strongly decreased, hereby allowing for easy deformation of the material [35]. If polymeric material is deformed in the rubbery state and kept in that particular deformed shape while bringing down the temperature to sub- T_g (the glassy range), the deformed shape is frozen into the solid material. The material will show no tendency to go back to the initial undeformed shape for as long as the temperature remains below T_g . When increasing the temperature to a value that lies within the rubbery range again, the system will transform back to its original shape.

When forcing filament through the narrowing printing nozzle during FFF printing, this exact phenomenon might occur. The filament has a temperature that is higher than T_g . Moreover, the filament is narrowed and elongated due to the interaction with the nozzle. Herewith a memory is imposed onto the printed filament. As deposited material quickly cools down to a temperature that is sub- T_g , the memory is stored in the printed workpiece. When reheating the workpiece by annealing, the system tries to retrieve its memorized shape. As the memory prescribes a

thickening and a shortening of all individual filament lines, this can be observed as component shrinkage at the macro-scale. Shrinkage will be predominant in the filament's printing direction.

1.3. State of the literature

Literature that pertains material shrinkage as a consequence of post-print heating sometimes finds its explanation in crystallization-induced shrinkage [15,36–39], while in other occasions the shrinkage is attributed to the shape memory effect [17,40–42]. No literature that dedicates itself to abating this ambiguity is found. The objective of the current work is therefore to provide more clarity to this topic. The likelihood of crystallization-induced shrinkage as the driving principle behind heat-induced material shrinkage of FFF printed parts is investigated. The effects of crystallization are measured by using the x-ray diffraction analysis method, yielding a quantitative value for the crystallinity fraction of the analysed material. Moreover, analytical calculations are done on the shrinkage magnitude that can be expected based on the acquired changes in the crystallinity fraction. With these results an assessment of the contribution of crystallinity changes to the total shrinkage behaviour will be made.

2. Method

The material that will be used throughout this study is polylactic acid (*PLA*). PLA is thermoplastic polymeric material that is widely used in FFF printing [43]. This material is of semi-crystalline nature and it qualifies as a T_g thermally-actuated SMP [44]. To eliminate the possible influence of colouring agents on the test results, a natural 1.75 mm PLA filament is used (DAS FILAMENT, Emskirchen, Germany). PLA has a T_g that lies between 50°C - 60°C [45] and a T_m that lies between 170°C - 180°C [45]. All samples that are used throughout this research are printed on a Creality Ender 3 Pro FFF printer (Shenzhen Creality 3D Technology Co, Ltd., Shenzhen, China).

2.1. The samples

As established in previous research there is a direct relation between the FFF print speed and the observed post-printing heat-induced shrinkage magnitude [16–20]. This shrinkage magnitude is reported to be of monotonically increasing nature for increasing print speeds. When adhering to the shrinkage explanation as provided in section 1.1, an increase in the shrinkage magnitude should be caused by an increase in the CF. A higher CF implies a higher crystalline-to-amorphous weight ratio after heating of the material. As crystalline material regions are more densely packed, this gives a lower total material volume, i.e. volumetric material shrinkage. According to this theory, an increase in printing speed should thus show

an increasing trend in the CF of the material after heating.

To establish whether this relation actually exists several FFF printed PLA samples are tested. All samples are printed with the exact same print settings except for the printing speed, which is different for each sample. G-code is generated with PrusaSlicer (version 2.4.2 - Prusa Research, Prague, Czech Republic). The default PLA preset from PrusaSlicer is used for slicing of the samples, with only the printing speed altered. The sample dimensions are shown in figure 1.

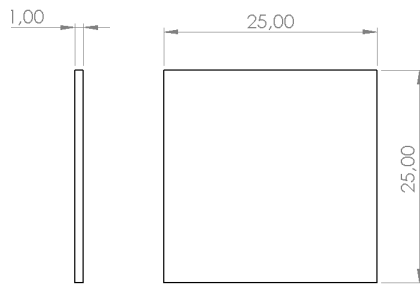


Figure 1: Representation of the sample and its dimensions.

The samples are printed with a parallel rectilinear pattern. By printing with this pattern it is assured that the parallel printing direction also corresponds to the major shrinkage direction of the sample [13]. The infill density is set to 100% for all samples. The assigned printing speeds are chosen such that they encompass a broad speed range; by also including extreme values in this range more pronounced shrinkage and crystallinity results are expected. The assigned printing speeds are 1 mm/s, 30 mm/s, 60 mm/s and 90 mm/s. For each speed setpoint two samples are printed. These identical samples are each assigned to a different test set; either **set 1** or **set 2**. The two test sets thus both comprise of 4 samples, of which each sample is printed with a different printing speed. These identical sets are indicated by **set 1** and **set 2** from here onwards.

As a first step several dimensions of the samples are measured. These measured dimensions are the distances in figure 2 that are indicated with: 1-2, 2-3, 3-4, 4-5, 5-6, 6-7, 7-8, 1-8, 1-5, 3-7, 2-6, 4-8, 2-4, 4-6, 6-8 and 2-8. Numbering of the measuring points is done with respect to the imprinted sample ID that is added to the top left corner of each sample. This is also shown in figure 2. These measurements are performed for both sample **set 1** and **set 2**. Also the sample thickness at each of the 8 measuring points is recorded. As a next step all samples belonging to **set 1** are put in a preheated oven (Silvercrest 9-in-1 Airfryer). The samples are heated for a duration of 300 seconds at a temperature of 110°C. Preliminary testing has shown that this combined heating time and temperature is sufficient for obtaining shrinkage magnitudes of adequate significance. After heating,

the samples are cooled down to room temperature and the aforementioned distances are measured again. The average shrinkage of lines 3-4, 4-5, 7-8, 1-8, and 2-6 will be used as an indication for the average axial shrinkage magnitude (i.e. parallel to the printing direction). The average shrinkage of lines 1-2, 2-3, 5-6, 6-7 and 4-8 will be used as an indication for the average transverse shrinkage magnitude (i.e. perpendicular to the printing direction). The shrinkage of the top area of each sample is calculated by triangulating area $\square 1357$ into 6 subdomains: $\triangle 128$, $\triangle 234$, $\triangle 456$, $\triangle 678$, $\triangle 268$ and $\triangle 246$. For each individual triangle Heron's formula can be used to calculate the area of this respective subdomain. When the areas of all subdomains are added, an approximation for the total top area is found. From preliminary testing it has become evident that in-plane shrinkage cannot be neglected. Oftentimes the in-plane deformation yields an hourglass type of shape. In the here used triangulated area approximation these in-plane shrinkage deformations are accounted for. By multiplying the now resulting top area with the average thickness of all 8 measuring points, an approximate value for the sample volume is obtained.

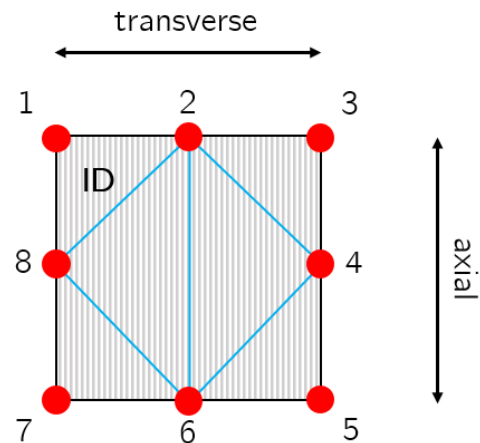
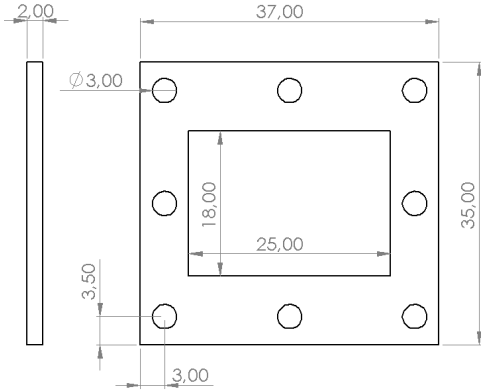


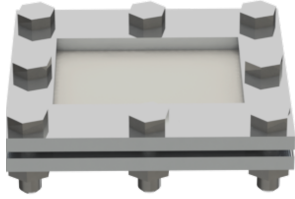
Figure 2: Measuring points on the sample. The grey lines indicate the direction of the parallel rectilinear printing pattern. The blue lines indicate the used triangulation pattern for each sample.

The samples belonging to **set 2** go through the same steps as **set 1**, with the only difference being that the samples are clamped between aluminium restraining frames during heating in the oven. A representation of the restraining frame is shown in figure 3. Each sample is clamped between two frames, which are connected by M3 bolt-nut connections. A visualisation of this can be found in figure 3b. The restraining frames are asymmetrical, meaning that clamping only occurs in a single shrinkage direction. The clamping direction is chosen such that the axial (major) shrinkage direction is constrained. By including the restraining frames, axial and transverse material shrinkage is partially obstructed. As it is unknown

whether this obstruction influences the changes in crystallinity fraction, the results of **set 2** might be important for understanding the underlying physical principles of crystallinity-induced shrinkage. If close-to-zero sample shrinkage is observed while still a vast change in the CF is found, this would suggest that changes in crystallinity are only limitedly related (and thereby limitedly accountable) for material shrinkage.



(a) Representation of the restraining frame including its dimensions in [mm].



(b) Representation of a sample that is clamped between two aluminium restraining frames.

Figure 3: The restraining aluminium frames that are used during heating of the samples of **set 2**.

Next to **set 1** and **set 2** yet another set of samples (**set 3**) is created. **Set 3** consists of 5 samples that are manufactured in the exact same manner as the samples from **set 1** and **set 2**, with the only difference being that these samples are all printed with an equal printing speed of 60 mm/s. The dimensions of the samples belonging to **set 3** are also measured prior to heating and after heating in the same way as explained for the samples of **set 1** and **set 2** (see figure 2). The samples belonging to **set 3** are not constrained during heating in the oven. The parameter that is altered for the samples from **set 3** is the heating time. All samples from **set 1** and **set 2** are heated for a fixed duration of 300 seconds. The samples from **set 3** are heated for a duration of 0 s, 20 s, 300 s, 1800 s and 3600 s respectively.

2.2. XRD testing

When all samples of **set 1**, **set 2** and **set 3** are heated and measured, the CF will be determined by

using an X-Ray Diffractometer (XRD). The machine that is used for the XRD analysis is the Bruker D8 Advance diffractometer (Bruker Corporation, Billerica, MA, USA) with a Bragg-Brentano parafocusing geometry. Cu-K α radiation is used. The measurement is a coupled $\theta - 2\theta$ scan in which diffraction patterns are made over a range of diffraction angles ranging from $5^\circ 2\theta$ to $110^\circ 2\theta$. The step size is $0.040^\circ 2\theta$ with a counting time of 1 s per step. The X-ray generator is set to a voltage of 45 kV and a current of 40 mA. A Lynxeye position sensitive detector is used. The detector is set to a lower level of 0.11 V and a window width of 0.14 V. Divergence slit V12 is used and the scatter screen height is set to 5 mm. Samples are fixed in the Bruker PMMA holder L40. The XRD data is evaluated with the Bruker DIFFRAC.EVA software. The crystalline material phases are extracted from the data by using the ICDD pdf4 database (International Centre For Diffraction Data, Newtown Square, PA, USA).

The crystallinity fraction χ_{XRD} is determined with equation 1.

$$\chi_{\text{XRD}} = \frac{A_{\text{crystalline}}}{A_{\text{total}}} \quad (1)$$

In this equation $A_{\text{crystalline}}$ represents the combined peak areas of the crystalline phases in the diffractogram. A_{total} is the total area under the diffraction pattern. Both area values are obtained with the DIFFRAC.EVA software.

To only compare the relative increase of the CF due to post-printing heat introduction, a non-heated benchmark sample is analysed by the XRD method as well. This sample is printed with a printing speed of 60 mm/s. After printing, this non-heated sample is subjected to the XRD analysis. The crystallinity fraction for this benchmark sample is found to be 0%. This indicates that printed samples can be considered to be fully amorphous prior to heating. The CFs resulting from **set 1**, **set 2** and **set 3** do therefore not require a corrective action to account for pre-heating crystallinity.

2.3. Crystallinity fraction calculations

The volumetric shrinkage values that are obtained by the triangulation method as explained in section 2.1 can be used to calculate the theoretically corresponding changes in crystallinity fraction. The density of crystalline PLA is reported to be 1360 kg/m^3 whereas the density of amorphous PLA is reported to be 1250 kg/m^3 [46]. It is assumed that conservation of mass is applicable to the current study, see equation 2. This implies that the sample mass prior to heating (m_{pre}) is equal to the sample mass after heating (m_{post}).

$$m_{\text{pre}} = m_{\text{post}} \quad (2)$$

Equation 2 can be rewritten as a function of the amorphous PLA density ρ_a , the crystalline PLA density ρ_c , the sample volume prior to heating V_{pre} , the sample

volume after heating V_{post} and the sub-volumes $V_{\text{post,c}}$ and $V_{\text{post,a}}$, representing the crystalline and amorphous volume fractions of V_{post} respectively. This results in equation 3

$$\rho_a V_{\text{pre}} = \rho_a V_{\text{post,a}} + \rho_c V_{\text{post,c}} \quad (3)$$

The total volume after heating consists of two components; an amorphous volume $V_{\text{post,a}}$ and a crystalline volume $V_{\text{post,c}}$. By reorganizing this relation, an expression for $V_{\text{post,a}}$ is obtained (equation 4).

$$V_{\text{post,a}} = V_{\text{post}} - V_{\text{post,c}} \quad (4)$$

$V_{\text{post,a}}$ in equation 3 can be substituted by the formulation of equation 4, resulting in equation 5.

$$\rho_a V_{\text{pre}} = \rho_a (V_{\text{post}} - V_{\text{post,c}}) + \rho_c V_{\text{post,c}} \quad (5)$$

Equation 5 only contains $V_{\text{post,c}}$ as an unknown, meaning that the equation can be solved for this value. Solving is done for all samples belonging to **set 1**, **set 2** and **set 3**. Equation 6 shows the definition of the weight crystallinity fraction χ_w [21].

$$\chi_w = \frac{\bar{v}_a - \bar{v}_{\text{post}}}{\bar{v}_a - \bar{v}_c} \quad (6)$$

In equation 6 the specific volumes \bar{v}_{post} , \bar{v}_a and \bar{v}_c are used. \bar{v}_a is the specific volume of fully amorphous PLA and \bar{v}_c is the specific volume of fully crystalline PLA. These values are obtained by taking the reciprocal of ρ_a and ρ_c respectively. \bar{v}_{post} is the resulting specific volume of the sample after heating. This value is unknown in principle, but can be calculated by using equation 7.

$$\bar{v}_{\text{post}} = \frac{V_{\text{post}}}{m_{\text{post}}} = \frac{V_{\text{post}}}{m_{\text{post,c}} + m_{\text{post,a}}} \quad (7)$$

In equation 7 $m_{\text{post,c}}$ represents the total mass of the crystalline material phase of the heated sample and $m_{\text{post,a}}$ represents the total mass of the amorphous material phase of the heated sample. Equation 7 can be rewritten into equation 8.

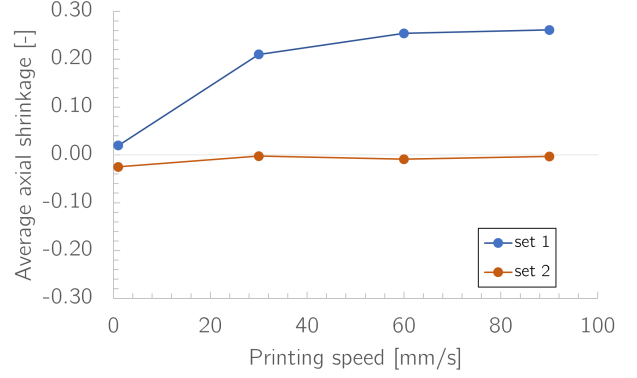
$$\bar{v}_{\text{post}} = \frac{V_{\text{post}}}{\rho_c V_{\text{post,c}} + \rho_a V_{\text{post,a}}} \quad (8)$$

$V_{\text{post,c}}$ and $V_{\text{post,a}}$ are already available due to the calculation of these values with equations 4 and 5. By inserting the value for V_{post} that is obtained with the triangulated volume measurements, \bar{v}_{post} is found. Now χ_w can be calculated by using equation 6.

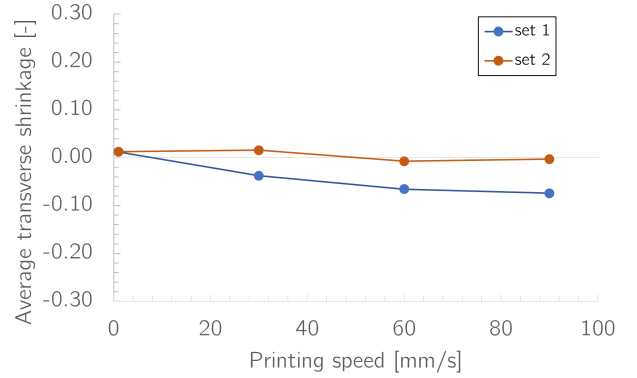
3. Results

3.1. Dimensional measurements and XRD testing

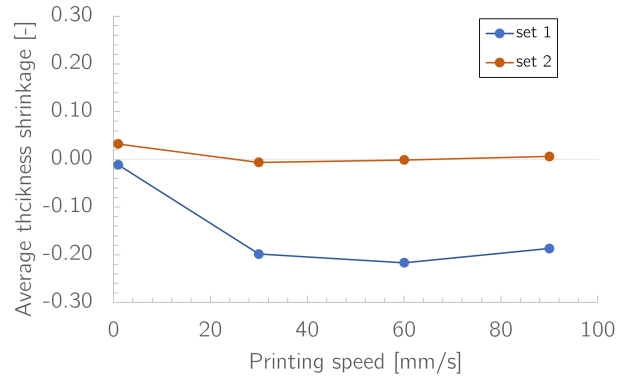
The measured average axial shrinkage of the samples of both **set 1** and **set 2** are shown in figure 4a. For the non-constrained **set 1** the results show a monotonic increase in the axial shrinkage magnitude. This



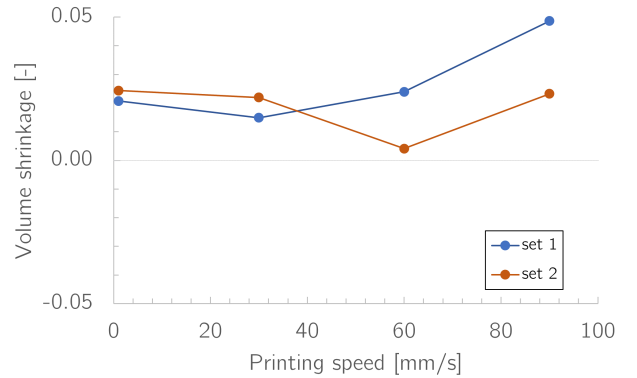
(a) Average axial shrinkage as a function of the printing speed.



(b) Average transverse shrinkage as a function of the printing speed.



(c) Average thickness shrinkage as a function of the printing speed.



(d) Volumetric material shrinkage as a function of the printing speed.

Figure 4: Axial, transverse, thickness and volumetric shrinkage values as a function of the printing speed. Results for **set 1** and **set 2**.

is in accordance with the literature as provided in section 2.1. For the constrained samples from **set 2** it can be seen that the axial shrinkage is mildly negative and almost constant for all setpoints. Negative axial shrinkage can be interpreted as expansion of the material in that respective direction.

In figure 4b the average transverse shrinkage is shown. For **set 1** the transverse shrinkage magnitude values are monotonically decreasing for increasing printing speeds. For the samples from **set 2** the shrinkage values vary between +2% and -2%. No clear trend or progression can here be extracted.

In figure 4c the shrinkage in the thickness direction is shown. For **set 1** this value is negative for each speed setpoint, thus implying an expansion. For a print speed of 1 mm/s this increase is close to 0%. For the other printing speeds the increase in thickness lies around 20%. For the samples from **set 2** the shrinkage values are all close to 0% with again no clear extractable trend in the shrinkage behaviour.

In figure 4d the approximated volume shrinkage is shown as a function of the printing speed. For the samples from **set 1** the volume shrinkage stays around a shrinkage value of 2% for the three lowest setpoints. Only for the printing speed of 90 mm/s a higher shrinkage of approximately 5% is found. For the samples from **set 2** for the printing speeds of 1 mm/s, 30 mm/s and 90 mm/s a volume shrinkage of approximately 2% can be found whereas for the printing speed of 60 mm/s a volume shrinkage of close to 0% is observed.

In figure 5 the crystallinity fractions for the samples from **set 1** and **set 2** are shown. For **set 1** it can be observed that the CF for a printing speed of 1 mm/s is approximately 5%. For higher printing speeds the CF is significantly lower than 5%. The uncertainty margin in the determination of the crystallinity fraction follows directly from the DEFFRAC.EVA software and has a value of $\pm 0.5\%$. These margins are also indicated in figure 5. The crystallinity fractions for the samples from **set 2** are consistently found to be around 3%-4% for all printing speeds.

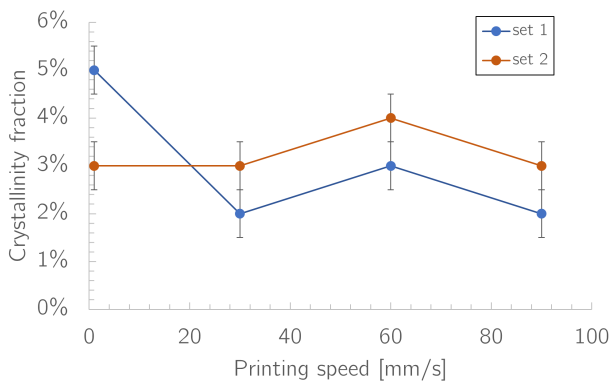
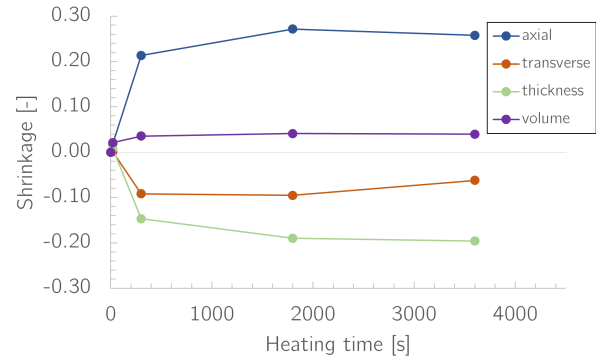


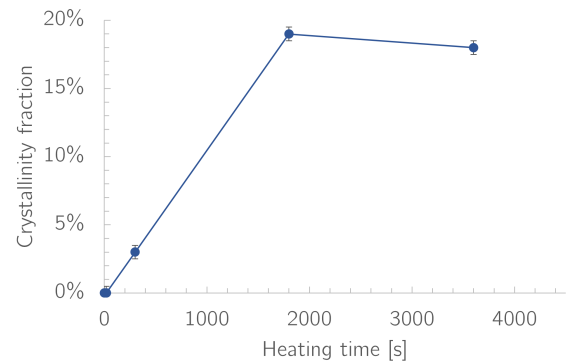
Figure 5: Crystallinity fraction as a function of the printing speed.

The results for the samples belonging to **set 3** are

shown in figure 6. In figure 6a it can be seen that all axial, transverse and thickness shrinkage values go to their respective extreme value at around 1800 s of heating time. At 300 s the values are already close to these extremes. The maximum volumetric shrinkage is obtained at 300 s. In figure 6b the crystallinity fraction for each sample of **set 3** is shown. It can be seen that at the maximum volumetric shrinkage (300 s) the CF is still far from its maximum value. This maximum CF is obtained around a heating time of 1800 s and yields approximately 20%.



(a) Average shrinkage values as a function of the heating time.



(b) Crystallinity fraction as a function of the heating time.

Figure 6: The shrinkage values and the crystallinity fraction, both as a function of the printing speed. Results for **set 3**.

3.2. Crystallinity fraction calculations

By using equation 6 the theoretical change in crystallinity fraction that is needed for the volumetric changes as reported in figure 4d can be calculated. The results of these calculations are shown in table 1. In this table χ_{XRD} is the CF as found with the XRD analysis. χ_{calc} is the CF that is calculated by using equation 6.

In table 1 a clear discrepancy between χ_{XRD} and χ_{calc} for all setpoints in both sets can be observed. Only for the printing speed of 60 mm/s in **set 2** χ_{XRD} seems to approach χ_{calc} , albeit still by 1% off. The values from table 1 can be added to figure 5, resulting in figure 7. These calculations have also been performed for the samples from **set 3**, giving the results as shown in table 2.

Table 1: Comparison of the crystallinity fraction as obtained by XRD and as resulting from calculations. Results for **set 1** and **set 2**.

	Print speed	χ_{XRD}	χ_{calc}
set 1	1	5%	25.6%
	30	2%	18.4%
	60	3%	29.6%
	90	2%	60.2%
set 2	1	3%	30.1%
	30	3%	27.1%
	60	4%	5.1%
	90	3%	28.8%

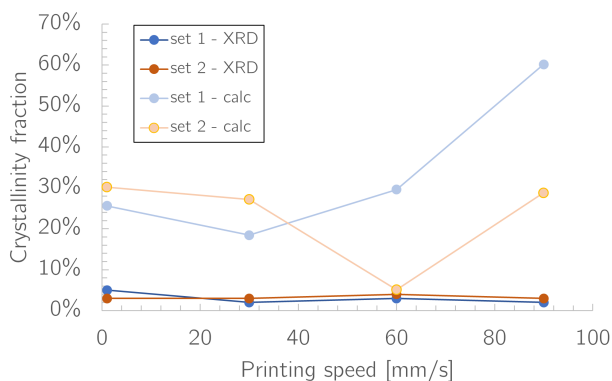


Figure 7: Crystallinity fraction as a function of the printing speed.

4. Discussion

With the results as presented in section 3.1 it is confirmed that the relation between the average axial shrinkage magnitude and the printing speed as found in literature (section 2.1) is indeed existing for the samples belonging to **set 1**. When comparing the results of both the axial shrinkage as well as the volumetric shrinkage to the XRD CF results, it is found that the crystallinity of printing speeds 30 mm/s, 60 mm/s and 90 mm/s are all of about the same value of 2-3%. Only at a printing speed of 1 mm/s a higher CF of 5% is found, which appears to be a clear outlier. There is no corresponding trend between the axial shrinkage for **set 1** and the change in CF of the sample. Even though the axial direction is the major shrinkage direction, the net material shrinkage is best captured by the volumetric shrinkage. When comparing the volumetric shrinkage magnitude of **set 1** in figure 4d to the CF values in figure 5, again no relation between the two can be observed.

When comparing the results from the XRD analysis for **set 1** to the results from the calculations in section 3.2, the likelihood of crystallization as the prime cause of heat-induced shrinkage is even further reduced. For obtaining the volume shrinkages that are established during the geometrical measurements an approximate crystallinity fraction of roughly a 5-to-30 fold larger would be required compared to what is found in the XRD analyses. This indicates that shrinkage that follows from an increasing crystallinity

Table 2: Comparison of the crystallinity fraction as obtained by XRD and as resulting from calculations. Results for **set 3**.

	Heating time	χ_{XRD}	χ_{calc}
set 3	0	0%	0.0%
	20	0%	26.1%
	300	3%	43.9%
	1800	19%	50.9%
	3600	18%	48.8%

fraction only has a minor influence on the total shrinkage behaviour. It can however not be excluded that crystallinity-induced shrinkage does to some degree contribute to the total shrinkage figures, both axially and volumetrically. This contribution does however seem to be very limited.

The samples from **set 2** are constrained in the axial direction. Consequently the axial shrinkage is indeed close to zero. Moreover, the transverse shrinkage direction and the thickness shrinkage direction are found to also display minute amounts of shrinkage compared to the samples from **set 1**. Volumetrically the observed shrinkage is however still found to be of comparable magnitude as found for the samples of **set 1**. Constraining of the samples thus has a major impact on the directional deformation behaviour of the sample. The imposed constraints do however not impact the total volumetric shrinkage values considerably. Moreover, constraining does not prohibit crystallization from occurring, as the crystallinity values for **set 2** are of comparable magnitude as for **set 1**. The volumetric shrinkage values for increasing printing speeds of **set 2** are of rather constant nature. The CF is also found to be semi-constant. An approximate relation between the volumetric shrinkage and the CF seems to be suggested here. When comparing the calculated CF to the CF following from XRD, this suggestion is however rejected. A multiplicity of the found CF is required to result in the observed volumetric shrinkage, meaning that crystallization cannot be solely responsible for the complete shrinkage.

The results from **set 3** strengthen the idea that crystallization actually has low influence on the eventual shrinkage magnitude. From figure 6 it appears that after a heating time of 300 s the axial, transverse, thickness and volumetric shrinkages are all close to their maximum attainable value. The CF that corresponds to this point is 3%. At the heating time of 1800 s a CF of 19% is found while no significant increase in either of the four shrinkage values is found.

The XRD analysis method is a rather expensive method of which the cost scales with the amount of measurements performed. For this reason only 1 sample per setpoint is analysed. The choice to use a small amount of samples has a direct influence on the statistical significance of the results. The trends that are found in the data of the current study correspond to trends found in literature. For this reason the results

are deemed sufficient on a qualitative level. For quantitative interpretation of the data the low statistical significance should be considered. As the shrinkage magnitudes and crystallinity values span a relatively broad range of results, small fluctuations in results are not detrimental. On a quantitative level the data is therefore also deemed to be of a level sufficient for drawing conclusions.

When comparing the crystallinity fractions from **set 2** to the fractions from **set 1** it can be seen that the fractions for **set 2** are consistently 1% higher at printing speeds 30 mm/s, 60 mm/s and 90 mm/s. The samples of **set 2** show volumetric shrinkages that are roughly equal (at 30 mm/s) or smaller (at 60 mm/s and 90 mm/s) than the corresponding shrinkages of **set 1**. This occurrence once more points towards a relative independence between material shrinkage and growth in the crystallinity. Due to the modest difference of only 1%, the low statistical significance does pose uncertainty in this regard.

In figure 5 a high crystallinity fraction value of 5% for the lowest printing speed in **set 1** is found. This value is a significant outlier with respect to the other values of both **set 1** and **set 2**. When printing a workpiece at this extremely low printing speed the hot nozzle only slowly moves over the workpiece. When the speed is sufficiently low, this might result in reheating of the previously deposited material layers to a temperature higher than T_g . Hereby cold crystallization is started, potentially resulting in a slightly increased crystallinity. Since this elevated crystallinity is not found for **set 2** no definite conclusions on this can be made. More samples at this setpoint should be tested to determine whether this value is an outlier or a correct value. In future research it would furthermore be useful to also measure the CF of each sample prior to the oven heating stage. In this way nozzle induced crystallinity changes could be corrected for.

For the analytical calculation of the volumetric shrinkage the method as explained in section 2 is used. By triangulating the sample's area into 6 triangles, of which only the lengths of the edges are measured, quite some shrinkage details could potentially be lost. To assure that this triangulation method provides sufficient accuracy in estimating the sample volume, a comparative test is performed between the triangulation measurement approach and an immersion test in water. The immersion test for sample volume determination is in theory more accurate, but it is not used for the samples of **set 1**, **set 2** and **set 3** as to not contaminate the radiation surface for the XRD tests. 4 different samples are subjected to this comparative test. The triangulated measurement results show to lie within a deviation band of $\pm 10\%$ compared to the immersion test. This uncertainty is deemed acceptable for this study.

For the analytical calculations of the crystallinity

fraction, the PLA amorphous density ρ_a and PLA crystalline density ρ_c are obtained from literature. Even though the ratio between ρ_a and ρ_c is of more importance than their absolute magnitudes, it is unclear how well the used values correspond to the respective densities for a geometry that is printed in a parallel rectilinear fashion with an infill density of 100%. When using other density values, the calculation outcomes will evidently change accordingly.

Based on the here presented results and discussion it is very unlikely that heat-induced changes in the crystallinity fraction are the main cause for the major shrinkage that is found in the axial printing direction of the PLA samples. The change in crystallinity does have a contribution to the total shrinkage figures, but its influence is only minor. As discussed in section 1.2, at least one other hypothesis exists on the origin of heat-induced shrinkage of printed polymeric materials. With the results of the current work the plausibility of this other explanation increases. It is evident that further research into the SMP-based shrinkage hypothesis should be conducted to ultimately determine whether this explanation is sufficient.

5. Conclusion

In this work the contribution of heat-induced crystallization shrinkage on the total shrinkage magnitude of heated FFF printed PLA is investigated. Based on the presented results shrinkage caused by crystallinity changes cannot be completely excluded as a contributing factor to the total shrinkage figures. It can however be concluded that crystallization shrinkage proves to be a highly unlikely cause of the extreme shrinkage values that follow from heat introduction to FFF printed PLA parts. The most significant shrinkage direction (axial), as well as the more representative volumetric material shrinkage do not show a comparable trend between the geometrical shrinkage values and their respective crystallinity fractions. Moreover, based on the discrepancies that followed from the analytical CF calculations in comparison to the XRD CF values, the probability of crystallization being the main cause of heat-induced shrinkage is further lowered.

References

- [1] T. Sathies, P. Senthil, and M.S. Anoop. A review on advancements in applications of fused deposition modelling process. *Rapid Prototyping Journal*, 26(4):669–687, 2020.
- [2] S. Ahn, M. Montero, D. Odell, S. Roundy, and P.K. Wright. Anisotropic material properties of fused deposition modeling abs. *Rapid Prototyping Journal*, 8(4):248–257, 2002.
- [3] S.R. Rajpurohit and H.K. Dave. Analysis of tensile strength of a fused filament fabricated pla part using an open-source 3d printer. *The International Journal of Advanced Manufacturing Technology*, 101:1525–1536, 2019.
- [4] X. Gao, S. Qi, X. Kuang, Y. Su, J. Li, and D. Wang. Fused filament fabrication of polymer materials: A review of interlayer bond. *Additive Manufacturing*, 37:101658, 2021.
- [5] H. Prajapati, D. Ravoori, R.L. Woods, and A. Jain. Measurement of anisotropic thermal conductivity and inter-

- layer thermal contact resistance in polymer fused deposition modeling (fdm). *Additive Manufacturing*, 21:84–90, 2018.
- [6] R.M. Dunn, K.R. Hart, and E.D. Wetzel. Improving fracture strength of fused filament fabrication parts via thermal annealing in a printed support shell. *Progress in Additive Manufacturing*, 4:233–243, 2019.
 - [7] R. Rane, A. Kulkarni, H. Prajapati, R. Taylor, A. Jain, and V. Chen. Post-process effects of isothermal annealing and initially applied static uniaxial loading on the ultimate tensile strength of fused filament fabrication parts. *Materials*, 13(2):352, 2020.
 - [8] R.A. Wach, P. Wolszczak, and A. Adamus-Wlodarczyk. Enhancement of mechanical properties of fdm-pla parts via thermal annealing. *Macromolecular Materials and Engineering*, 303(9):1800169, 2018.
 - [9] S. Wickramasinghe, T. Do, and P. Tran. Fdm-based 3d printing of polymer and associated composite: A review on mechanical properties, defects and treatments. *Polymers*, 12(7):1529, 2020.
 - [10] K. Sathish Kumar, R. Soundararajan, G. Shanthosh, P. Saravanakumar, and M. Ratteesh. Augmenting effect of infill density and annealing on mechanical properties of petg and cfpetg composites fabricated by fdm. *Materials Today: Proceedings*, 45:2186–2191, 2021. International Conference on Advances in Materials Research - 2019.
 - [11] K.R. Hart, R.M. Dunn, J.M. Sietins, C.M. Hofmeister Mock, M.E. Mackay, and E.D. Wetzel. Increased fracture toughness of additively manufactured amorphous thermoplastics via thermal annealing. *Polymer*, 144:192–204, 2018.
 - [12] J. Hong, T. Yu, Z. Chen, S. Park, and Y. Kim. Improvement of flexural strength and compressive strength by heat treatment of pla filament for 3d-printing. *Modern Physics Letters B*, 33(14n15):1940025, 2019.
 - [13] J. Butt and R. Bhaskar. Investigating the effects of annealing on the mechanical properties of fff-printed thermoplastics. *Journal of Manufacturing and Materials Processing*, 4(38), 2020.
 - [14] Y. Zhang and S.K. Moon. The effect of annealing on additively manufactured ultem 9085 mechanical properties. *Materials*, 14(11), 2021.
 - [15] B. Wijnen, P. Sanders, and J.M. Pearce. Improved model and experimental validation of deformation in fused filament fabrication of polylactic acid. *Progress in Additive Manufacturing*, 3:193–203, 2019.
 - [16] A.R. Rajkumar and K. Shanmugam. Additive manufacturing-enabled shape transformations via fff 4d printing. *Journal of Materials Research*, 33(24):4362–4376, 2018.
 - [17] Q. Zhang, D. Yan, K. Zhang, and G. Hu. Pattern transformation of heat-shrinkable polymer by three-dimensional (3d) printing technique. *Sci Rep*, 5:8936, 2015.
 - [18] Q. Zhang, K. Zhang, and G. Hu. Smart three-dimensional lightweight structures triggered from a thin composite sheet via 3d printing technique. *Sci Rep*, 6:22431, 2016.
 - [19] L. Kačergis, R. Mitkus, and M. Sinapius. Influence of fused deposition modeling process parameters on the transformation of 4d printed morphing structures. *Smart Materials and Structures*, 28:105042, 2019.
 - [20] B. An, Y. Tao, J. Gu, T. Cheng, X. Chen, X. Zhang, W. Zhao, Y. Do, S. Takahashi, H. Wu, T. Zhang, and L. Yao, editors. *Telemorph: Democratizing 4D Printing of Self-Folding Materials and Interfaces*, CHI Conference on Human Factors in Computing Systems, Montréal, QC, Canada, 2018. Association for Computing Machinery.
 - [21] S. Kavesh and J.M. Schultz. Meaning and measurement of crystallinity in polymers: A review. *Polymer Engineering & Science*, 9(5):331–338, 1969.
 - [22] J.F. Mano, J.L. Gómez Ribelles, N.M. Alves, and M. Salmerón Sanchez. Glass transition dynamics and structural relaxation of plla studied by dsc: Influence of crystallinity. *Polymer*, 46:8258–8265, 2005.
 - [23] D. Vaes and P. Van Puyvelde. Semi-crystalline feedstock for filament-based 3d printing of polymers. *Progress in Polymer Science*, 118:101411, 2021.
 - [24] P. Badrinarayanan, K. Brianna Dowdy, and M.R. Kessler. A comparison of crystallization behavior for melt and cold crystallized poly (l-lactide) using rapid scanning rate calorimetry. *Polymer*, 51(20):4611–4618, 2010.
 - [25] E.Piorcoeska and G.C. Rutledge. *Handbook of Polymer Crystallization*. John Wiley & Sons, inc., 2013.
 - [26] T. Wang, J. Xi, and Y. Jin. A model research for prototype warp deformation in the fdm process. *The International Journal of Advanced Manufacturing Technology*, 33:1087–1096, 2007.
 - [27] N.S. Trasi and L.S. Taylor. Effect of polymers on nucleation and crystal growth of amorphous acetaminophen. *CrystEngComm*, 16:5188–5197, 2012.
 - [28] H.W. Starkweather Jr., G.E. Moore, J.E. Hansen, T.M. Roder, and R.E. Brooks. Effect of crystallinity on the properties of nylons. *Journal of Polymer Science*, 11:189–204, 1956.
 - [29] M.A.G. Cunha and M. O. Robbins. Effect of flow-induced molecular alignment on welding and strength of polymer interfaces. *Macromolecules*, 53(19):8417–8427, 2020.
 - [30] M. Pivar, D. Gregor-Svetic, and D. Muck. Effect of printing process parameters on the shape transformation capability of 3d printed structures. *Polymers*, 14(1):117, 2022.
 - [31] Z. Ma, L. Balzano, and G.W.M. Peters. Dissolution and re-emergence of flow-induced shish in polyethylene with a broad molecular weight distribution. *Macromolecules*, 49(7):2724–2730, 2016.
 - [32] Z. Wang, Z. Ma, and L. Li. Flow-induced crystallization of polymers: Molecular and thermodynamic considerations. *Macromolecules*, 49(5):1505–1517, 2016.
 - [33] A. Lendlein and S. Kelch. Shape-memory polymers. *Angewandte Chemie International Edition*, 41(12):2034–2057, 2002.
 - [34] H. Meng and G. Li. A review of stimuli-responsive shape memory polymer composites. *Polymer*, 54:2199–2221, 2013.
 - [35] C.A. Mahieux and K.L. Reifsnider. Property modeling across transition temperatures in polymers: a robust stiffness-temperature model. *Polymer*, 42:3281–3291, 2001.
 - [36] A.G. Tantillo. *Annealing of Fused Filament Fabricated Nylon 6 with Elevated Isostatic Pressure*. Master’s thesis, Kate Gleason College of Engineering, 2019.
 - [37] T. Tábi, I.E. Sajó, F. Szabó, A.S. Luyt, and J.G. Kovács. Crystalline structure of annealed polylactic acid and its relation to processing. *eXPRESS Polymer Letters*, 4(10):659–668, 2010.
 - [38] B. de Wijk. *Annealing of 3D printed parts*. Master’s thesis, University of Groningen, 2022.
 - [39] D.G. Zisopol, A.I. Portoaca, I. Nae, and I. Ramadan. A comparative analysis of the mechanical properties of annealed pla. *Engineering, Technology & Applied Science Research*, 12(4):8978–8981, 2022.
 - [40] T. van Manen, S. Janbaz, and A.A. Zadpoor. Programming 2d/3d shape-shifting with hobbyist 3d printers. *Materials Horizons*, 4(6):1064–1069, 2017.
 - [41] G.F. Hu, A.R. Damanpack, M. Bodaghi, and W.H. Liao. Increasing dimension of structures by 4d printing shape memory polymers via fused deposition modeling. *Smart Materials and Structures*, 26:125023, 2017.
 - [42] L. Jia, Z. Hua, L. Ju, and L. Song. 4d printed shape memory polymers and their structures for biomedical applications. *Science China Technological Sciences*, 63:545–560, 2020.
 - [43] S.R. Subramaniam, M. Samykano, S.K. Selvamani, W.K. Ngui, K. Kadirgama, K. Sudhakar, and M.S. Idris. 3d printing: Overview of pla progress. *AIP Conference Proceedings*, 2059(1):020015, 2019.
 - [44] F.S. Senatov, K.V. Niaza, M.Yu. Zadorozhnyy, A.V. Maksimkin, S.D. Kaloshkin, and Y.Z. Estrin. Mechanical properties and shape memory effect of 3d-printed pla-based porous scaffolds. *Journal of the Mechanical Behavior of Biomedical Materials*, 57:139–148, 2016.
 - [45] C. Chen, J. Chueh, H. Tseng, H. Huang, and S. Lee. Preparation and characterization of biodegradable pla polymeric blends. *Biomaterials*, 24(7):1167–1173, 2003.
 - [46] S. farah, D.G. Anderson, and R. Langer. Physical and mechanical properties of pla, and their functions in widespread applications — a comprehensive review. *Advanced Drug Delivery Reviews*, 107:367–392, 2016.

4

Discussion

When reflecting on the goal of this work as stated in chapter 1, and when considering the results as provided in chapters 2 and 3, this project can be deemed successful. Some remarks with regard to the performed work and the acquired results can however be made.

The method as discussed in chapter 2 showed that a monostable-to-bistable stability transition can be obtained by introducing heat to printed material. The heat-induced (pre)stressing method showed sufficient employability on the macro scale for alteration of the stability behaviour. Scaling towards smaller scales is in the first place limited by the FFF technique itself; geometric features smaller than the printing nozzle diameter -generally 0.4 mm- is not possible with regular FFF printers. Moreover, geometrical scalability of the prestressing method has not been explicitly investigated in this research. It is therefore unclear whether small geometric scales show comparably sufficient results.

The results in this report currently only encompass a stability change from monostability to bistability. When comparing the bistable torque-angle curves to the torque-angle curves of the monostable structure, the bistable graph might even be considered to be quasi-neutrally stable. Strictly speaking neutral stability is however not achieved with the demonstrator of chapter 2. To acquire stability profiles that are different than bistable, other demonstrator geometries and other imposed stress fields are required. Since this is not included in the current report, little can be said about the general tailorability of the stability profiles of CMs that can be obtained by the here proposed method.

In chapter 2 no model is provided with which the design parameters can be related to the eventual shrinkage magnitude. Rather, only empirical results are presented. The current work would highly benefit from an accurate model in which design parameters could be related to eventual stresses and strains; tailoring of the stability profile of to be produced parts would be one step closer. The results from this report might form the onset to a simple empirical model in which the heat-induced directional shrinkage magnitude of printed filament lines can be obtained from the loaded and unloaded shrinkage relations as presented in chapter 2.

As found in the results of chapter 2, variable printing speeds result in variable shrinkage magnitudes. This is the case both when the material is loaded and when the material is not loaded. The printing speeds thus can be a design parameter with which the shrinkage magnitude can be variably assigned to regions of a printed part. This is an import factor when thinking about tailoring of the stability behaviour of different types of compliant mechanisms.

As following from the results of chapter 3, the observed semi-instantaneous shrinkage in heated FFF printed parts can most likely be attributed to the shape memory effect of the printed PLA. When looking at the shrinkage net progression in figure 9b in chapter 2, initially a decline in the shrinkage magnitude can be found. This decline makes sense and the reason for this is also provided in chapter 2. This decline reaches the lower limit of 0% shrinkage around a heating time of 300 s. Hereafter the shrinkage net starts to increase again, meaning that the sample material starts to re-compress the springs that are attached to the shrinkage measurement device. Solely based on the information that is provided in chapter 2, this re-increase in the

shrinkage magnitude cannot be explained. When comparing figure 9b in chapter 2 to figure 6b in chapter 3, an interesting observation is done. The increase in crystallinity fraction occurs on a time scale that is far longer than the time scale of the observed initial material shrinkage of heated PLA. The crystallinity fraction reaches its maximum value for a heating duration of 1800 s. The crystallinity fraction is however negligible for low heating durations. The re-increase of the shrinkage magnitude for heating times that are longer than 300 s (figure 9b, chapter 2) thus might be related to the increase in the crystallinity fraction. As an extension to this observation it can be hypothesized that the initial -major- shrinkage that is observed when introducing FFF printed parts to heat is caused by the shape memory property of the PLA. On longer time scales the influence of crystallinity shrinkage might add to the total shrinkage figures as well, meaning that both processes contribute to the total shrinkage magnitude of heated parts. This suspicion is however not further investigated and more data should be collected in order to determine whether this relation actually exists or not.

As became apparent in chapter 3, the most likely cause of heat-induced shrinkage in FFF printed parts is the activation of the shape memory. This insight might help to focus on specific FFF features in order to maximize the heat-induced material shrinkage and force-delivering potential of PLA in future work. The shape memory is stored during interactions with the narrowing nozzle. In the current work a nozzle with a diameter reduction from 1.75 mm to 0.4 mm is used. Nozzles with a diameter reduction of e.g. 1.75 mm to 0.25 mm are also commercially available. Evidently, a higher diameter reduction will lead to different filament-nozzle interactions, potentially yielding an even higher shrinkage and force-delivering property than is found in chapter 2.

In chapter 2 the relation between the shrinkage magnitude and the printing speed has been established. From chapter 3 it became highly plausible that the shape memory effect is underlying to this shrinkage. The speed dependent shrinkage profile as shown in figure 7 of chapter 2 can hereby be interpreted. For increasing printing speeds, increasing shrinkage magnitudes are found. At extremely low printing speeds a filament volume element remains relatively long inside the heated nozzle. Due to this longer heating time, the material can be fully heated, as opposed to faster printing speeds. The material temperature will then be close to the nozzle temperature. The nozzle temperature is significantly higher than the melting temperature of PLA. The PLA will therefore enter a "melted" (i.e. low-viscosity or rubbery liquid) state within the printing nozzle for low printing speeds. When the viscosity of a material is low, it is able to flow under the shear effects that are induced by the reducing nozzle diameter and the applied feeding pressure. The filament volume can hereby better conform to the reduced diameter. Consequently this gives less stretching and straining of individual polymer chains than would be the case for polymeric material that has a higher viscosity. Storage (or freezing) of polymer stretch and strain is essentially what causes the shape memory effect. For increasing printing speeds the heating of the filament material will be decreasingly thorough, yielding a higher viscosity. This increases the potential for storage of material shrinkage. This suspected relation is as of yet not explicitly investigated. Further research should be conducted to confirm or reject this hypothesis.

Future research

Based on the work that is presented in this report some suggestions for further research can be done. Firstly, no fundamental modelling of the observed shrinkage behaviour is performed. In future work modelling of the shrinkage behaviour might however be interesting. As a starting point, the shrinkage relations as provided in chapter 2 of this report could be used to create an empirical shrinkage model for PLA filament lines. By superposition of different print lines, and by connecting the filament elements in a finite element type of way, the observed shrinkage behaviour might already be roughly approached. Results from this model could be used to create custom g-code that can be directly fed to FFF printers. By including printing speed gradients to this g-code, a distributed shrinkage profile could be imposed onto the printed parts when they are heated. Secondly, the next step in the application of the here presented prestressing method is to use this method for prestressing of more complex monostable compliant mechanisms. An example of a geometry that would be suited for this is the helicoidal shell as presented by Radaelli [16]. Finally, future research could be aimed towards FFF printers that have dual nozzle capabilities. By printing with two materials, fully printed geometries can be obtained that can be partially prestressed by heat introduction. A short elaboration on this can be found in section 4.3 of chapter 2.

5

Conclusion

The goal of this thesis project was to create a method with which (pre)stress can be imposed onto monostable compliant mechanisms. This prestress was ought to bring about a permanent change in the stability behaviour; from a monostable state into a non-monostable state. The prestress inducement should be directly related to the production method with which the part is created. The production method that is chosen for this study is FFF.

By heating unconstrained FFF printed parts to a temperature higher than the glass transition temperature, a significant shrinkage of up to 20% can be obtained. When the shrinking material needs to perform mechanical work in the form of spring compression, the maximum attainable shrinkage figure reduces to a value that is still around 2%-3%. The printing speed shows to be a parameter with which the shrinkage magnitude can be scaled between 0% shrinkage (extremely low printing speeds) and the maximum shrinkage value (high printing speeds). The heating time, heating temperature and geometrical dimensions all proved to be of influence on the shrinkage behaviour. An increase in parameter value generally resulted in an increased shrinkage magnitude. With a composed set of optimum parameters, a monostable-to-bistable stability transition is performed for a rotational demonstrator model.

Results from the conducted research seem to suggest that heat-induced changes in the crystallinity fraction of PLA only minutely influence the shrinkage behaviour when heated for a short time (i.e. lower than a few minutes). The state of literature currently only has one other possible explanation for the material shrinkage, which is based on the shape memory property of polymeric materials. The likelihood of shape memory as the main shrinkage causing mechanic is therefore high. Contribution of crystallinity to the total shrinkage figures cannot be fully excluded. It does however seem that crystallinity-induced shrinkage occurs on far longer timescales than the shape memory induced shrinkage.

The general goal of this thesis project is successfully achieved. Questions regarding e.g. the application of this theory for obtaining tailored stability profiles, application to different dimensional scales and application to different geometries are as of yet unanswered. This shows that a lot of further research on this topic still can be done for advancements of this technique.

Bibliography

- [1] L.L. Howell. *Compliant Mechanisms*. John Wiley & Sons, 2001.
- [2] E.G. Merriam, J.E. Jones, and L.L. Howell. Design of 3d-printed titanium compliant mechanisms. In *42nd Aerospace Mechanisms Symposium*, pages 169–174, Greenbelt, Maryland, USA, 2014. NASA.
- [3] S. Linss, P. Graser, S. Henning, F. Harfensteller, R. Theska, and L. Zentner. Synthesis method for compliant mechanisms of high-precision and large-stroke by use of individually shaped power function flexure hinges. In *Proc. of the 15th IFToMM World Congress on Mechanism and Machine Science*, pages 1569–1578, Krakow, Poland, 2019. Springer International Publishing.
- [4] K. Entsfellner, I. Kuru, T. Maier, J.D.J. Gumprecht, and T.C. Lueth. First 3d printed medical robot for ent surgery - application specific manufacturing of laser sintered disposable manipulators. In *2014 IEEE/RSJ International Conference on Intelligent Robots and Systems*, pages 4278–4283, Chicago, Illinois, USA, 2014. IEEE.
- [5] M Schenk and S.D. Guest. On zero stiffness. *Proceedings of the Institution of Mechanical Engineers, Part C: Journal of Mechanical Engineering Science*, 228(10):1701–1714, 2014.
- [6] N. Tolou, V.A. Henneken, and J.L. Herder, editors. *Statically Balanced Compliant Micro Mechanisms (SB-MEMS): Concepts and Simulation*, volume Volume 2: 34th Annual Mechanisms and Robotics Conference, Parts A and B of *International Design Engineering Technical Conferences and Computers and Information in Engineering Conference*, Montreal, Quebec, Canada, 2010. ASME.
- [7] *A Novel Actuated Composite Tape-Spring for Deployable Structures*, Proceedings of 45th AIAA/ASME/ASCE/AHS/ASC Structures, Structural Dynamics & Materials Conference, Palm Springs, California, USA, 2012. AIAA.
- [8] E.L. Starostin and G.H.M. van der Heijden. The shape of a möbius strip. *Nature Materials*, 6:563–567, 2007.
- [9] M.G. de Jong, W.P.J. van de Sande, and J.L. Herder. Properties of twofold tape loops: The influence of the subtended angle. *Journal of Mechanisms and Robotics*, 11(2), 2019.
- [10] J. Qiu and J.H. Lang. A curved-beam bistable mechanism. *Journal of microelectromechanical systems*, 13(2):137–145, 2004.
- [11] S. Kok. *Towards neutrally stable compliant shells*. Master’s thesis, Delft University of Technology, 2020.
- [12] B.D. Jensen. *Identification of Macro- and Micro-Compliant Mechanism Configurations Resulting in Bistable Behavior*. Master’s thesis, Brigham Young Univeristy, 1998.
- [13] P. Stavropoulos, P. Foteinopoulos, A. Papacharalampopoulos, and G. Tsoukantas. Warping in slm additive manufacturing processes: estimation through thermo-mechanical analysis. *The International Journal of Advanced Manufacturing Technology*, 104(1):1571–1580, 2019.
- [14] M.M. El-Khabeery and M. Fattouh. Residual stress distribution caused by milling. *International Journal of Machine Tools and Manufacture*, 29(3):391–401, 1989.
- [15] N.S. Rossini, M. Dassisti, K.Y. Benyounis, and A.G. Olabi. Methods of measuring residual stresses in components. *Materials & Design*, 35:572–588, 2012.
- [16] G. Radaelli. Reverse-twisting of helicoidal shells to obtain neutrally stable linkage mechanisms. *International Journal of Mechanical Sciences*, 202-203:106532, 2021.

Appendix A: Review on the stress inducing potential of different manufacturing methods

1. Introduction

The purpose of this thesis is to find a way in which a prescribed stress pattern can be imposed onto a material, solely by the means of inherent mechanics of the used manufacturing process. This imposed stress pattern is ought to achieve a permanent change in the stability behaviour of a compliant mechanism; from monostable into non-monostable. Over time countless different production methods have been created. Each of these methods has its own advantages and disadvantages. In conventional production settings the introduction of stresses during manufacturing is considered to be a negative by-effect of the process [1–3]. To comply with the goal of this thesis, which is to deliberately induce stresses by the means of the manufacturing process, the usability of manufacturing methods should be reassessed on a fundamental level and in a non-conventional manner. In conventional production approaches the existence of e.g. thermal gradients will lead to undesired internal stress build-up and potentially even to warping and deformation of the workpiece [4]. In the current study this occurrence might however be considered to be a stress inducing method that fits the purpose of this thesis well.

It is not yet evident which process is the best fit for purpose to this study. To be able to choose the method that shows the highest stress inducing potential, a review on some of the most common (additive) manufacturing processes is performed. The results of this investigation are presented in this appendix. Subtractive production methods such as milling, lathing, laser cutting and electrical discharge machining are not included in this study. Subtractive methods work with a material volume that is partially chiselled, milled or cut away. By these actions generally only the very top layer of the material is mechanically affected by residual stresses, typically reaching to depths not further than $300\ \mu\text{m}$ from the area where material is removed [2]. This affected depth is deemed too shallow to bring about significant changes to the macro stability behaviour of compliant mechanisms that are created with subtractive manufacturing methods. An exception to this is the laser cutting technique in which the induced residual stress fields can bridge distances on the macro scale (affected areas of $\sim 5\ \text{mm}$ have been reported on [5]). Laser bending/forming can be considered to be a toned-down version of laser cutting. Laser bending/forming is included in this study.

For the sake of conciseness the considered manufac-

turing processes are not individually elaborated on in this appendix. Rather, a general grading is given to a set of criteria. References for further information on all criteria are provided.

2. Method

All manufacturing processes that are considered in this work are shown in table 1. The abbreviations that are used in the *family*-column are defined in the following way: AM: additive manufacturing, PBF: powder bed fusion (subgroup of AM), DED: direct energy deposition (subgroup of AM), ME: material extrusion (subgroup of AM), BJ: binder jetting (subgroup of AM), photo: Vat Photo-polymerization (subgroup of AM).

An investigation is performed on all manufacturing methods that are mentioned in table 1 through a literature study. The individual applicability of each method with regard to the scope of this thesis project is assessed through several criteria. Sources that provide answers to the criteria are formed by academic literature and available information from manufacturing companies and industrial service providers.

Table 1: The list of considered manufacturing methods.

Name	Abbreviation	Family
Selective Laser Sintering	SLS	AM-PBF
Selective Laser Melting	SLM	AM-PBF
Direct Metal Laser Sintering	DMLS	AM-PBF
Direct Metal Deposition(/Laser Engineered Net Shaping)	DMD(/LENS)	AM-DED
Selective Laser Cladding	SLC	AM-DED
Fused Deposition Modelling/Fused Filament Fabrication	FDM/FFF	AM-ME
Robocasting	RC	AM-ME
Ballistic Particle Manufacturing	BPM	AM-DED
Multi-Jet Modelling(/Multi-Jet Fusion/Thermojet)	MJM(/MJF/TJ)	AM-BJ
Electron Beam Manufacturing	EBM	AM-PBF
Wire Arc Additive Manufacturing	WAAM	AM-DED
Stereolithography	SLA	AM-Photo
Injection Moulding	IM	Moulding
Compression Moulding	CM	Moulding
Sand Casting	SC	Casting
Plaster Mold Casting	PIMC	Casting
Investment Casting(/Precision Casting)	IC(/PC)	Casting
Permanent Mold Casting	PeMC	Casting
Continuous Casting	CC	Casting
Die Casting	DC	Casting
Extruding (hot & cold)	EX	-
Laser Forming/Laser Bending	LF	-

This thesis work focusses on compliant mechanisms that have dimensions on to the macro scale (typical dimensions of 50 mm to 100 mm). The objective of this work is to create a compliant mechanism with a single manufacturing method. This manufacturing method should impose stresses onto the created work-piece as well, such that the compliant mechanism can attain non-monostable behaviour.

Inherent to compliant mechanisms are system regions that show high compliance. The compliance of a mechanism's region is directly related to the combination of the local material properties and the geometry. Apart from the choice of material, the only other way to obtain a desired compliance behaviour is thus by geometrical considerations. This poses several functional requirements onto the manufacturing processes that is used. Compliant regions are generally obtained in the form of thin-walled flexural sections [6]. Consequently, thin-walled features need to be obtainable with the manufacturing process. This pertains both the absolute obtainable smallest feature size, as well as the relative aspect ratios between system features that can be achieved with the process. Since the eventual compliance is formed by the combination of geometry and material, the different materials that can be processed with the manufacturing method should be considered as well. This results in the first few assessment criteria, which are stated below.

Criterion 1: What is the smallest feature size that can be obtained with the manufacturing method?

The magnitude of the smallest possible feature size that can be acquired with each manufacturing method will be investigated. Manufacturing processes will not be rejected solely based on the results for this criterion, even if the smallest feature size is relatively large. The smallest feature size will however be used in criterion 3, in which a selection on quantitative values will take place.

Criterion 2: What materials can be processed?

The materials that can be processed with each method have a direct influence on the attainable compliance that can be achieved with the manufacturing method. The materials that can be processed with each method are therefore identified as well. Almost all manufacturing processes are able to process more than just one material. Most processes can handle a multitude of materials that belong to a material group, like steel (alloys), aluminium (alloys) or ceramics. The material groups that are considered in this work are abbreviated in the following way - S: steel (including steel alloys), A: aluminium (including aluminium alloys), T: titanium (including titanium alloys), C: ceramics, CP: commodity polymers [7],

EP: engineering polymers [7]. Zinc-based alloys, copper-based alloys, nickel-based alloys, etc. are not explicitly included as separate material groups in this work. Some manufacturing processes will be able to process these (and other) material groups. These groups do however show little added significance with regard to the scope of this review. The considered material groups are therefore limited to the set formed by S, A, T, C, CP and EP.

Criterion 3: What is the highest attainable compliance?

The equivalent attainable compliance C for each individual production process is a measure that is here created to quantitatively compare the different production methods to each other. This equivalent compliance value is calculated by calculating the highest possible compliance value of a cantilever beam that can be produced with each of the manufacturing methods. The equivalent compliance is calculated according to equation 1.

$$C = \frac{4L^3}{wh^3E} \quad (1)$$

Equation 1 is directly derived from Euler-Bernoulli beam theory for a cantilever beam with a rectangular cross-section. The compliance value C represents the compliance in the direction of the applied force, which is perpendicular to the longitudinal direction of the cantilever beam. In equation 1 L is the length of the beam. This length is fixed to a length of 0.1 m for this study. As the resulting compliance value C will only be used for a relative comparison between the different manufacturing methods, the actual value for L is not of high importance here. This value will be the same for all manufacturing methods, hereby being a mere scaling factor for the C value. The w and h components in equation 1 are chosen such that they both correspond to the smallest feature size that can be acquired with the respective production process. This value directly follows from Criterion 1. E in equation 1 represents the Young's modulus. For the calculation of the equivalent compliance, E is chosen such that it matches the lowest value that is possible with the material groups that can be processed with the production process (Criterion 2). This is done as to obtain a measure for the highest possible compliance that could be acquired with the manufacturing process under consideration. Each of the aforementioned material-groups is assigned its own representative E -value: S: 210 GPa [8], T: 110 GPa [8], A: 70 GPa [9], CP: 1.8 GPa [10], EP: 3.0 GPa [11], C: 120 GPa [12]. With equation 1 a value for the compliance can be calculated such that the different production techniques can be compared to each other. A minimum compliance value of 1 m/N is set as the minimally required attainable

compliance. Manufacturing processes that show compliance values lower than 1 m/N are rejected. This compliance value of 1 m/N is chosen such that it roughly matches the compliance value of a steel leaf spring with a length 0.1 m, a thickness 0.1 mm and a width of 20 mm [13].

Criterion 4: Can thin-walled features be obtained with the manufacturing process?

Thin-walled features are here defined to have a minimal aspect ratio of 1:20 between the major and the minor geometrical dimensions. The 1:20 ratio is chosen quasi-arbitrary; no strict rules on the definition of thin-walled elements for compliant mechanisms exist. An aspect ratio of 1:20 is however adhered to in literature [14]. When aspect ratios of 1:20 cannot be achieved, the manufacturing method will not be further considered.

The first 4 criteria focus on the possibilities of obtaining compliant regions within the compliant mechanisms that will be produced. The following three criteria look at the shape forming possibilities and the induced residual stresses that are associated with each manufacturing processes.

Criterion 5: Is the manufacturing process a shape forming process?

A shape forming manufacturing process is here defined as a manufacturing process in which the base material can be shaped into a 2D or 3D geometry that includes geometrical features. Shape forming to some degree is necessary to acquire compliant mechanisms. Without this shape forming option only the shape of the base material or that of a flat plate can be obtained. Although it is likely that internal stress fields (and therewith resulting strains) can be obtained with non-shape forming production processes as well, it will be hard to obtain functional compliant mechanism with this. For this reason non-shape forming manufacturing processes will be rejected from further consideration.

Criterion 6: What are the typical residual stress magnitudes that can be reached with the manufacturing process?

To realize a stability state transformation, significant stress magnitudes are required. The stresses in the compliant mechanism are ought to result in strains that are of such magnitude that this stability state transformation can occur. The different manufacturing methods cannot be solely assessed on their (residual) stress inducing potential; a certain amount of

stress will yield different strains for different materials. For this reason the acquired residual stress values are normalized with the Young's modulus of the respective material for which the residual stress is found. The result from this will be an equivalent residual strain value. The equivalent residual strains of the different manufacturing methods can be better compared to each other. When for a specific manufacturing method no residual stress value is found in literature, the literature searching scope is broadened to also include reporting on production shrinkages and warping magnitudes.

A minimally required equivalent residual strain is set to 1%. With this minimum residual strain it is expected that an alteration in the stability behaviour is possible. Manufacturing methods that cannot reach equivalent residual strains of 1% or higher are deemed to be insufficient for the scope of this study.

Criterion 7: What is the cause of the residual stress?

Several different phenomena can cause residual stresses and strains in workpieces that are produced. The phenomena that are considered in this work are:

TG: Temperature Gradient - Manufacturing processes always have a certain time-dependency; not all material of the part that is manufactured is instantaneously processed. Rather, the processing is executed sequentially (as in many additive manufacturing methods) or subject to a gradual cooling process (for e.g. moulding and casting techniques). When the manufacturing process poses a thermal input onto the manufactured part, this will evidently lead to temperature gradients over the workpiece. Thermal gradients directly lead to spatial differences in thermal expansion/shrinkage for different volume elements of the part. This results in the creation of residual stresses and strains.

TGM: Temperature Gradient Mechanism - The TGM mainly occurs in manufacturing processes in which a focused thermal source is applied to the processed workpiece. Laser-based manufacturing processes for example heavily experience the TGM. During incidence of the energy bundle to the workpieces' material, the top layer (the heat affected volume) will experience thermal expansion, while the material below the top layer remains unaffected. This will lead to compressive stresses directly around the heat affected volume, eventually leading to plastic deformations at the front of this heat affected volume. When the energy bundle moves away, the material cools down and subsequently it experiences thermal shrinkage. Due to the plastic deformations that have taken place, this thermal shrinkage will now be accompanied by the rise of tensile stress in the heat

affected volume.

Cr: Crystallization - The crystal composition of a material can change under the influence of pressure or temperature. The latter factor especially can occur during the manufacturing processes that are considered in this review. Different solid crystal phases all have different packings and densities [15]. When the crystal composition of a system is (partially) altered this will lead to internal residual stresses. These stresses are mainly on the micro and meso scale and are therefore not of major influence on macroscopic straining behaviour [15]. On the contrary, when considering polymeric materials, the crystallization of amorphous regions within semi-crystalline parts leads to an alteration in the relative crystalline and amorphous volume fractions. These altered volume fractions result both in a change of the total (macro) workpiece volume, as well as in the rise of residual stresses.

SM: Shape Memory - Some polymeric and metal materials show the shape memory effect. These materials can change their shape between an original shape and a -stimulus induced- deformed shape. Under the influence of an activation stimulus the memory is activated, resulting in deformational behaviour that is either permanent or temporary.

SiS: Sintering Shrinkage - When material is sintered it experiences densification under the influence of heat (or in some cases pressure). As the thermal distribution within a material volume is not instantaneously homogeneous during sintering (i.e. a manifestation of the TG principle) this can result in internal residual stresses.

SS: Solidification Shrinkage - The density of the liquid form of material is different than the density of the solid form of that same material. Manufacturing processes that use liquid material to obtain solid workpieces (e.g. casting and moulding) solidify gradually. This gradual solidification process results in residual stresses due to its non-homogeneous nature. Solidification shrinkage is often, but not always, in close relation to the existence of the TG.

PD: Plastic Deformation - When (heated) solid material is deformed by e.g. forming techniques, evidently plastic deformation occurs. Due to plastic deformations residual stresses can arise.

are shown in table 2. Entries represented in **red** indicate that the minimum criterion requirement as set in section 2 is not met. For some entries in table 2 no information is found; the herewith existing information gaps are indicated by **?**. Furthermore, due to the nature of some manufacturing processes, not all set criteria are applicable to all processes. If a criterion is not applicable, this is indicated with **–** in table 2. The column **Contender?** indicates whether the manufacturing process passes all minimum requirements as set in section 2. When a process is deemed to not be a contender, the column **Reason** provides the criteria based on which this decision is made.

3. Results

The considered manufacturing processes, together with the results to all respective assessment criteria,

Table 2: The assessment table

Process ↓ — Criterion →	1	2	3	4	5	6	7	Contender?	Reason
Selective Laser Sintering	0.6 mm [16, 17]	CP [18], EP [19]	17.1 m/N	✓ [19]	✓	0.0032 [20]	TG, TGM [21], Cr [20]	X	6
Selective Laser Melting	0.5 mm [22]	A, T, S [22]	0.91 m/N	✓ [23]	✓	0.0020 [24, 25]	TG, TGM [26]	X	3,6
Direct Metal Laser Sintering	0.5 mm [16, 27]	A, T, S [28]	0.91 m/N	✓ [27]	✓	0.0029 [29]	TG, TGM [29]	X	3,6
Direct Metal Deposition	0.6 mm [30]	A, T, S [30]	0.44 m/N	✓ [31]	✓	0.0015 [32]	TG, TGM [32]	X	3,6
Selective Laser Cladding	100 μm [33]	A, T, S [34]	571.4 m/N	✓ [33]	✓	0.0010 [35]	TG, TGM [35]	X	6
Fused Filament Fabrication	0.8 mm [36]	CP, EP [36]	5.43 m/N	✓ [37]	✓	0.35 [38]	TG [36], Cr [39], SM [40]	✓	—
Robocasting	100 μm [41]	A, S, CP [42], T [43]	22222 m/N	✓ [44]	✓	0.16 [45]	TG [46], SIS [43]	✓	—
Ballistic Particle Manufacturing	?	CP [47]	?	?	?	?	?	X	1,3,4,6,7
Multi-Jet Modelling	0.5 mm [48, 49]	CP [48, 49]	3506 m/N	✓ [49]	✓	0.016 [50]	TG, TGM, Cr [50]	✓	—
Electron Beam Manufacturing	0.5 mm [51]	T [52]	0.58 m/N	✓ [51]	✓	0.00011 [53]	TG, TGM [53, 54]	X	3,6
Wire Arc Additive Manufacturing	2 mm [55]	A [56], T, S [57]	0.0036 m/N	✓ [57]	✓	0.0031 [58, 59]	TG, TGM [60]	X	3,6
Stereolithography	0.1 mm [61]	CP, EP [62]	22222 m/N	✓ [61]	✓	0.0045 [63]	SS [63]	X	6
Injection Moulding	0.8 mm [64]	CP, EP [65]	5.4 m/N	✓ [65]	✓	0.033 [66]	TG [67, 68], Cr [69]	✓	—
Compression Moulding	0.8 mm [70]	CP, EP [71]	5.4 m/N	✓ [70]	✓	0.026 [72]	TG [73], Cr [69]	✓	—
Sandcasting	3 mm [74]	A, S [75]	0.0007 m/N	✓ [74]	✓	0.06 [76]	TG, SS [76]	X	3
Plaster Mold Casting	0.6 mm [77]	A [78]	0.44 m/N	✓ [79]	?	?	TG, SS [80]	X	3,6
Investment Casting	0.6 mm [77]	A, S [81]	0.44 m/N	✓ [82]	✓	0.031 [83]	TG, SS [80]	X	3
Permanent Mold Casting	3 mm [77]	A, S, T [84]	0.0007 m/N	✓ [84]	✓	0.07 [85]	TG, SS [80]	X	3
Continuous Casting	1.5 mm [86]	A [87], S [86], T [88]	0.011 m/N	X	X	?	TG [89]	X	3,4,5,6
Die Casting	0.5 mm [90]	A [77]	0.91 m/N	✓ [90]	✓	0.065 [91]	TG, SS [80]	X	3
Extruding	1 mm [92]	A, S, T [93], CP, EP [94], TG [95]	2.22 m/N	✓ [96]	✓	0.0019 [97]	PD [97]	X	6
Laser forming/bending	—	A, T, S [98]	—	✓ [98]	✓	0.032 [99]	PD, TGM [98]	✓	—

4. Manufacturing process assessment and selection

In section 3 the results to all criteria as mentioned in section 1 are shown. Based on these tabulated results a single manufacturing process can be chosen that fits the purpose of this thesis project best. A first selection is done based on the Contender? column. This column shows whether a manufacturing process can be directly excluded from the study based on the results for one or more of the assessment criteria. Exclusion is here indicated by X. When all assessment criteria are met this is indicated with ✓ in the Contender? column. Based on this first selection, 6 manufacturing processes remain. These processes are: FFF, RC, MJM, IM, CM and LF.

When looking at criterion 6 in table 2 it can be seen that solidification shrinkage of metals (SS), the combination of the shape memory effect and crystallization (SM and Cr) of polymers and the sintering (SiS) of ceramics yield the largest equivalent residual strain values. The combination of SM-strain and Cr-strain for polymers gives the largest value in this regard, with reported shrinkages of up to 35% obtained with the FFF printing technique [38]. This makes FFF an interesting contender for the use in this thesis work. As additional benefits both the shrinkage magnitude and the shrinkage direction can be steered with the FFF technique by selecting the right printing parameters [38,100]. This steering-property is far less abundant in e.g. moulding or casting techniques. The goal of this thesis work is to obtain tailorable stress fields with which significant and predefined material strains can be obtained. FFF seems to be a well fitting technique for this. Moreover, the FFF manufacturing process is widely available and has very low operational costs [101]. This makes this production process an even more interesting option for the current work.

References

- [1] P. Stavropoulos, P. Foteinopoulos, A. Papacharalampopoulos, and G. Tsoukantas. Warping in slm additive manufacturing processes: estimation through thermo-mechanical analysis. *The International Journal of Advanced Manufacturing Technology*, 104(1):1571–1580, 2019.
- [2] M.M. El-Khabeery and M. Fattouh. Residual stress distribution caused by milling. *International Journal of Machine Tools and Manufacture*, 29(3):391–401, 1989.
- [3] N.S. Rossini, M. Dassisti, K.Y. Benyounis, and A.G. Olabi. Methods of measuring residual stresses in components. *Materials & Design*, 35:572–588, 2012.
- [4] B.K. Nagesha, A.K. Tigga, S. Barad, and S. Anand Kumar. Influence of post-processing techniques on residual stresses of slm processed hpngv. *Journal of Manufacturing Processes*, 66:189–197, 2021.
- [5] A.F.M. Arif, B.S. Yilbaz, and B.J. Abdul Aleem. Laser cutting of thick sheet metals: Residual stress analysis. *Optics & Laser Technology*, 41(3):224–232, 2009.
- [6] L.L. Howell. *Compliant Mechanisms*. John Wiley & Sons, inc., 2001.
- [7] Plasticut. Differences between commodity & engineering plastics. <https://www.plasticut.com.au/differences-between-commodity-engineering-plastics/>. Accessed: 26-09-2022.
- [8] Kobelco. Characteristics. <https://www.kobelco.co.jp/english/titan/characteristic/>. Accessed: 26-09-2022.
- [9] Engineering Toolbox. Young's modulus, tensile strength and yield strength values for some materials. https://www.engineeringtoolbox.com/young-modulus-d_417.html. Accessed: 26-09-2022.
- [10] A. Hassan, H. Balakrishnan, and A. Akbari. *Polylactic Acid Based Blends, Composites and Nanocomposites*. Springer Berlin Heidelberg, 2013.
- [11] Omnexus. Modulus of elasticity. <https://omnexus.specialchem.com/polymer-properties/properties/young-modulus>. Accessed: 26-09-2022.
- [12] Kyocera. Stiffness (young's modulus). <https://global.kyocera.com/prdct/fc/list/tokusei/gousei/index.html>. Accessed: 26-09-2022.
- [13] Tribology ABC. Calculator for leaf springs. https://www.tribology-abc.com/calculators/t14_9.htm. Accessed: 26-09-2022.
- [14] M. Wang, D. Ge, L. Zhang, and J.L. Herder. Micro-scale realization of compliant mechanisms: Manufacturing processes and constituent materials—a review. *Chinese Journal of Mechanical Engineering*, 34:85, 2021.
- [15] D. Liu and P.E.J. Flewitt. Raman measurements of stress in films and coatings. *Spectroscopic Properties of Inorganic and Organometallic Compounds*, 45, 2014.
- [16] Xometry. What is the smallest feature that you can print? <https://support.xometry.com/hc/en-us/articles/217723698-What-is-the-smallest-feature-that-you-can-print->. Accessed: 26-09-2022.
- [17] Protolabs.com. Design guidelines: Selective laser sintering (sls). <https://www.protolabs.com/services/3d-printing/selective-laser-sintering/design-guidelines/>. Accessed: 26-09-2022.
- [18] Materialise. Design for additive manufacturing. <https://www.materialise.com/en/academy/industrial/design-am>. Accessed: 26-09-2022.
- [19] HUBS. What is sls 3d printing? <https://www.hubs.com/knowledge-base/what-is-sls-3d-printing/>. Accessed: 26-09-2022.
- [20] F. Shen, W. Zhu, K. Zhou, and L. Ke. Modeling the temperature, crystallization, and residual stress for selective laser sintering of polymeric powder. *Acta Mechanica*, 232:3635–3653, 2021.
- [21] N. Rudolph and R. Sehling. Estimating residual stresses in sls parts using dma. <https://analyzing-testing.netzsch.com/en/blog/2021/estimating-residual-stresses-in-sls-parts-using-dma>. Accessed: 26-09-2022.
- [22] Materialise. Metal 3d printing. https://www.materialise.com/en/industrial/3d-printing-technologies/metal-3d-printing?gclid=CjwKCAiAhreNBhAYEiwAFGGKPKonomZ9S8CArnA0hmrIU5eRSJ3cAamz_Z8PYpKmuY-YNKB2zaCeRoCFMcQAvD_BwE. Accessed: 26-09-2022.
- [23] L. Yang, H. Gong, S. Dilip, and B. Stucker. An investigation of thin feature generation in direct metal laser sintering systems. *Conference: 25th Annual International Solid Freeform Fabrication Symposium*, 2014.
- [24] M. Shiomu, K. Osakada, K. Nakamura, T. Yamashita, and F. Abe. Residual stress within metallic model made by selective laser melting process. *CIRP Annals*, 53(1):195–198, 2004.
- [25] T. Simson, A. Emmel, A. Dwars, and J. Böhm. Residual stress measurements on aisi 316l samples manufactured by selective laser melting. *Additive Manufacturing*, 17:183–189, 2017.
- [26] K. Kempen, L. Thijs, B. Vrancken, S. Bols, J. van Humbeeck, and J.P. Kruth. Producing crack-free, high density m2 hss parts by selective laser melting: Pre-heating the baseplate. *Journal of Manufacturing Science and Engineering*, 136(6):061026, 2014.
- [27] Protolabs.co.uk. Metal 3d printing (dmls). <https://www.protolabs.co.uk/services/3d-printing/direct-metal-laser-sintering/>. Accessed: 26-09-2022.
- [28] EOS. Eos materials overview metal. https://www.eos.info/03_system-related-assets/material-related-contents/material_pdf/eos_materials_overview_metal_en.pdf. Accessed: 26-09-2022.

- [29] I. Yadroitsava and I. Yadroitsev. Residual stress in metal specimens produced by direct metal laser sintering. *Proceedings of International Solid Freeform Fabrication Symposium*, 2015.
- [30] Sculpteo. Direct metal deposition (dmd) fabrication process for metal 3d prints. <https://www.sculpteo.com/en/glossary/dmd-definition/>. Accessed: 26-09-2022.
- [31] T. Amine, J.W. Newkirk, and F. Liou. An investigation of the effect of direct metal deposition parameters on the characteristics of the deposited layers. *Case Studies in Thermal Engineering*, 3:21–34, 2014.
- [32] H. Liu and F. Liou. *New Challenges in Residual Stress Measurements and Evaluation*. IntechOpen, 2019.
- [33] F. Brückner, S. Nowotny, and C. Leyens, editors. *Innovations in laser cladding and direct metal deposition*, volume 8239, High Power Laser Materials Processing: Lasers, Beam Delivery, Diagnostics, and Applications of SPIE LASE, San Francisco, CA, USA, 2012. SPIE.
- [34] TWI Global. What is laser cladding technology? <https://www.twi-global.com/technical-knowledge/faqs/what-is-laser-cladding/>. Accessed: 26-09-2022.
- [35] U.O.B. de Oliveira, V. Ocelik, and J.T.M. De Hosson. *Residual stresses in Co-based laser claddings investigated by lab X-rays and synchrotron diffraction techniques*. WIT Press, 2005.
- [36] HUBS. What is fdm (fused deposition modeling) 3d printing? <https://www.hubs.com/knowledge-base/what-is-fdm-3d-printing/>. Accessed: 26-09-2022.
- [37] Formlabs. Minimum wall thickness for 3d printing. <https://formlabs.com/blog/minimum-wall-thickness-3d-printing/>. Accessed: 26-09-2022.
- [38] A.R. Rajkumar and K. Shanmugam. Additive manufacturing-enabled shape transformations via fff 4d printing. *Journal of Materials Research*, 33(24):4362–4376, 2018.
- [39] B. Wijnen, P. Sanders, and J.M. Pearce. Improved model and experimental validation of deformation in fused filament fabrication of polylactic acid. *Progress in Additive Manufacturing*, 3:193–203, 2019.
- [40] Q. Zhang, D. Yan, K. Zhang, and G. Hu. Pattern transformation of heat-shrinkable polymer by three-dimensional (3d) printing technique. *Sci Rep*, 5:8936, 2015.
- [41] P. Miranda. Robocasting - direct ink writing. <https://euroceram.org/en/eu/robocasting-direct-ink-writing/>. Accessed: 26-09-2022.
- [42] E. Feilden, E. García-Tuñón Blanca, F. Giuliani, E. Saiz, and L. Vanderperre. Robocasting of structural ceramic parts with hydrogel inks. *Journal of the European Ceramic Society*, 36(10):2525–2533, 2016.
- [43] C. Oliver-Urrutia, A. Kashimbetova, K. Slámečka, L. Čelko, and E.B. Montufa. Robocasting additive manufacturing of titanium and titanium alloys: A review. *Transactions of the Indian Institute of Metals*, 2022.
- [44] J. Cesarano and S. Grieco. Robocasting: A new technique for the freeform fabrication of near-net-shape ceramics. *Materials Technology*, 12(3-4):98–100, 1997.
- [45] M. Mohammadi, P. Pascaud-Mathieu, V. Allizond, J. Tulliani, B. Coppola, G. Banche, C. Chaput, A. Cuffini, F. Rossignol, and P. Palmero. Robocasting of single and multi-functional calcium phosphate scaffolds and its hybridization with conventional techniques: Design, fabrication and characterization. *Applied Sciences*, 10(23):8677, 2020.
- [46] E. Peng, D. Zhang, and J. Ding. Ceramic robocasting: Recent achievements, potential, and future developments. *Ceramic Additive Manufacturing*, 30(47):1802404, 2018.
- [47] Padt Digital Manufacturing. Ballistic particle manufacturing [bpm]. <https://www.padtinc.com/digital-manufacturing/glossary/ballistic-particle-manufacturing/>. Accessed: 26-09-2022.
- [48] Materialise. Multi jet fusion. <https://www.materialise.com/en/industrial/3d-printing-technologies/multi-jet-fusion/>. Accessed: 26-09-2022.
- [49] Protolabs. Multi jet fusion. <https://www.protolabs.com/services/3d-printing/multi-jet-fusion/>. Accessed: 26-09-2022.
- [50] H.W.B. Teo, K. Chen, V.T. Tran, H. Du, J. Zeng, and K. Zhou. Non-isothermal crystallization behaviour of polyamide 12 analogous to multi-jet fusion additive manufacturing process. *Polymer*, 235(19):124256, 2021.
- [51] J.K. Algardh, T. Horn, H. West, R. Aman, A. Snis, H. Engqvist, J. Lausmaa, and O. Harrysson. Thickness dependency of mechanical properties for thin-walled titanium parts manufactured by electron beam melting (ebm). *Additive Manufacturing*, 12:45–50, 2016.
- [52] 3dnatives. The complete guide to electron beam melting (ebm) in 3d printing. <https://www.3dnatives.com/en/electron-beam-melting100420174/>. Accessed: 26-09-2022.
- [53] M. Galati, G. Rizza, A. Salmi, S. Biamino, C. Ghibauda, P. Fino, and L. Luliano. Residual stress investigation on ti-48al-2cr-2nb samples produced by electron beam melting process. *Procedia CIRP*, 99:336–341, 2021.
- [54] W.P. Syam, H.A. Al-Shehri, A.M. Al-Ahmari, K.A. Al-Wazzan, and M.A. Mannan. Preliminary fabrication of thin-wall structure of ti6al4v for dental restoration by electron beam melting. *Rapid Prototyping Journal*, 18(3):230–240, 2012.
- [55] D. Jafari, T.H.J. Vanecker, and I. Gibson. Wire and arc additive manufacturing: Opportunities and challenges to control the quality and accuracy of manufactured parts. *Materials and Design*, 202:109471, 2021.
- [56] J. Sun, J. Hensel, M. Köhler, and K. Dilger. Residual stress in wire and arc additively manufactured aluminum components. *Journal of Manufacturing Processes*, 65:97–111, 2021.
- [57] Ramlab. Waam 101. <https://www.ramlab.com/resources/waam-101/>. Accessed: 26-09-2022.
- [58] Q. Wu, T. Mukherjee, A. De, and T. DebRoy. Residual stresses in wire-arc additive manufacturing – hierarchy of influential variables. *Additive Manufacturing*, 35:101355, 2020.
- [59] B.A. Szost, S. Terzi, F. martina, D Boisselier, A. Prytuliak, T. Pirling, M. Hofmann, and D.J. Jarvis. A comparative study of additive manufacturing techniques: Residual stress and microstructural analysis of clad and waam printed ti-6al-4v components. *Materials and Design*, 89:559–567, 2016.
- [60] C. Li, Z.Y. Liu, X.Y. Fang, and Y.B. Guo. Residual stress in metal additive manufacturing. *Procedia CIRP*, 71:348–353, 2018.
- [61] Xometry. Stereolithography (sla) 3d printing design tips. <https://xometry.eu/en/sla-3d-printing-design-tips/#:~:text=Embossed%20features%20must%20be%20at,a%20width%20of%200.5mm.> Accessed: 26-09-2022.
- [62] Materialise. Stereolithography. <https://www.materialise.com/en/industrial/3d-printing-technologies/stereolithography/>. Accessed: 26-09-2022.
- [63] D. Karalekas and A. Aggelopoulos. Study of shrinkage strains in a stereolithography cured acrylic photopolymer resin. *Journal of Materials Processing Technology*, 136(1-3):146–150, 2003.
- [64] HUBS. The manufacturing & design guide injection molding. <https://www.hubs.com/guides/injection-molding/>. Accessed: 26-09-2022.
- [65] 3D Systems. Basics of injection molding design. <https://www.3dsystems.com/quickparts/learning-center/injection-molding-basics.> Accessed: 26-09-2022.
- [66] K.M.B. Jansen, D.J. van Dijk, and M.H. Husselman. Effect of processing conditions on shrinkage in injection molding. *Polymer Engineering and Science*, 38(5):838–846, 1998.
- [67] M. Akay and S. Ozden. Predictions of process-induced warpage in injection molded thermoplastics. *Polymer Engineering and Science*, 36(13):1839–1846, 1996.
- [68] D. Choi and Y. Im. Prediction of shrinkage and warpage in consideration of residual stress in integrated simulation of injection molding. *Composite Structures*, 47(1-4):655–665, 1999.

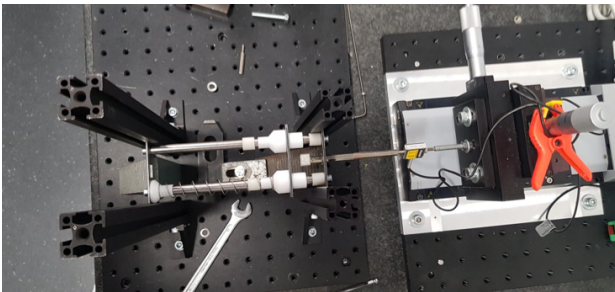
- [69] G. Titomanlio and K.M.B. Jansen. In-mold shrinkage and stress prediction in injection molding. *Polymer Engineering and Science*, 36(15):2041–2049, 1996.
- [70] EngineeringClicks. Compression molding – manufacturing process guide. <https://www.engineeringclicks.com/compression-molding/>. Accessed: 26-09-2022.
- [71] Formlabs. Guide to compression molding from prototyping to mass production. <https://formlabs.com/blog/compression-molding/>. Accessed: 26-09-2022.
- [72] K. Miller and K. Ramani. Process-induced residual stresses in compression molded uhmwpe. *Polymer Engineering and Science*, 39(1), 1999.
- [73] A. Rios, B. Davis, and P. Gramann. Computer aided engineering in compression molding.
- [74] Manufacturing Network. Sand casting - the designers & buyers guide. <https://www.manufacturingnetwork.com/knowledgebase/view/30>. Accessed: 26-09-2022.
- [75] OneMonroe. The 6-step process of sand casting. <https://monroeengineering.com/blog/the-6-step-process-of-sand-casting/>. Accessed: 26-09-2022.
- [76] Haworth Castings. Shrinkage in sand casting. <https://www.haworthcastings.co.uk/news/shrinkage-in-sand-casting>. Accessed: 26-09-2022.
- [77] E.P. DeGarmo, J.T. Black, and R.A. Kohser. *Materials and Processes in Manufacturing*. Wiley & Sons,inc., 2003.
- [78] Thomasnet. All about plaster mold casting - what it is and how it works. <https://www.thomasnet.com/articles/custom-manufacturing-fabricating/all-about-plaster-mold-casting/>. Accessed: 26-09-2022.
- [79] Precisecast. What is plaster mold casting? <https://precisecast.com/what-is-plaster-mold-casting/>. Accessed: 26-09-2022.
- [80] Thomas. Shrinkage in casting: Causes and solutions. <https://www.thomasnet.com/articles/custom-manufacturing-fabricating/shrinkage-casting/>. Accessed: 26-09-2022.
- [81] Impro. Different types of investment casting materials. <https://www.improprecision.com/different-types-investment-casting-materials/>. Accessed: 26-09-2022.
- [82] R. Svenningsson and S. Farre. Thin walled investment castings.
- [83] D. Wang, B. He, S. Liu, C. Liu, and L. Fei. Dimensional shrinkage prediction based on displacement field in investment casting. *The International Journal of Advanced Manufacturing Technology*, 85:201–208, 2016.
- [84] custompart.net. Permanent mold casting. <https://www.custompartnet.com/wu/permanent-mold-casting>. Accessed: 26-09-2022.
- [85] R. Viets, M. Breuer, H. Haferkamp, T. Kruessel, and M. Niemeyer. Solidification process and infrared image characteristics of permanent mold castings. In *Thermosense XXI*, volume 3700, pages 132–140. SPIE, 1999.
- [86] R.I.L. Guthrie and M.M. Isac. Continuous casting practices for steel: Past, present and future. *Metals*, 12(5):862, 2022.
- [87] Leichtmetall. Continuous casting of aluminium. <https://www.leichtmetall.eu/en/aluminium-casting-production/>. Accessed: 26-09-2022.
- [88] T. Tanaka, A. Kuroda, and K. Kurita. Continuous casting of titanium alloy by an induction cold crucible. *ISIJ International*, 32(5):575–582, 1992.
- [89] B.G. Thomas. Review on modeling and simulation of continuous casting. *Special Issue: Modeling and Simulation of Steelmaking*, 89(1):1700312, 2017.
- [90] International Zinc Association. Design rules. https://diecasting.zinc.org/properties/en/design/eng_prop_d_design-rules/. Accessed: 26-09-2022.
- [91] 3ERP. Decreasing shrinkage in metal die-casting. <https://www.3erp.com/blog/decreasing-shrinkage-metal-die-casting/>. Accessed: 26-09-2022.
- [92] Engineering Product Design. Direct metal extrusion design guide – dfm. <https://engineeringproductdesign.com/knowledge-base/how-to-design-parts-for-direct-metal-extrusion-and-dfm-guidelines>. Accessed: 26-09-2022.
- [93] Industrial Extrusion Machinery. Hot extrusion. http://www.industrialextrusionmachinery.com/extrusion_process_hot_extrusion.html. Accessed: 26-09-2022.
- [94] D. Kopeliovich. Extrusion of polymers. https://www.substech.com/dokuwiki/doku.php?id=extrusion_of_polymers. Accessed: 26-09-2022.
- [95] ToolNotes. Ceramic extrusion. <http://toolnotes.com/home/production-processes/ceramic-processes/shaping-and-forming-ceramics/ceramic-extrusion/>. Accessed: 26-09-2022.
- [96] F.F. Kraft and J. Kochis. Hot extrusion of thin-wall multichannel copper profiles. *Journal of Manufacturing Science and Engineering*, 135(6):061008, 2013.
- [97] P. Landkramer, A. Jobst, C. Kiener, P. Steinmann, and M. Merklein. Investigations on residual stress generation in full-forward-extrusion. *Production Engineering*, 13:169–180, 2019.
- [98] H. Shen and F. Vollertsen. Modelling of laser forming – an review. *Computational Materials Science*, 46(4):834–840, 2009.
- [99] J. Magee, K.G. Watkins, and W.M. Steen. Advances in laser forming. *Journal of Laser Applications*, 10:235, 1998.
- [100] L. Kačergis, R. Mitkus, and M. Sinapius. Influence of fused deposition modeling process parameters on the transformation of 4d printed morphing structures. *Smart Materials and Structures*, 28:105042, 2019.
- [101] FACT.MR. 3d printing materials market outlook (2021–2031), 2022.

Appendix B: The shrinkage measurement device PI-stage tests

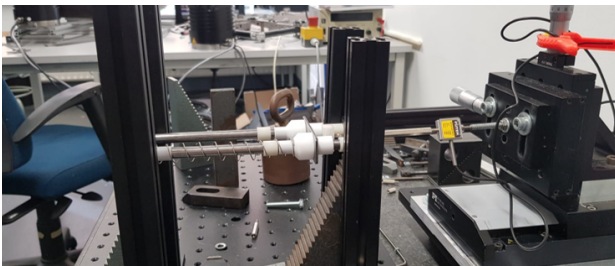
To validate the effective spring stiffness as experienced by the PLA samples, and to establish a value for the static and dynamic friction forces, several measurements on the shrinkage measurement device (SMD) have been performed. These measurements are done on a PI M-505 translational stage (Physik Instrumente GmbH & Co. KG, Karlsruhe, Germany). Attached to this translational stage is a LSB200 low capacity load cell (FUTEK Advanced Sensor Technology, Inc., Irvine, CA, USA). A general explanation on the working principle of the SMD can be found in chapter 2, section 2.1.1.

1. The setup

Before the measurements can be executed, first the SMD needs to be properly constrained. Without these constraints the device might translate or rotation during the measurements, giving inaccurate test results. For constraining of the device, several Thorlabs (Newton, NJ, USA) components are used, all mounted to a Thorlabs aluminium breadboard. The setup that is built is shown in figure 1.



(a) Top view of the test setup.



(b) Side view of the test setup.

Figure 1: The SMD test setup for testing with the PI translational stage.

The outer edges of both end plates of the SMD are slid into 4 separate 25 mm Optical Construction Rails that are bolted to the breadboard. The two leftmost construction rails in figure 1a are slightly rotated be-

fore fastening. This is done to put minute tension on the SMD, hereby constraining the system in the direction of translational motion of the PI-stage. To get the approximate height alignment, the SMD is put on two equal-height steel step blocks. For the fine height-alignment the ratchet thimble screw of the PI-stage is used. The different interfaces that connect the PI-stage and the SMD have been 3D printed (PLA) or laser cut (steel). Connection with the PI-stage is obtained by M3 bolts.

2. Spring stiffness

In the first test on the PI-stage the actual effective spring stiffness is determined. Two springs, each with a stiffness of 0.085 N/mm, are used here. According to equation 1 for the equivalent parallel spring stiffness, the total spring stiffness should be 0.17 N/mm.

$$K_{eq} = K_1 + K_2 = 2K \quad (1)$$

Both springs that are used in the SMD are tested separately. The test setup that is used for this measurement is shown in figure 2. The force-displacement graphs of both springs are added to get the equivalent force-displacement curve. This curve is shown in figure 3. The maximum applied PI-stage compression is 10 mm. This compression magnitude is larger than the maximum compression (6%) that is found during the SMD tests as presented in chapter 2. This assures that the here obtained values are valid to all tests that are performed in chapter 2.



Figure 2: Test setup for measurement of the stiffness of a single spring.

In figure 3 it can be seen that the compression path is almost perfectly linear. A linearised line, obtained with the least squares method, is added to this graph for comparison.

During sample testing as presented in chapter 2, the compression stiffness is of most importance as this is the stiffness that the shrinking PLA must counter-

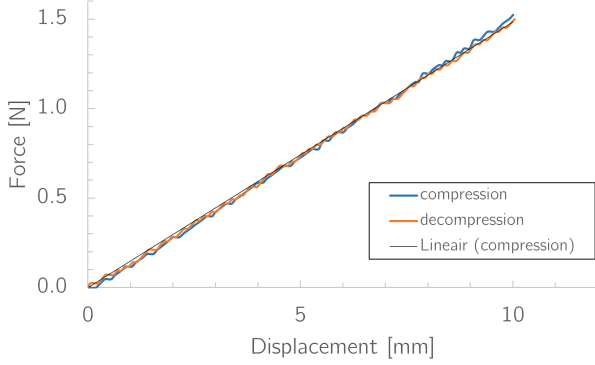


Figure 3: Equivalent force-displacement curve for the two combined springs.

act. The linearised equivalent stiffness of the springs is calculated by making use of equation 2.

$$K_{eq,real} = \frac{\Delta F_{eq,linearised}}{\Delta disp,linearised} \quad (2)$$

When entering the linearised compression values into equation 2, a $K_{eq,real}$ of 0.148 N/mm is found. This is approximately 87% of the K_{eq} that is obtained with equation 1.

As a second test both springs have been attached to the SMD and the moving cart is now actuated by the PI-stage. In this test friction effects due to guiding rail - cart interactions are included. The result of this test is shown in figure 4. When again using equation 2, a compressive linearised $K_{eq,real}$ of 0.158 N/mm is now found.

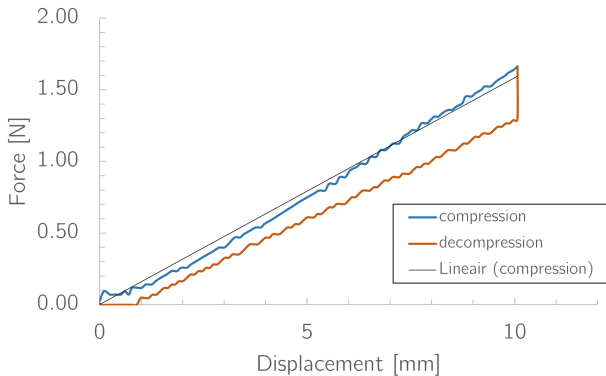


Figure 4: Force-displacement curve for the SMD.

The increase in compression stiffness between figures 3 and figure 4 is peculiar. A net difference of 0.010 N/mm is found while no changes to the stiffness elements are made. It appears that within the SMD a displacement dependent friction element is at play. This displacement dependent friction hereby contributes as pseudo-stiffness to the total stiffness figure. Possible causes for this pseudo-stiffness could be e.g. non-parallelity of the two guiding rails, non-straightness of the individual guiding rails or non-concentricity of either of the individual guiding rails. A further investigation into the root cause of this occurrence has not been conducted.

The hysteresis loop formed by the compression and decompression paths is larger in figure 4 compared to figure 3. This increase in hysteresis can be attributed to the non-conservative friction forces that need to be accounted for in the fully assembled SMD. Once more it is emphasized that a displacement dependency appears to be present here. It can be seen that for the compression path initially a small step in applied force is required. This step, that can be found around a displacement of 0.1 mm, indicates the overcoming of the static friction of the system. A more elaborate test on this is presented in section 3.

3. Friction

The SMD's moving cart slides over steel guiding rails by the means of PTFE sleeve bearings. The addition of these bearings inherently adds both static and dynamic friction to the motion path. The friction effects are directly experienced by the shrinking PLA and it is therefore important to have these friction force magnitudes available. For this reason a test on the PI-stage is performed to find the magnitude of both the static and the dynamic friction forces. N.B. for these tests the springs are removed from the SMD. The results of this test are shown in figure 5.

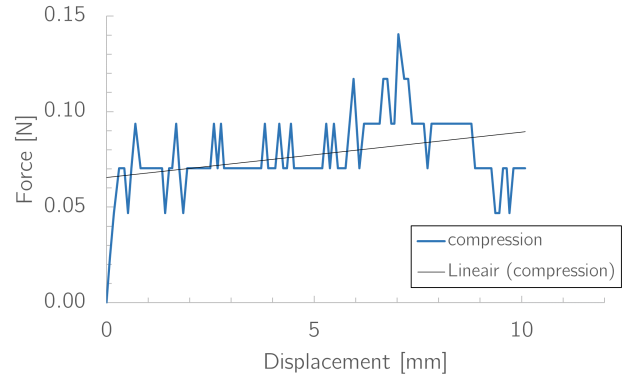


Figure 5: Friction test for the SMD.

As the measurement resolution of 0.02343 N is in the same order of magnitude as the friction values, no definitive conclusions can be drawn from this test. From figure 5 it is found that the frictional effects are only of a limited magnitude. A maximum friction force spike of 0.141 N is found. The average dynamic friction force over the cart's motion range is 0.077 N. The linearised trend of the dynamic friction force is added to figure 5 as well. This trend is again obtained with the least squares method. When looking at this line, an increase in the frictional force over the displacement range is found. This observation confirms the suspicion of the presence of pseudo-stiffness in the SMD. When using equation 2 on this linear trend, a pseudo-stiffness value of 0.006 N/mm is found. As the resolution of the force measurements is relatively low, the value of 0.006 N/mm can only be considered to be a mere approximation of the true value. This value is

however in the same ballpark as the before mentioned 0.010 N/mm.

A peak at the onset of the motion range corresponding to the overcoming of static friction is not clearly observed in figure 5. Possibly this force peak falls within the load cell's measurement resolution and is therefore not distinguishable in figure 5. It could also mean that the static frictional force is of lower magnitude than the dynamic frictional force. Interestingly, the static friction force peak was however observed in figure 4. The combination of non-lubricated steel with PTFE yields a dynamic friction coefficient between 0.1 and 0.15 and a static friction coefficient of 0.08, according to literature [1]. The total mass of the steel cart and the two PTFE sleeve bearings is 35g, based on the CAD model. This mass equals a weight of 0.343 N. The formula for coulomb friction as shown in equations 3 and 4 [1] is used to compare the theoretical friction values to the values as presented in figure 5. In equations 3 and 4, $F_{f,\dots}$ is the dry frictional force (either static or dynamic), μ_{\dots} is the coefficient of friction (either static or dynamic) and F_n is the exerted normal force.

$$F_{f,static} \leq \mu_{static} F_n \quad (3)$$

$$F_{f,dynamic} = \mu_{dynamic} F_n \quad (4)$$

The normal force provided by the cart assembly is fully defined by its own weight. As the cart is symmetrically carried by two guiding rails, the normal force on each carrying interface is the total cart's weight halved. This gives a F_n value of 0.171 N. Inserting this value into equation 4 gives a $F_{f,dynamic}$ that lies between 0.017 N and 0.026 N. A $F_{f,static}$ of 0.014 N is found by using equation 3. All results are summarized in table 1.

Table 1: Comparison of results of the friction force measurements and theoretical friction force values.

	$F_{f,static}$ [N]	$F_{f,dynamic}$ [N]
Measurement (avg)	≤ 0.077	0.077
Theoretical (avg)	0.014	0.022

The theoretical maximum static friction force appears to be lower than the measurement resolution of the PI-stage. Moreover, the theoretical value for $F_{f,static}$ is lower than the theoretical value for $F_{f,dynamic}$. These two factors explain why the measured static friction force is not distinguishable in figure 5. The measured dynamic friction value is roughly 3 times larger than the value that is expected based on the theoretical value. The SMD has two collinear guiding rails for a single degree of freedom. This implies the existence of over-constraints in the linear guiding system. The SMD has two sleeve bearings that slide over the guiding rails, each providing 4 constraints. To obtain a single degree of freedom with the SMD, 5 constraints are minimally needed. This means that the sliding cart has 3 over-constraints in

total. As a result of these over-constraints, jamming can occur. Due to the jamming phenomenon extra frictional force might be experienced by the actuator.

During its intended operation the SMD is heated in the oven. Consequently radial expansion of both the PTFE sleeve bearings as well as the steel guiding rail will occur. As the thermal expansion coefficient of PTFE is roughly an order of magnitude larger than that of steel [2], no thermally-induced locking is expected to take place. The chances on thermally-induced jamming might however increase due to this. The risks and consequences of thermally-induced and mechanically-induced jamming are attempted to be reduced by accurate manufacturing, attachment of the pulling force in the exact centreline of the cart and by having elongated sleeve bearings.

References

- [1] A. van beek. *Advanced Engineering Design*. TU Delft, 2015.
- [2] Engineering ToolBox. Thermal expansion - linear expansion coefficients. Accessed: 06-09-2022.

Appendix C: The demonstrator in detail

In chapter 2 a demonstrator is presented. This demonstrator is created and used to show that post-print heat introduction to FFF printed PLA is able to result in significant material shrinkage. With this shrinkage a prestress can be applied to the system with which a permanent stability switch can be obtained. Details and design considerations about the demonstrator are provided in this appendix.

1. Design choices & design iterations

During the design phase of the demonstrator several iteration steps are made. The design process of the demonstrator is discussed in this section.

Demonstrator version 1

The working principle of the first version of the planar twisting demonstrator is shown in figure 1. By printing the middle beam (orange) with a relatively high printing speed and the outer beams (blue) with a lower printing speed, a relative shrinkage difference will start to exist when the material is heated. The middle beam shows a relatively large shrinkage, whereas the outer beams will have a less significant shrinkage. The three PLA beams are interconnected by clamping them between rigid aluminium beams. By this rigid connection, the beam with the largest shrinkage will impose a compressive force on the beams that show a lower shrinkage. When this imposed compressive load surpasses the critical buckling load of the outer beams, the demonstrator will show an out of plane twist. The result of this twisting motion is a relative rotation between the two aluminium beams, as depicted in figure 1b.

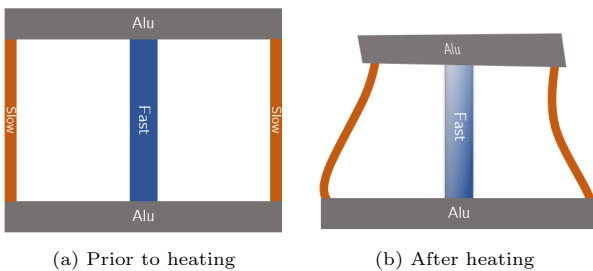


Figure 1: Representation of the working principle of the planar twisting demonstrator version 1.

A preliminary ANSYS APDL simulation on this demonstrator has been made. The result of this simulation can be found in figure 2. Here it can be seen that by shrinkage of the middle beam the aforementioned twisting motion can be realised. An elaboration on the APDL model is provided in section 2 of this appendix.



Figure 2: Preliminary APDL simulation of the planar demonstrator version 1.

A prototype of this first demonstrator version is built. The middle beam is printed with a printing speed of 80 mm/s. The outer beams both are printed with a printing speed of 10 mm/s. Geometrically all three beams are of equal size; the width is 10 mm, the length is 150 mm and the thickness is 1 mm. Both outer beams are placed on a distance of 75 mm from the middle beam. The complete assembly is put in a preheated oven at 110°C for a duration of 45 minutes. The result after heating is shown in figure 3. Unfortunately it appeared that all beams showed a different shrinkage magnitude than was expected. The shrinkage distribution over the different beams showed an almost linearly descending amount of shrinkage from top to bottom in figure 3. With this shrinkage distribution no out of plane rotation was obtained. Moreover it is found that the top beam in figure 3 has locally buckled during the heating cycle.

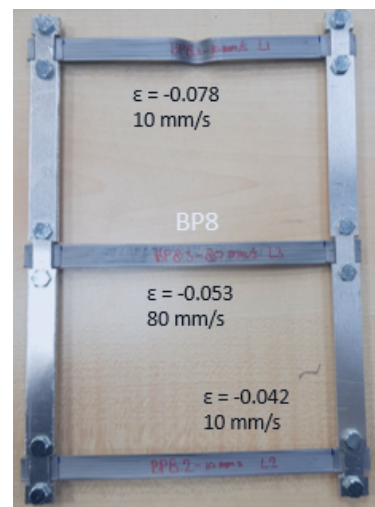


Figure 3: Post-heating results for planar demonstrator version 1.

An explanation for the shrinkage behaviour can be found in the fundamentals of the PLA material shrinkage. As the PLA is gradually heated, at some point it surpasses its glass transition temperature ($T_g - 50^\circ\text{C}$ [1]). Heating above this T_g is a prerequisite to enable the shape memory effect and therewith the accompanying material shrinkage. Another effect that starts occurring above T_g is the vast reduction of material stiffness in both the axial and the transverse (bending) directions. For polymeric materials this is an inherent consequence of heating material above the T_g . During heating of demonstrator version 1, the middle beam tries to shrink more than the outer two beams. Consequently the two outer beams experience an initially equal axial compressive force. Due to small clamping errors and/or production errors, one of the two outer beams might have a slightly lower critical buckling load. As both the axial and the transverse stiffnesses are greatly reduced in the rubbery state, the compressive force might result in buckling already at extremely low compressive forces. The top beam in figure 3 seems to have had a lower critical buckling load than the lowest beam. This top beam buckled first, hereby even further reducing its axial stiffness. The lowest beam has a relatively higher axial stiffness than the top beam while the middle beam proceeds to shrink. As a result of this shrinking of the middle beam, the beam with the lowest axial stiffness will only further be compressed. A schematic representation of this can be found in figure 4.

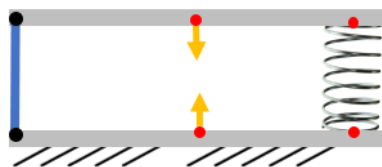


Figure 4: Schematic representation of demonstrator version 1, in which the outer two PLA beams show a different axial stiffness. The leftmost beam (blue) is stiff and starts functioning as a pivot point for the aluminium beams (grey). The PLA middle beam (orange) proceeds to shrink under the influence of heat. The rightmost PLA beam (spring) has a low stiffness and is compressed.

Demonstrator version 2

To prevent this local buckling phenomenon from happening, it must be ensured that both outer beams preserve equal amounts of stiffness. This also needs to hold during heating of the material. For this reason an iteration on demonstrator version 1 is made (i.e. demonstrator version 2). In this new version the outer beams are interchanged for steel leaf flexures. Furthermore, all dimensions have been reduced to decrease the total weight of the system. With this weight reduction the shrinking PLA needs to provide less force to realize the out-of-plane twisting motion. For this new version the PLA middle beam now has a length of 80 mm, a width of 3 mm and a height of 1

mm. The beam is clamped such that the normal distance between the aluminium bars is 60 mm. The leaf flexures have a thickness of 0.1 mm and a width of 3 mm. The flexures are both placed at a distance of 20 mm from the PLA middle beam. This demonstrator version is shown in figure 5.



(a) Prior to heating.

(b) After heating.

Figure 5: Representation of the working principle of the planar twisting demonstrator version 2.

As shown in figure 5b, both leaf flexures have buckled out of plane after heating in the oven. Buckling of both flexures occurred in the same direction. This same sense buckling poses a rotational moment on both aluminium bars. When the temperature is above the T_g of the PLA, the PLA will barely resist the rotational motion that is induced by this moment. Consequently both aluminium bars rotate. When the temperature reduces to a point sub- T_g this rotation is frozen into the clamped parts of the PLA. This occurrence can be seen in figure 5b. Demonstrator version 2 is thus able to induce stress into the leaf flexures. An out of plane twisting motion of one aluminium bar with respect to the other aluminium bar is however not obtained. Another reason for the system not twisting can be found in the fact that this demonstrator is put in the oven horizontally. Theoretically the shrinking PLA middle beam would impose a twist onto the demonstrator due to the constraints that are provided by the leaf flexures. As the demonstrator is put in the oven horizontally this means that the twist that is induced by the PLA now should also overcome a part of the weight of the aluminium bars, the bolts and the nuts. Moreover, overcoming friction between the aluminium bars and the oven's bottom plate partially takes up the PLA shrinkage potential. The PLA sample cannot provide sufficient force for this and instead of twisting, the flexures both buckle out of plane. Putting demonstrator version 2 upright in the oven will not be the solution to this problem. When the PLA enters the rubbery state, most of its bending stiffness will be lost. Also the thin steel leaf flexures show low amounts of bending stiffness. Due to the weight of the aluminium bars, the bolts and the nuts the system will collapse in the oven when put in upright.

Demonstrator version 3

To get a system that is able to stand upright in the oven, the focus is shifted from a planar demonstrator to a spatial one. This iteration resulted in the

demonstrator **version 3**, which is the final version. This final **version 3** is shown in figure 6. An elaboration on this final demonstrator version can be found in chapter 2, section 2. This demonstrator version is of double symmetric nature, giving 4 connection points for the wire flexures. Double symmetry is mainly opted for because the herewith resulting cross shape (red crosses in figure 6) provide an easy-to-use clamping interface for the torsion machine. Clamping is realised by inserting two M3 bolt-nut combinations into opposing holes in both of the red crosses for each demonstrator. The torsion machine is able to clamp to these bolts.

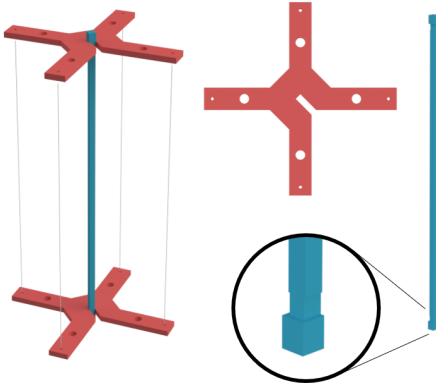


Figure 6: Representation of the final demonstrator.

For the demonstrator it is of importance that the axial stiffness profile is sufficiently low such that the PLA is able to provide the required critical buckling load. Moreover the system should show a sufficiently large bistable range of motion after shrinkage of the PLA. Design parameters that are here of influence are: the wire flexure diameter d , the wire flexure length L and the flexure position with respect to the centre line x . Since the gravity acting on the upper red cross is collinear with the PLA shrinkage direction, the weight of this steel assists in the flexure buckling. In the dimensional design it must be assured that the weight of the upper steel cross can be fully supported by the wire flexures without buckling when being in the upright position. If this would not be the case, the additional effect of the shrinking PLA is redundant and no point regarding the PLA shrinkage potential is proven with this demonstrator. It is evident that the aforementioned design parameters should be chosen such that all requirements will be met.

For considerations regarding the design parameters Euler's Critical Load criterion is used [2]. The formula for this critical load is shown in equation 1. Here P_{cr} is represented in newtons [N], E is the Young's Modulus [Pa] - 210 GPa for spring steel, I is the second moment of inertia [m⁴] of which the formulaic form is shown in equation 2. K is the column effective length which is a dimensionless factor. For this wire flexure situation, K yields a recommended value of 1.2 [3]. L is the column length

[m], which is here considered to be one of the design variables. d in equation 2 is the wire flexure diameter [m], which is one of the other design variables. As there are 4 wire flexures acting in parallel on the steel cross, P_{cr} is premultiplied by 4. This is indicated by the red number in equation 1.

$$P_{cr} = 4 \frac{\pi^2 EI}{(KL)^2} \quad (1)$$

$$I = \frac{\pi d^4}{64} \quad (2)$$

Wire flexure diameter - Since both the wire diameter d and the wire length L are independent from each other according to equation 1, either of the two can be chosen quasi-randomly. For the wire flexures only a select amount of diameters are commercially available. Moreover, the wire flexure rods must be straight. This is not very common for sub-millimetre wire diameters. A straight spring steel wire with a diameter of 0.3 mm is chosen. Herewith design variable d is fixed.

Wire flexure length - The mass of the red steel cross is 12.58g. By multiplying this by the gravitational constant of 9.81 m/s² a weight of 0.123N is found. As the 4 parallelly orientated wire flexures should not buckle under this weight, it can be stated that P_{cr} should at least be greater than 0.123N. When combining this with the now available wire diameter of 0.3mm, equation 1 can be used for determining the maximum allowed wire length under which no buckling occurs. Rearrangement of the equation 1 gives equation 3.

$$L \leq \sqrt{\frac{4\pi^2 EI}{P_{cr}}} \frac{1}{K} \quad (3)$$

When entering all variable values, equation 3 results in a maximum wire flexure length of 0.136 m. With this length the system is on the verge of buckling. To be somewhat further from this limit value, a wire flexure length of 0.1 m is chosen for the demonstrator. A length of 0.1 m gives a P_{cr} of 0.229 N according to equation 1. 0.123 N (53.9%) of the buckling force will be delivered by gravity. This leaves 0.106 N (46.1%) of buckling force to be delivered by the shrinking PLA.

Wire flexure position - The last design parameter is the distance between the wire flexure connection point and the centreline that is defined by the PLA beam. This distance is here indicated by x . As presented in the work by Ahmad [4], distance x has direct influence on the magnitude of the relative rotation angle (θ) between the top and bottom cross for a given middle beam shrinkage. Furthermore this rotation angle is dependent on the previously set wire

length L . The formula presented by Ahmad that relates the system parameters to the rotation angle is shown in equation 4. In this equation S_h is the contraction strain, l_f is the wire flexure length [m] (in this work indicated by design variable L) and l_{fr} is the direct distance [m] between the PLA centreline and the wire flexure connection point on the steel cross (in this work indicated by design variable x).

$$\theta = \frac{180}{\pi} \sqrt{(2S_h - S_h^2) \frac{(l_f)^2}{(l_{fr})^2}} \quad (4)$$

In the here discussed case the wire length l_f is set to 0.1 m, giving l_{fr} as the only variable to prescribe the rotational angle for a given PLA shrinkage S_h . To demonstrate proper functioning of the monostable-to-bistable switch, a one-sided shrinkage induced rotation angle of 45° is desired. The total range of motion equals twice the one-sided rotation, which would thus give a total range of motion of 90° . Although at this point in the process no concrete PLA shrinkage magnitudes are known, preliminary results have shown that non-loaded PLA strips are able to contract to shrinkage levels as much as 20%. It is here assumed that shrinkage in this mildly loaded case will reduce by one order of magnitude compared to shrinkage in the non-loaded case. Based on the preliminary tests this seems to be a realistic scaling. An attainable shrinkage strain of 2% will therefore be used here. When inserting this value into equation 4 with the requirement of having an approximate one-sided rotation angle of 45° , this gives a value for l_{fr} of 0.0255 m. The total direct distance between two opposing wire flexure connections thus equals 0.051m. This value is slightly increased to a distance of 0.055 m in the final demonstrator.

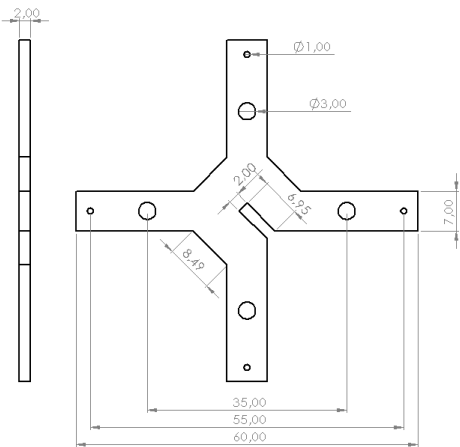


Figure 7: Technical drawing of the steel cross. All dimensions are in [mm].

The steel crosses are lasercut from 2 mm steel sheet material. For the wire flexure connections holes with a diameter of 1 mm are cut in the material. To provide an interface with the torsion machine, holes with a

diameter of 3 mm are added to the crosses as well. M3 bolt-nut combinations can be inserted in these holes. The resulting steel cross dimensions are shown in figure 7.

2. APDL simulation

A finite element (FE) simulation of the demonstrator is made in ANSYS APDL version 2021 R2. The reasons for having this simulation at hand are provided in chapter 2, section 2.2.3. The code that is used can be found in section 3 of this appendix.

In chapter 2 the following information is provided:

From chapter 2, section 2.2.3

“The goal of this simulation is not to model the polymer shrinkage behaviour on a fundamental level. Instead, the material shrinkage is imposed upon the PLA middle beam, hereby forcing a relative rotational motion between the top and bottom crosses. In this manner the kinematic demonstrator behaviour is simulated. The simulation is performed fully in the mechanical domain. Heat-induced PLA shrinkage is realised by assigning a coefficient of thermal expansion (CTE) to the PLA alone; for the steel parts the CTE is set to 0. In the first simulation step the ambient temperature is lowered, resulting in PLA shrinkage only. As a consequence of the PLA shrinkage, the wire flexures will be prestressed. This results in flexure buckling when the critical buckling load is exceeded. After buckling the simulation proceeds to the next step, where the rotational snap-through behaviour of the now bistable demonstrator is simulated.”

To relate a change in ambient temperature to a preferred PLA shrinkage in APDL, a relation between the two must be defined. The definition of this relation is elaborated on here. Variable names are indicated in this text by the `typewriter` font. These exact variable names can also be found in the APDL code that is included in section 3.

First a desired shrinkage value (value between 0-1) is defined in the variable set under the variable name `shrinkage`. `T_delta` (ΔT) is set as the applied change in ambient temperature. This value is set to $100^\circ C$. The formula for linear thermally induced material shrinkage is shown in equation 5. By rewriting this formula an expression for the coefficient of thermal expansion α (CTE) can be found (equation 6).

$$\Delta L = \alpha \Delta T L \quad (5)$$

$$\alpha = \frac{\Delta L}{\Delta T L} \quad (6)$$

α from equation 6 can be expressed in the variables `height`, `shrinkage` and ΔT . Variable `height` represents the initial length of the PLA middle beam. This results in equation 7.

$$\alpha = \frac{\text{height} \times \text{shrinkage}}{\Delta T \times \text{height}} = \frac{\text{shrinkage}}{\Delta T} \quad (7)$$

Thermal shrinkage in APDL is defined by equation 8.

$$\epsilon = \alpha(\text{TUNIF} - \text{TREF}) \quad (8)$$

In this equation `TUNIF` is the uniform temperature that is assigned to all system nodes. In the here performed simulation `TUNIF` is set to the ΔT value of 100°C . `TREF` is the reference temperature that dictates the thermal expansion. When substituting α in equation 8 for equation 7, equation 9 results.

$$\epsilon = \frac{\text{shrinkage}}{\Delta T}(\Delta T - \text{TREF}) \quad (9)$$

In equation 9 variable `TREF` can thus be used to vary the portion of applied material shrinkage of the PLA. When `TREF` equals the value of ΔT , ϵ is 0. When `TREF` equals $2\Delta T$, ϵ will correspond to the strain that follows from the set `shrinkage`. The applied shrinkage portion (prescribed by $\Delta T \leq \text{TREF} \leq 2\Delta T$) is utilized for applying shrinkage in an increasing step-wise manner over multiple time steps. This can be seen in the APDL code (section 3) lines 175 to 294. When the desired shrinkage is not imposed stepwise, the solution will not converge.

3. APDL code

The APDL code for a PLA middle beam of dimensions 2 mm x 2 mm and a desired shrinkage magnitude of 3% is shown below. Between lines 21 to 47 (in blue) material properties for PLA and steel are defined. The material properties for steel are isotropic whereas the material properties for the PLA are modelled as transversely isotropic material. Lines 49 to 112 (green) define the geometric variables of the system. To some nodes a small perturbation (`rand_disp`) is applied to include non-idealities. These non-idealities are required for the system to be able to converge during the buckling stage. Lines 114 to 153 are dedicated to the meshing of the geometry. Line elements are meshed into 50 elements each, as indicated by variable `MESH_NO`. The simulation includes geometric non-linearity. For this reason the `PRERR` APDL-command for finding the percent error in the structural energy norm could unfortunately not be used to perform a meshing convergence study. Therefore a convergence study has been performed of which the results are shown in figure 8. Convergence of the rotational motion of KeyPoint 5 (see figure 9) under axial PLA

shrinkage is used as convergence indicator. The convergence criterion is set to a rotational difference that should be smaller than $1e-4$ for a subsequent increase of the meshing number `MESH_NO`. `MESH_NO` is started at a value of 10 and increased repeatedly by an additional value of 10. Convergence was found when going from 40 divisions per element to 50 divisions per element. A `MESH_NO` value of 50 is therefore used in the APDL simulations.

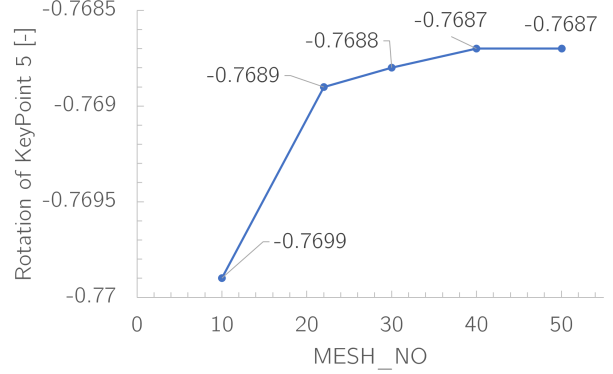


Figure 8: Results of the meshing convergence study.

Boundary conditions are applied in lines 155 to 160. KeyPoint 2 in figure 9 is constrained in all its degrees of freedom. KeyPoint 5 in figure 9 has freedom in the translational and rotational Y-direction. The Y-direction in this model is collinear with the PLA middle beam. `NSUBST` is set to 200 for this model. When the value of `shrinkage` is changed, it sometimes is required to mildly alter the `NSUBST` value by a few steps for the model to be able to converge.

Some additional points of attention for this simulation:

- The analysis type is static (`ANTYPE,STATIC` - line 18).
- Non-linearity is accounted for (`NLGEOM,ON` - line 168).
- 3D 2-node beam elements are used (`ET,1,BEAM188` - line 19).
- During rotation through the bistable path the arc length method is enabled (`ARCLEN,ON,1e-1,1e-5` - line 298).

```

1 /CLEAR,START
2
3 !set variables
4
5 height = 0.1
6 width = 0.055/2
7 shrinkage = 0.03
8 T_delta = 100
9 thermal_coef = shrinkage/T_delta
10 rand_disp = 0.0008
11 LOAD_VALUE = 2
12 MESH_NO = 50

```

```

13 radius_strip = 0.00015
14
15 /PREP7
16 smrt,off
17
18 ANTYPE,STATIC
19 ET,1,BEAM188
20
21 ! MATERIAL PROPERTIES - PLA
22 MPTEMP,1,0
23 MPDATA,DENS,1,,1250
24 MPDATA,EX,1,,4.04E9
25 MPDATA,EY,1,,3.98E9
26 MPDATA,EZ,1,,4.04E9
27 MPDATA,PRXY,1,,0.34
28 MPDATA,PRYZ,1,,0.34
29 MPDATA,PRXZ,1,,0.37
30 MPDATA,GXY,1,,1.5
31 MPDATA,GYZ,1,,1.5
32 MPDATA,GXZ,1,,1.5
33 MPDATA,CTEX,1,,thermal_coef
34 MPDATA,CTEY,1,,thermal_coef
35 MPDATA,CTEZ,1,,thermal_coef
36
37 ! MATERIAL PROPERTIES - STEEL
38 MPDATA,DENS,3,,8000
39 MPDATA,EX,3,,210E9 !195
40 MPDATA,EY,3,,210E9
41 MPDATA,EZ,3,,210E9
42 MPDATA,PRXY,3,,0.3
43 MPDATA,PRYZ,3,,0.3
44 MPDATA,PRXZ,3,,0.3
45 MPDATA,CTEX,3,,0
46 MPDATA,CTEY,3,,0
47 MPDATA,CTEZ,3,,0
48
49 ! DEFINE CROSS SECTIONS
50 ! STEEL BEAM
51 SECTYPE,1,BEAM,RECT,,0
52 SECOFFSET,CENT
53 SECADATA,0.002,0.00675
54
55 SECTYPE,2,BEAM,CSOLID,,0
56 SECOFFSET,CENT
57 SECADATA,radius_strip,10,4
58
59 ! PLA MIDDLE BEAM
60 SECTYPE,3,BEAM,RECT,,0
61 SECOFFSET,CENT
62 SECADATA,0.002,0.002
63
64 ! DEFINE KEYPOINTS
65 K,1,-width,-height/2,0
66 K,2,0,-height/2,0
67 K,3,width,-height/2,0
68 K,4,width,height/2,rand_disp
69 K,5,0,height/2,0
70 K,6,-width,height/2,-rand_disp
71 K,7,width,0+rand_disp/2
72 K,8,-width,0-rand_disp/2
73 K,9,0,-height/2,-width
74 K,10,0,-height/2,width
75 K,11,rand_disp,height/2,-width
76 K,12,-rand_disp,height/2,width
77 K,13,rand_disp/2,0,-width
78 K,14,-rand_disp/2,0,width
79
80 ! Define Lines, index on sections
81 ! STEEL FRAME
82 *GET,Line_ID1,LINE,0,NUM,MAXD
83 L,1,2
84 L,2,3
85 L,4,5
86 L,5,6
87
88 ! PLA
89 *GET,Line_ID2,LINE,0,NUM,MAXD
90 L,2,5
91
92 ! STEEL
93 *GET,Line_ID3,LINE,0,NUM,MAXD
94 L,1,8
95 L,8,6
96 L,3,7
97 L,7,4
98 *GET,Line_ID4,LINE,0,NUM,MAXD
99
100 ! STEEL FRAME ROTATED
101 L,2,9
102 L,2,10
103 L,5,11
104 L,5,12
105 *GET,Line_ID5,LINE,0,NUM,MAXD
106
107 ! STEEL STRIP ROTATED
108 L,11,13
109 L,9,13
110 L,10,14
111 L,14,12
112 *GET,Line_ID6,LINE,0,NUM,MAXD
113
114 ! MESHING OF LINES
115 ! STEEL FRAME
116 TYPE,1
117 SECNUM,1
118 LSEL,S,LINE,,Line_ID1+1,Line_ID2
119 LESIZE,ALL,,MESH_NO
120 MAT,3
121 LMESH,ALL
122
123 ! PLA MIDDLE BEAM
124 TYPE,1
125 SECNUM,3
126 LSEL,S,LINE,,Line_ID2+1,Line_ID3
127 LESIZE,ALL,,MESH_NO
128 MAT,1
129 LMESH,ALL
130
131 ! WIRE FLEXURE
132 TYPE,1
133 SECNUM,2
134 LSEL,S,LINE,,Line_ID3+1,Line_ID4
135 LESIZE,ALL,,MESH_NO
136 MAT,3
137 LMESH,ALL
138
139 ! STEEL FRAME ROTATED
140 TYPE,1
141 SECNUM,1
142 LSEL,S,LINE,,Line_ID4+1,Line_ID5
143 LESIZE,ALL,,MESH_NO
144 MAT,3
145 LMESH,ALL
146
147 ! WIRE FLEXURE
148 TYPE,1
149 SECNUM,2
150 LSEL,S,LINE,,Line_ID5+1,Line_ID6
151 LESIZE,ALL,,MESH_NO
152 MAT,3
153 LMESH,ALL
154
155 ! BOUNDARY CONDITIONS
156 DK,2,ALL
157 DK,5,UX
158 DK,5,UZ

```

```

159 DK,5,ROTZ
160 DK,5,ROTX
161
162 /ESHAPE,1
163 PSTRES,ON
164 FINISH
165 /OUTPUT,SCRATCH
166
167 /SOLUTION
168 NLGEOM,ON
169 ANTYPE,STATIC
170 OUTRES,all,all
171 ARCLN,OFF
172 NSUBST,200
173 TUNIF,T_delta
174
175 ! STEP 1
176 TIME,0
177 TREF,T_delta
178 SOLVE
179
180 ! STEP 2
181 TIME,0.05
182 TREF,T_delta+T_delta*0.001
183 !FK,5,MY,-0.01
184 SOLVE
185
186 ! STEP 3
187 TIME,0.1
188 TREF,T_delta+T_delta*0.005
189 SOLVE
190
191 ! STEP 4
192 TIME,0.15
193 TREF,T_delta+T_delta*0.01
194 SOLVE
195
196 ! STEP 5
197 TIME,0.2
198 TREF,T_delta+T_delta*0.02
199 SOLVE
200
201 ! STEP 6
202 TIME,0.25
203 TREF,T_delta+T_delta*0.04
204 SOLVE
205
206 ! STEP 7
207 TIME,0.3
208 TREF,T_delta+T_delta*0.06
209 SOLVE
210
211 ! STEP 8
212 TIME,0.35
213 TREF,T_delta+T_delta*0.08
214 SOLVE
215
216 ! STEP 9
217 TIME,0.4
218 TREF,T_delta+T_delta*0.1
219 SOLVE
220
221 ! STEP 10
222 TIME,0.45
223 TREF,T_delta+T_delta*0.15
224 SOLVE
225
226 ! STEP 11
227 TIME,0.5
228 TREF,T_delta+T_delta*0.2
229 SOLVE
230
231 ! STEP 12
232 TIME,0.55
233 TREF,T_delta+T_delta*0.25
234 SOLVE
235
236 ! STEP 13
237 TIME,0.6
238 TREF,T_delta+T_delta*0.3
239 SOLVE
240
241 ! STEP 14
242 TIME,0.65
243 TREF,T_delta+T_delta*0.35
244 SOLVE
245
246 ! STEP 15
247 TIME,0.7
248 TREF,T_delta+T_delta*0.4
249 SOLVE
250
251 ! STEP 16
252 TIME,0.75
253 TREF,T_delta+T_delta*0.45
254 SOLVE
255
256 ! STEP 17
257 TIME,0.8
258 TREF,T_delta+T_delta*0.5
259 SOLVE
260
261 ! STEP 18
262 TIME,0.85
263 TREF,T_delta+T_delta*0.55
264 SOLVE
265
266 ! STEP 19
267 TIME,0.9
268 TREF,T_delta+T_delta*0.6
269 SOLVE
270
271 ! STEP 20
272 TIME,0.95
273 TREF,T_delta+T_delta*0.7
274 SOLVE
275
276 ! STEP 21
277 TIME,1
278 TREF,T_delta+T_delta*0.8
279 SOLVE
280
281 ! STEP 22
282 TIME,1.05
283 TREF,T_delta+T_delta*0.85
284 SOLVE
285
286 ! STEP 23
287 TIME,1.1
288 TREF,T_delta+T_delta*0.9
289 SOLVE
290
291 ! STEP 24
292 TIME,1.15
293 TREF,T_delta+T_delta*1
294 SOLVE
295
296 ! STEP 25
297 TIME,1.5
298 ARCLN,ON,1e-1,1e-5
299 FK,5,MY,LOAD_VALUE
300 SOLVE
301
302 /OUTPUT
303 FINISH
304

```

```

305 /POST26
306 NSOL,2,103,ROT,Y
307 RFORCE,4,2,M,Y
308 PROD,5,4,,,,,-1000
309 PRVAR,4
310 /AXLAB,X,ROTATION(rad)
311 /AXLAB,Y,TOTAL LOAD(Nm)
312 /GRID,1
313 /XRANGE,-1.4,1.4
314 /YRANGE,-5,5
315 XVAR,2
316 PLVAR,5
317 /NOERASE
318 /ERASE
319
320 FINISH

```

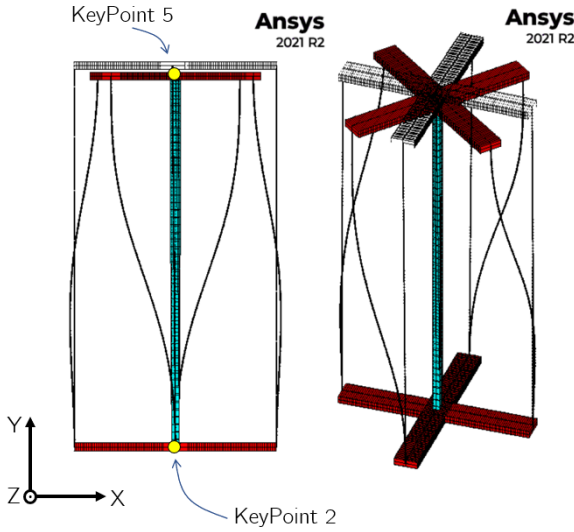
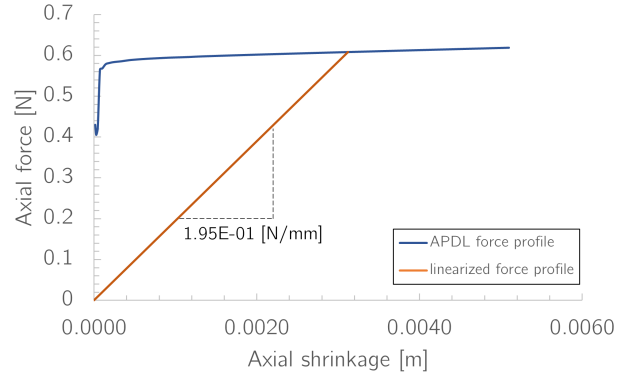


Figure 9: Model in ANSYS APDL, including the material properties that are used.

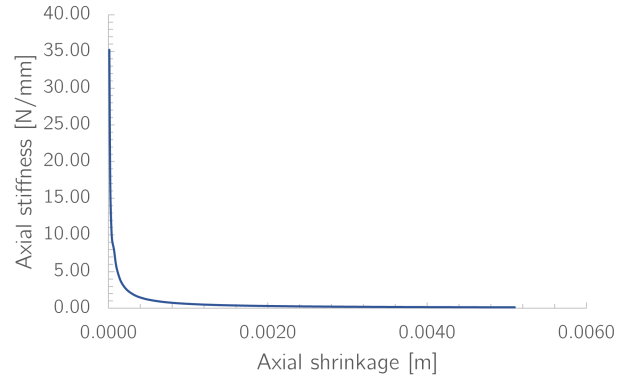
From this ANSYS model both the tangent stiffness as well as the secant stiffness as experienced by the PLA middle beam can be determined. Due to the rotational buckling behaviour of the wire flexures, the axial stiffness as experienced by the shrinking PLA is not linear. Both the tangent stiffness profile as well as the secant stiffness profile can be extracted from the force-displacement graph as shown in figure 10a. The tangent stiffness is shown figure 10b. A total axial shrinkage of 5 mm for a PLA beam of 100 mm (5% shrinkage) is simulated for. The secant stiffness is calculated by using equation 10. For determination of the secant stiffness a shrinkage value of 3 mm (3%) shrinkage is taken. This shrinkage value seems to be well attainable based on preliminary testing. In equation 10 s represents the axial shrinkage magnitude as shown on the horizontal axes of figures 10a and 10b.

$$K_{sec} = \frac{F_{s=0.003} - F_{s=0}}{0.003} \quad (10)$$

By using equation 10 a secant axial stiffness of 0.195 N/mm is obtained.



(a) APDL simulation of the axial force profile of the buckling wire flexures.



(b) APDL simulation of the axial stiffness profile of the buckling wire flexures.

Figure 10: Results from the APDL simulation regarding the axial stiffness and the axial force profile.

4. Building procedure

For assembly of the demonstrator, heat-resistant cyanoacrylate glue is used (MESA products, Almelo, The Netherlands). This glue has a curing time of 24 hours, implying that the to be glued parts should be constrained properly for this complete duration. Moreover, the wire flexures should be glued into the steel crosses as perpendicular as possible to prevent significantly lower buckling stiffness or unequal stability states when being bistable. Assembly of the demonstrator is split up in two parts. First all wire flexures are glued to the bottom cross and cured for 24 hours. To assure a straight connection between the wire flexure and the steel cross, special holders are 3D printed. These holders are shown in figure 11.

In the second assembly step the top cross is glued onto the system and cured for 24 hours. To again assure the straight connection between the wire flexure and the cross, and moreover to have a correct distance between both crosses, a tower-like geometry is 3D printed that is put between the crosses during the curing time of the glue. This geometry is shown in figure 12.

As final step a PLA beam needs to be 3D printed such that it can be inserted in the demonstrator. The



Figure 11: 3D printed holders (grey) are used during the manufacturing process to assure a straight and perpendicular glue connection between the steel cross and the wire flexure during glue curing.

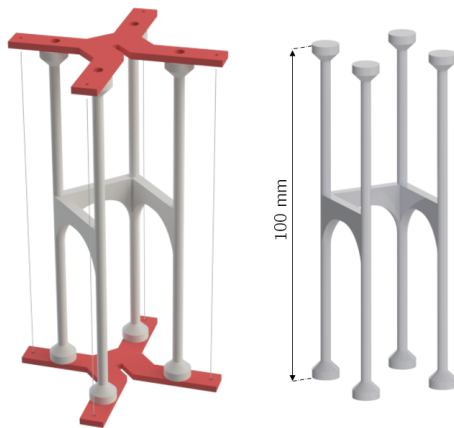


Figure 12: 3D printed tower-like geometries (grey), used to assure straight connections of the wire flexures during glue curing. These geometries are also used to set the correct distance between the two crosses.

design variables for this beam follow from the parameter study as performed in chapter 2.

5. Testing procedure

Testing of the demonstrator can roughly be split up in two separate parts; heating of the demonstrator and torsion testing. First the demonstrator is heated in the oven due to which the PLA will start shrinking. Consequently, the wire flexures will buckle when the applied compressive forces surpass the buckling force of the 4 wire flexures combined. As a result of this buckling the top cross will start to rotate with respect to the bottom cross around the centreline that is defined by the PLA beam. PLA loses its bending stiffness when heated above the T_g . To prevent potential sideways collapse of the demonstrator when heated, the demonstrator is put in a cylindrical glass with a

slightly larger inner diameter than the outer diameter of the crosses. In case of sideways motion this glass prevents tipping over of the demonstrator. When the predefined heating time has passed, the assembly is taken out of the oven and the shrinkage of the PLA is determined. Also the rotation angle between the top and bottom cross is recorded.

The second step of testing is torsion testing. The machine that is used for this is the ZwickRoell Z005 torsion machine (ZwickRoell GmbH & Co. KG, Ulm, Germany). Before insertion into this machine is possible, first M3 bolts-nut combinations need to be added to the demonstrator to provide a clamping interface for the machine. This is shown in figure 13.

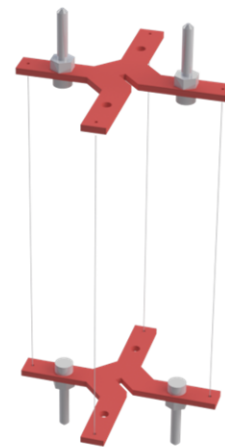


Figure 13: M3 bolt-nut combinations are inserted in the demonstrator to provide an interface with the torsion machine.

First, the bottom cross is connected to the torsion machine by aligning the axis of rotation of the torsion machine with the axis of rotation of the demonstrator. This aligning is done manually. When properly aligned, the clamping mechanism of the torsion machine is fastened. Hereafter the height of the top clamping mechanism is adjusted to be in line with the demonstrator's clamping interface. The clamping procedure as mentioned above is repeated for clamping the top. With both sides clamped, the torsion tests can be executed. The applied rotation angle is iteratively increased in order to not go beyond the allowed range of motion. Iterative increasing of this angle is done up to the point where a full bistable switch has been performed (i.e. up to the point where the torque reaches a value of 0 Nmm).

6. Possible further extension of the demonstrator

Initially the goal for the demonstrator was to have a fully printed geometry in which no use of steel parts or glue was required. This fully printed geometry, in which the desired monostable-to-bistable transition could be made, would then be created by

simultaneously printing with two different materials in a single FFF printer (i.e. using a dual nozzle FFF printer). When the two separate materials that are used have T_g s that lie sufficiently far apart from each other, heat-induced shrinkage can be enabled in one of the materials while the other material remains as is. A heating temperature T_{heating} should then be selected that adheres to the following: $T_{g,\text{mat1}} \leq T_{\text{heating}} \leq T_{g,\text{mat2}}$. Due to time and money constraints this fully printed demonstrator idea was only worked out on a conceptual level. The results of this conceptual design phase are presented in this section and they can be used as an onset for future work on this topic.

As a first step the two materials should be chosen correctly such that heat-induced shrinkage can take place only for the material with the lowest T_g . Multiple thermal factors need to be considered that might negatively influence the general shrinkage behaviour of the demonstrator. These thermal factors are the T_g , the melting temperature (T_m), the required print nozzle temperature (T_n) and the heated bed temperature (T_b). T will here be used to indicate the variable ambient temperature that can be set to enable material shrinkage. As shrinkage is enabled when $T > T_g$, a material combination in which e.g. $T_{g,\text{mat1}} < T_{b,\text{mat2}}$ will result in problems. Here shrinkage of material 1 will be enabled already during the printing process by the required heated bed temperature of material 2. The relations between the different thermal requirements of the two materials that are used are shown in matrix form in table 1. When a thermal factor of material 1 has no influence on another thermal factor of material 2, this is indicated with $-$ in the matrix.

Table 1: Matrix representation of requirements on the thermal factors between the shrinking material (mat1) and non-shrinking material (mat2). The symbolic relations should be read by putting mat1 on the left side of the operator and mat2 on the right side, e.g. $T_{x,\text{mat1}} >$ (or $<$) $T_{y,\text{mat2}}$.

	$T_{g,\text{mat2}}$	$T_{m,\text{mat2}}$	$T_{n,\text{mat2}}$	$T_{b,\text{mat2}}$
$T_{g,\text{mat1}}$	$<$	$<$	$>$	$>$
$T_{m,\text{mat1}}$	$>$	$-$	$>$	$>$
$T_{n,\text{mat1}}$	$<$	$<$	$-$	$-$
$T_{b,\text{mat1}}$	$<$	$<$	$-$	$-$

A list of the most common FFF filament materials is shown in table 2. In the first column the material name is provided. In the second column an indication is given on whether the material qualifies as amorphous (A) or semi-crystalline (SC). Semi-crystalline materials have a rather strictly defined T_g and T_m . The existence of the T_g in SC materials can be directly attributed to the amorphous portion of the material; fully crystalline material does not show a glassy-to-rubbery transition, this is a property that only is found for amorphous materials. On the contrary, the T_m in SC materials is directly caused by the

crystalline portion of the material. Fully crystalline material does show a clear glassy-to-(rubbery)liquid transition at T_m , which cannot be found in fully amorphous material. SC materials thus have a T_g and a T_m , whereas fully amorphous materials only have a T_g . For amorphous materials the rubbery-to-(rubbery)liquid transition is very gradual. Here the viscosity of the polymeric material increasingly reduces for an increasing temperature [5, 6]. In table 2 T_m values are still provided for the fully amorphous materials. These values are thus not actual melting points, but they rather represent temperatures that lie sufficiently far into the rubbery range by which the material can be considered to be a low viscosity polymer [7].

Table 2: Most common FFF printing materials with their T_g [8] and T_m [7]

Material	SC/A	T_g	T_m
PEEK	SC	143°C	357°C
PEI	A	215°C	340°C
PA12	SC	40°C	180°C
PA11	SC	40°C	187°C
PA6	SC	60°C	223°C
TPU	SC	60°C	146°C
PETG	A	80°C	264°C
PC	A	150°C	265°C
PPE	A	105°C	320°C
PP	SC	-15°C	179°C
PE	SC	-110°C	141°C
PLA	SC	60°C	180°C
ABS	A	96°C	200°C
PS	A	90°C	242°C
HIPS	A	90°C	242°C
PVC	A	80°C	220°C

In the study as presented in chapter 2, the focus is on PLA as the shrinking material. As knowledge is hereby gained on the behaviour of PLA, this material will be kept as the shrinking material in the current investigation as well. Material 1 as mentioned in table 1 is therefore PLA. By setting PLA as the shrinking material, the material requirements on material 2 that follow from table 1 are also directly known. Solely based on the T_g and T_m requirements as shown in table 1 this leaves PEEK, PC, PPE, ABS, PS, HIPS and PVC as feasible options. The difference between $T_{g,\text{mat1}}$ and $T_{g,\text{mat2}}$ should be sufficiently large such that only the material with the lowest T_g will be activated during heat introduction whilst the other material remains unaffected. In order to assure this, the following additional criterion is introduced: $T_{g,\text{mat2}} \geq T_{g,\text{PLA}} + 50^\circ\text{C}$. With this additional criterion only PEEK and PC remain as feasible materials.

PEEK requires a printing nozzle temperature between 370°C - 450 °C and a heated bed temperature between 120°C - 150 °C [9]. PC needs a nozzle temperature between 260°C - 310°C and a heated bed temperature between 80°C-120°C [10]. PLA has a

printing nozzle temperature between 190°C - 220°C and a heated bed temperature between 55°C - 70°C [11]. This results in table 3 for the combination of PLA and PEEK and in table 4 for the combination of PLA and PC.

Table 3: Matrix representation of requirements on the thermal factors between the shrinking material (PLA) and non-shrinking material (PEEK). When the operator is coloured green the criterion is met, when the operator is coloured red the criterion is not met.

	$T_{g,\text{PEEK}}$	$T_{m,\text{PEEK}}$	$T_{n,\text{PEEK}}$	$T_{b,\text{PEEK}}$
$T_{g,\text{PLA}}$	<	<	>	>
$T_{m,\text{PLA}}$	>	—	>	>
$T_{n,\text{PLA}}$	<	<	—	—
$T_{b,\text{PLA}}$	<	<	—	—

Table 4: Matrix representation of requirements on the thermal factors between the shrinking material (PLA) and non-shrinking material (PC). When the operator is coloured green the criterion is met, when the operator is coloured red the criterion is not met.

	$T_{g,\text{PC}}$	$T_{m,\text{PC}}$	$T_{n,\text{PC}}$	$T_{b,\text{PC}}$
$T_{g,\text{PLA}}$	<	<	> ⁽¹⁾	> ⁽²⁾
$T_{m,\text{PLA}}$	>	—	> ⁽³⁾	>
$T_{n,\text{PLA}}$	<	<	—	—
$T_{b,\text{PLA}}$	<	<	—	—

In table 3 four criteria are indicated in red. As $T_{g,\text{PEEK}}$, $T_{m,\text{PEEK}}$, $T_{n,\text{PEEK}}$ and $T_{b,\text{PEEK}}$ are all significantly higher than the corresponding values for PLA, this might impose significant heat-induced shrinkage problems already during the printing process. In table 4 three criteria are marked in red. These criteria are numbered from 1 to 3. Remarks on these points, as well as an interpretation of the severity of these failed requirements are discussed below.

1. $T_{g,\text{PLA}} < T_{n,\text{PC}}$ indicates that during printing the temperature of the nozzle for PC might enable the shape memory effect in the deposited PLA layers, resulting in shrinkage and warping during printing. $T_{g,\text{PLA}}$ has a value of 60°C whereas $T_{n,\text{PC}}$ has a lower bound value of around 260°C . Even though this difference of 200°C seems significant, the $T_{n,\text{PC}}$ is not directly imposed on the deposited materials. This is underlined by the fact that the upper bound of $T_{n,\text{PLA}}$ itself has a value of 220°C . Extruded filament material quickly cools down when it leaves the hot end of the FFF printer. Although it should still be tested for, the additional 40°C for $T_{n,\text{PC}}$ with respect to $T_{n,\text{PLA}}$ is deemed to be not problematic.
2. $T_{g,\text{PLA}} < T_{b,\text{PC}}$ indicates that during printing, the heated bed temperature of PC (lower bound of 80°C) is higher than the T_g of PLA (60°C). When adhering to these values, the heated bed temperature required for PC will enable the shape memory effect in the PLA layers

that have already been printed. The heated bed temperature mainly has the purpose of achieving proper layer-to-bed adhesion for the first few print layers [12]. Leaving the recommended T_b range could pose problems on adhesion for the first few layers of PC. The printing process itself is however not negatively affected. By keeping the bed temperature at the T_b value for PLA (55°C) there might not be any problems. Here additional testing should be performed to assess whether PC adheres to the print bed at lower print bed temperatures.

3. $T_{m,\text{PLA}} < T_{n,\text{PC}}$ indicates that the melting temperature of PLA (180°C) is lower than the nozzle temperature of PC (260°C). This could mean that during printing the PLA starts melting when PC layers are printed close to the already deposited PLA layers. Here the same argumentation as for remark 1 as mentioned above can be given. The nozzle temperature itself is not directly transferred to the deposited material, but rather it is used to heat up the to be printed material within the nozzle. From the moment of heating up to the moment of deposition, already significant cooling has taken place. As it is expected that $T_{n,\text{PC}}$ does not influence $T_{g,\text{PLA}}$ (remark 1), the same can be expected for $T_{m,\text{PLA}}$. As with the previous two remarks also here additional testing is required to confirm this suspicion.

A printing combination of PLA with PC would likely be the best option for a dual material and fully printed demonstrator. Given the requirements of both PLA and PC, a dual-material FFF printer like the Raise3D Pro 2 [13] can be used for this.

References

- [1] C. Chen, J. Chueh, H. Tseng, H. Huang, and S. Lee. Preparation and characterization of biodegradable polymeric blends. *Biomaterials*, 24(7):1167–1173, 2003.
- [2] U.C. Jindal. *Strength of Materials*. Person India, 2012.
- [3] R.G. Budynas and J.K. Nisbett. *Shigley's Mechanical Engineering Design*. McGraw-Hill, 2006.
- [4] H. Ahmad, G. Radaelli, and J. Herder. *Design and fabrication of a compliant joint with activatable pre-stress to switch between a stiff and a neutrally stable state*. Master's thesis, Delft University of Technology, 2022.
- [5] A. Bouzouita. *Elaboration of polylactide-based materials for automotive application : study of structure-process-properties interactions*. PhD dissertation, Université de Valenciennes et du Hainaut-Cambresis ; Université de Mons, 2016.
- [6] M.D. Lechner, K. Gehrke, and E.H. Nordmeier. *Makromolekulare Chemie*. Birkhäuser, 2010.
- [7] Melting points of polymers. <http://polymerdatabase.com/polymer%20physics/Polymer%20Tm%20C.html>. Accessed: 04-05-2022.
- [8] Omnexus. Glass transition temperature. <https://omnexus.specialchem.com/polymer-properties/properties/glass-transition-temperature>. Accessed: 04-05-2022.

-
- [9] 3D4makers.com. Best practices in 3d printing peek fdm filament. <https://www.3d4makers.com/blogs/news/best-practices-in-3d-printing-peek-fdm-filament>. Accessed: 20-06-2022.
- [10] Simplify3d.com. Polycarbonate. <https://www.simplify3d.com/support/materials-guide/polycarbonate/>. Accessed: 04-09-2022.
- [11] Ethan Sommer. The best pla bed & print temperature settings. <https://all3dp.com/2/the-best-pla-print-temperature-how-to-achieve-it/>. Accessed: 04-09-2022.
- [12] Roman Polák, František Sedláček, and Karel Raz. *Determination of FDM Printer Settings with Regard to Geometrical Accuracy*, pages 0561–0566. 01 2017.
- [13] Raise3D. Pro2 3d printer. <https://www.raise3d.com/products/pro2-3d-printer/>. Accessed: 04-09-2022.

Appendix D: G-code layer stacking in Matlab

1. Requirement of the stacking script

FFF printers sequentially execute commands that are provided by a g-code file. G-code can be created from CAD models by using a slicer program. Many slicers are available, with some of the more widely known programs being PrusaSlicer, Ultimaker Cura and Slic3r. All of the aforementioned programs are freeware and open source. For the study as presented in chapter 2, some requirements were needed for the generation of g-code that could not, or only in limited form, be provided by the slicing software. For this study as many non-investigated variables as possible should be excluded. Some variations that slicers add to their generated g-code by default are, amongst others:

- A different layer thickness for the first deposited layer than for all subsequent layers.
- A different nozzle temperature for the first deposited layer than for all subsequent layers.
- A different printing speed for the first deposited layer than for all subsequent layers.
- A fan cooling speed that depends on the layer height and the type of filling (e.g. first layer, perimeter, solid layer).
- A slightly displaced deposition pattern for each subsequent layer.

Generally these settings are applied layer-wide, meaning that values only change when changing to the next slice of the model (i.e. changes in variables are only dependent on the Z-direction). Although exceptions to this exist, for now it is assumed that this holds for all slicing variables. Additionally, the `parallel rectilinear` printing pattern appeared to not always work properly.

To assure that the influence of variations in the above mentioned parameters is kept as small as possible, a MATLAB code has been created that is able to extract a single print layer (i.e. one single slice) from a g-code file and duplicate this layer for a set amount of times in the Z-direction (i.e. the height direction within the printing volume). The current state of this code is only applicable to models that show no dimensional variations in the Z-direction.

2. Usage of the code

For using this stacking code, first a g-code file of a single slice must be available. In the here provided example a block of dimensions 40x10x1 (L [mm] x W [mm] x H [mm]) will be prepared for printing. This block is shown in figure 1. The CAD model of this

block is made in SolidWorks (v2019) and slicing is done in PrusaSlicer (v2.4.2).

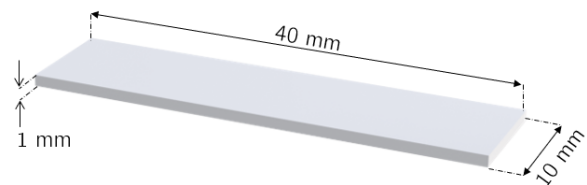


Figure 1: CAD model of the block.

As a first step a duplicate of the CAD model is made. The height of the model in this duplicate file must be reduced to exactly match the height of the first extruded layer as defined in the slicing software. For PrusaSlicer the default value for the thickness of the first layer is 0.2 mm. This results in the CAD model that is shown in figure 2. This model must be exported to a file that can be imported in the slicing software. For this example a .STL file is chosen for.

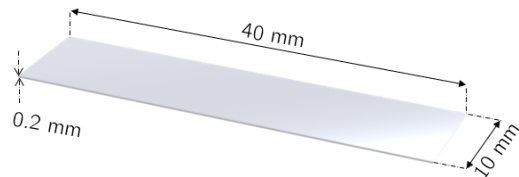


Figure 2: CAD model of the block with reduced height.

The next step is to import the .STL file in the slicing software. In the slicer brims, rafts and skirts should be disabled. Moreover, a correct printing speed should be set. N.B. this printing speed will be the printing speed that is applied to the complete model. When these settings are adjusted properly the model can be sliced. This should now result in the file as shown in figure 3. It is important to assure that only 1 layer is sliced by the Slicer. If this is not the case, most likely the layer height of the first layer in the slicer software should be adjusted.

The sliced model can now be exported to a g-code file via the export function in the slicer software. The name that is assigned to the g-code that is here created is `block.gcode`. This code can be found in section 4.

As a next step markers need to be manually added to the g-code such that the MATLAB script is able to recognize all commands that make up this single slice. The begin marker is defined as “`; begin layer 1`” in the MATLAB script. Another marker tag can be used, but it should accordingly be changed in the MATLAB code (line 13 - see section 3). The begin marker should be placed between

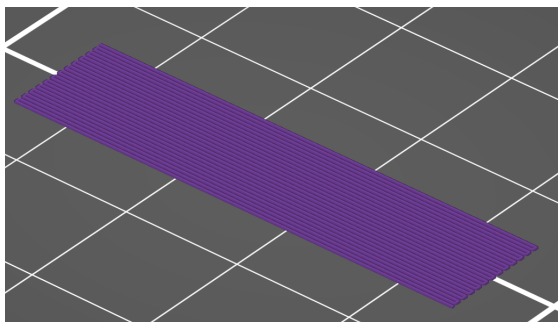


Figure 3: Sliced representation of the block with reduced height.

lines ;0.2 and ; printing object block.STL id:0 copy 0, which are lines 56 and 57 in the code in section 4 respectively. The end marker is defined as “; end layer 1”. Again this marker tag can be changed if desired. The end marker should be placed after all commands that make up the first slice, but before the place where the end sequence of the printer is entered. The marker should therefore be placed between M107 and ; TYPE:Custom, which are lines 155 and 156 respectively in the code in section 4.

When the markers are added to the g-code file, the file can be saved under the same name, i.e. block.gcode in this case. The layer_stacking.m file (see section 3) can be opened in MATLAB. Some parameters in the m-file can be adjusted by the user. In line 5 the number of layer multiplications can be entered. For the current example this value is set to 4 multiplications, resulting in a total of 5 layers. In line 6 the layer height for the first layer as defined in the slicer software is entered; 0.2 mm for the current case. This results in 5 layers with each a height of 0.2 mm. The total height of 1 mm will hereby again be obtained. In line 7 the name of the g-code file is entered, being block for this example. N.B. the extension .gcode must not be added here. As a final step the correct directory of the g-code file should be entered in line 58. The MATLAB script can now be executed and block_4layers_0.2mm_incr.gcode (see section 5) is the result. This code can now be directly used on a FFF printer to print a PLA block of dimensions 40x10x1 mm³ while assuring that print settings are consistent over all printed layers.

3. The layer_stacking.m MATLAB code

```

1  %% Gcode layer stacking code
2  clear all; close all; clc;
3  %% Parameters
4
5  no_layers = 4;
6  z_incr = 0.2;
7  doc_name = "block";
8  ext = ".gcode";
9  full_name = append(doc_name, ext);
10 gcode = fileread(full_name);
11
12 A = regexp(fileread(full_name), '\n', 'split');
```

```

13 start_line = find(contains(A, ' begin layer 1'
14 );
15 end_line = find(contains(A, ' end layer 1'));
16 steps = end_line-start_line+1;
17
18 %% insert G1 Z.2 F720 after start_line
19 ins = cellstr(append("G1 Z", num2str(z_incr), "
20 F720"));
21 A_beg = A(1:start_line);
22 A_end = A(start_line+1:end);
23 A = [A_beg; ins; A_end];
24 end_line = end_line+1;
25
26 for i = 1:no_layers
27     newlayer(:, :) = A(start_line:end_line);
28     newlayer(1) = cellstr(sprintf("; begin
29         layer %f", i+1));
30     newlayer(end) = cellstr(sprintf("; end
31         layer %f", i+1));
32     height_change = find(contains(newlayer, ' Z'
33         ));
34
35     for j = 1:length(height_change)
36         temp_line = newlayer(height_change(j));
37         idx = strfind(temp_line, "Z");
38         idx2 = strfind(temp_line, " ");
39         first_part = extractBefore(temp_line, "Z
40             ");
41         Z_val = extractBetween(temp_line, "Z", "
42             ");
43         Z_val2 = cellstr(append("Z", num2str(
44             str2num(char(Z_val))+z_incr*i));
45         last_part = extractAfter(temp_line,
46             Z_val);
47         new_line = append(char(first_part),
48             Z_val2, char(last_part));
49         newlayer(height_change(j)) = new_line;
50     end
51
52     newlayer_stored(:, i) = newlayer;
53 end
54
55 A_first = A(1:end_line);
56 A_last = A(end_line+1:end);
57 A_new = A_first;
58
59 for k = 1:no_layers
60     A_new = [A_new; newlayer_stored(:, k)];
61 end
62 A_new = [A_new; A_last];
63
64 writecell(A_new, append(doc_name, "_", num2str(
65     no_layers), "layers_", num2str(z_incr), "
66     mm_incr.txt"), "QuoteStrings", 0);
67
68 %% Change to G-code
69
70 directory = 'C:\...';
71 file = fullfile(directory, append(doc_name, "_",
72     num2str(no_layers), "layers_", num2str(z_incr),
73     "mm_incr.txt"));
74 [tempDir, tempFile] = fileparts(file);
75 status = copyfile(file, fullfile(tempDir,
76     append(tempFile, '.gcode')));
77
78 name_file = append(doc_name, "_", num2str(
79     no_layers), "layers_", num2str(z_incr), "
80     mm_incr.txt");
81 delete(name_file)
```

4. The g-code from PrusaSlicer - Block.gcode

```

1 ; generated by PrusaSlicer 2.4.2+win64 on
  2022-09-05 at 12:52:59 UTC
2
3 ;
4
5 ; external perimeters extrusion width = 0.45mm
6 ; perimeters extrusion width = 0.45mm
7 ; infill extrusion width = 0.45mm
8 ; solid infill extrusion width = 0.45mm
9 ; top infill extrusion width = 0.45mm
10 ; first layer extrusion width = 0.42mm
11
12 M73 P0 R0
13 M201 X9000 Y9000 Z500 E10000 ; sets maximum
  accelerations, mm/sec^2
14 M203 X500 Y500 Z12 E120 ; sets maximum
  feedrates, mm / sec
15 M204 P2000 R1500 T2000 ; sets acceleration (P,
  T) and retract acceleration (R), mm/sec^2
16 M205 X10.00 Y10.00 Z0.20 E4.50 ; sets the jerk
  limits, mm/sec
17 M205 S0 T0 ; sets the minimum extruding and
  travel feed rate, mm/sec
18 M107
19 ;TYPE:Custom
20 M862.3 P "MK2.5" ; printer model check
21 M862.1 P0.4 ; nozzle diameter check
22 M115 U3.11.0 ; tell printer latest fw version
23 G90 ; use absolute coordinates
24 M83 ; extruder relative mode
25 M104 S215 ; set extruder temp
26 M140 S60 ; set bed temp
27 M190 S60 ; wait for bed temp
28 M109 S215 ; wait for extruder temp
29 G28 W ; home all without mesh bed level
30 G80 ; mesh bed leveling
31 G1 Z0.2 F720
32 G1 Y-3 F1000 ; go outside print area
33 G92 E0
34 G1 X60 E9 F1000 ; intro line
35 G1 X100 E12.5 F1000 ; intro line
36 G92 E0
37 G21 ; set units to millimeters
38 G90 ; use absolute coordinates
39 M83 ; use relative distances for extrusion
40 M900 K0.05 ; Filament gcode LA 1.5
41 M900 K30 ; Filament gcode LA 1.0
42 M107
43 ;LAYER_CHANGE
44 ;Z:0.2
45 ;HEIGHT:0.2
46 ;BEFORE_LAYER_CHANGE
47 G92 E0.0
48 ;0.2
49
50
51 M73 P11 R0
52 G1 E-.8 F2100
53 M73 P19 R0
54 G1 Z.4 F720
55 ;AFTER_LAYER_CHANGE
56 ;0.2
57 ; printing object block.STL id:0 copy 0
58 G1 X105.219 Y109.608 F10800
59 G1 Z.2 F720
60 M73 P21 R0
61 G1 E.8 F2100
62 M204 S800
63 ;TYPE:Solid infill
64 ;WIDTH:0.42692
65 G1 F3600
66 G1 X144.611 Y109.608 E1.2578
67 G1 X144.611 Y109.224 E.01226
68 M73 P23 R0
69 G1 X105.389 Y109.224 E1.25238
70 M73 P24 R0
71 G1 X105.389 Y108.84 E.01226
72 M73 P26 R0
73 G1 X144.611 Y108.84 E1.25238
74 G1 X144.611 Y108.456 E.01226
75 M73 P28 R0
76 G1 X105.389 Y108.456 E1.25238
77 G1 X105.389 Y108.072 E.01226
78 M73 P30 R0
79 G1 X144.611 Y108.072 E1.25238
80 G1 X144.611 Y107.688 E.01226
81 M73 P32 R0
82 G1 X105.389 Y107.688 E1.25238
83 M73 P33 R0
84 G1 X105.389 Y107.304 E.01226
85 M73 P35 R0
86 G1 X144.611 Y107.304 E1.25238
87 G1 X144.611 Y106.92 E.01226
88 M73 P37 R0
89 G1 X105.389 Y106.92 E1.25238
90 G1 X105.389 Y106.536 E.01226
91 M73 P39 R0
92 G1 X144.611 Y106.536 E1.25238
93 G1 X144.611 Y106.152 E.01226
94 M73 P41 R0
95 G1 X105.389 Y106.152 E1.25238
96 M73 P42 R0
97 G1 X105.389 Y105.768 E.01226
98 M73 P44 R0
99 G1 X144.611 Y105.768 E1.25238
100 G1 X144.611 Y105.384 E.01226
101 M73 P46 R0
102 G1 X105.389 Y105.384 E1.25238
103 G1 X105.389 Y105 E.01226
104 M73 P48 R0
105 G1 X144.611 Y105 E1.25238
106 G1 X144.611 Y104.616 E.01226
107 M73 P50 R0
108 G1 X105.389 Y104.616 E1.25238
109 M73 P51 R0
110 G1 X105.389 Y104.232 E.01226
111 M73 P53 R0
112 G1 X144.611 Y104.232 E1.25238
113 G1 X144.611 Y103.848 E.01226
114 M73 P55 R0
115 G1 X105.389 Y103.848 E1.25238
116 G1 X105.389 Y103.464 E.01226
117 M73 P57 R0
118 G1 X144.611 Y103.464 E1.25238
119 G1 X144.611 Y103.08 E.01226
120 M73 P59 R0
121 G1 X105.389 Y103.08 E1.25238
122 M73 P60 R0
123 G1 X105.389 Y102.696 E.01226
124 M73 P62 R0
125 G1 X144.611 Y102.696 E1.25238
126 G1 X144.611 Y102.312 E.01226
127 M73 P64 R0
128 G1 X105.389 Y102.312 E1.25238
129 G1 X105.389 Y101.928 E.01226
130 M73 P66 R0
131 G1 X144.611 Y101.928 E1.25238
132 G1 X144.611 Y101.544 E.01226
133 M73 P68 R0
134 G1 X105.389 Y101.544 E1.25238
135 M73 P69 R0
136 G1 X105.389 Y101.16 E.01226
137 M73 P71 R0
138 G1 X144.611 Y101.16 E1.25238
139 G1 X144.611 Y100.776 E.01226
140 M73 P73 R0
141 G1 X105.389 Y100.776 E1.25238
142 G1 X105.389 Y100.392 E.01226
143 M73 P75 R0
144 G1 X144.781 Y100.392 E1.2578
145 M204 S1000
146 ; stop printing object block.STL id:0 copy 0
147 ;WIPE_START
148 G1 F8640;_WIPE
149 M73 P77 R0
150 G1 X141.49 Y100.392 E-.76
151 ;WIPE_END
152 G1 E-.04 F2100
153 M73 P78 R0
154 G1 Z.6 F720
155 M107
156 ;TYPE:Custom
157 ; Filament-specific end gcode
158 G1 Z1.2 F720 ; Move print head up
159 G1 X0 Y200 F3600 ; park
160 G1 Z49.2 F720 ; Move print head further up
161 G4 ; wait
162 M104 S0 ; turn off temperature
163 M140 S0 ; turn off heated
164 M107 ; turn off fan

```

```

165 M900 K0 ; reset LA
166 M84 ; disable motors
167 M73 P100 R0
168 ; filament used [mm] = 31.61
169 ; filament used [cm3] = 0.08
170 ; filament used [g] = 0.09
171 ; filament cost = 0.00
172 ; total filament used [g] = 0.09
173 ; total filament cost = 0.00
174 ; estimated printing time (normal mode) = 32s
175
176 ; prusaslicer_config = begin
177 ; avoid_crossing_perimeters = 0
178 ; avoid_crossing_perimeters_max_detour = 0
179 ; bed_custom_model =
180 ; bed_custom_texture =
181 ; bed_shape = 0x0,250x0,250x210,0x210
182 ; bed_temperature = 60
183 ; before_layer_gcode = ;BEFORE_LAYER_CHANGE\
    nG92 E0.0\n\n[layer_z]\n\n
184 ; between_objects_gcode =
185 ; bottom_fill_pattern = alignedrectilinear
186 ; bottom_solid_layers = 5
187 ; bottom_solid_min_thickness = 0.5
188 ; bridge_acceleration = 1000
189 ; bridge_angle = 0
190 ; bridge_fan_speed = 100
191 ; bridge_flow_ratio = 1
192 ; bridge_speed = 60
193 ; brim_separation = 0.1
194 ; brim_type = no_brim
195 ; brim_width = 0
196 ; clip_multipart_objects = 1
197 ; color_change_gcode = M600\nG1 E0.4 F1500 ;
    prime after color change
198 ; compatible_printers_condition_cumulative = "
    printer_notes=~/.*PRINTER_VENDOR_PRUSA3D.*/
    and printer_notes=~/.*PRINTER_MODEL_MK2
    [^].*/ and nozzle_diameter[0]=0.4";"
    nozzle_diameter[0]!=0.8 and !(
    printer_notes=~/.*PRINTER_VENDOR_PRUSA3D.*/
    and printer_notes=~/.*PRINTER_MODEL_MK
    (2.5|3).*/ and
    single_extruder_multi_material)"
199 ; complete_objects = 0
200 ; cooling = 1
201 ; cooling_tube_length = 5
202 ; cooling_tube_retraction = 91.5
203 ; default_acceleration = 1000
204 ; default_filament_profile = "Prusament PLA"
205 ; default_print_profile = 0.15mm OPTIMAL
206 ; deretract_speed = 0
207 ; disable_fan_first_layers = 1
208 ; dont_support_bridges = 0
209 ; draft_shield = disabled
210 ; duplicate_distance = 6
211 ; elephant_foot_compensation = 0.2
212 ; end_filament_gcode = "; Filament-specific end
    gcode"
213 ; end_gcode = {if max_layer_z <
    max_print_height}G1 Z{z_offset+min(
    max_layer_z+1, max_print_height)} F720 ;
    Move print head up{endif}\nG1 X0 Y200 F3600
    ; park\n{if max_layer_z < max_print_height
    }G1 Z{z_offset+min(max_layer_z+49,
    max_print_height)} F720 ; Move print head
    further up{endif}\nG4 ; wait\nM104 S0 ;
    turn off temperature\nM140 S0 ; turn off
    heatbed\nM107 ; turn off fan\nM900 K0 ;
    reset LA\nM84 ; disable motors
214 ; ensure_vertical_shell_thickness = 1
215 ; external_perimeter_extrusion_width = 0.45
216 ; external_perimeter_speed = 60
217 ; external_perimeters_first = 0
218 ; extra_loading_move = -2
219 ; extra_perimeters = 0
220 ; extruder_clearance_height = 20
221 ; extruder_clearance_radius = 45
222 ; extruder_colour = ""
223 ; extruder_offset = 0x0
224 ; extrusion_axis = E
225 ; extrusion_multiplier = 1
226 ; extrusion_width = 0.45
227 ; fan_always_on = 1
228 ; fan_below_layer_time = 100
229 ; filament_colour = #FF8000
230 ; filament_cooling_final_speed = 3.4
231 ; filament_cooling_initial_speed = 2.2
232 ; filament_cooling_moves = 4
233 ; filament_cost = 27.82
234 ; filament_density = 1.24
235 ; filament_diameter = 1.75
236 ; filament_load_time = 0
237 ; filament_loading_speed = 28
238 ; filament_loading_speed_start = 3
239 ; filament_max_volumetric_speed = 15
240 ; filament_minimal_purge_on_wipe_tower = 15
241 ; filament_notes = ""
242 ; filament_ramming_parameters = "120 100 6.6
    6.8 7.2 7.6 7.9 8.2 8.7 9.4 9.9 10.0| 0.05
    6.6 0.45 6.8 0.95 7.8 1.45 8.3 1.95 9.7
    2.45 10 2.95 7.6 3.45 7.6 3.95 7.6 4.45 7.6
    4.95 7.6"
243 ; filament_settings_id = "Prusa PLA"
244 ; filament_soluble = 0
245 ; filament_spool_weight = 230
246 ; filament_toolchange_delay = 0
247 ; filament_type = PLA
248 ; filament_unload_time = 0
249 ; filament_unloading_speed = 90
250 ; filament_unloading_speed_start = 100
251 ; filament_vendor = Made for Prusa
252 ; fill_angle = 0
253 ; fill_density = 100%
254 ; fill_pattern = alignedrectilinear
255 ; first_layer_acceleration = 800
256 ; first_layer_acceleration_overRAFT = 0
257 ; first_layer_bed_temperature = 60
258 ; first_layer_extrusion_width = 0.42
259 ; first_layer_height = 0.2
260 ; first_layer_speed = 60
261 ; first_layer_speed_overRAFT = 30
262 ; first_layer_temperature = 215
263 ; full_fan_speed_layer = 4
264 ; fuzzy_skin = none
265 ; fuzzy_skin_point_dist = 0.8
266 ; fuzzy_skin_thickness = 0.3
267 ; gap_fill_enabled = 1
268 ; gap_fill_speed = 60
269 ; gcode_comments = 0
270 ; gcode_flavor = marlin
271 ; gcode_label_objects = 1
272 ; gcode_resolution = 0.0125
273 ; gcode_substitutions =
274 ; high_current_on_filament_swap = 0
275 ; host_type = octoprint
276 ; infill_acceleration = 2000
277 ; infill_anchor = 2.5
278 ; infill_anchor_max = 12
279 ; infill_every_layers = 1
280 ; infill_extruder = 1
281 ; infill_extrusion_width = 0.45
282 ; infill_first = 0
283 ; infill_only_where_needed = 0
284 ; infill_overlap = 0%
285 ; infill_speed = 60
286 ; inherits_cumulative = "0.15mm OPTIMAL";;
287 ; interface_shells = 0
288 ; ironing = 0
289 ; ironing_flowrate = 15%
290 ; ironing_spacing = 0.1
291 ; ironing_speed = 15
292 ; ironing_type = top
293 ; layer_gcode = ;AFTER_LAYER_CHANGE\n\n[layer_z]
294 ; layer_height = 0.2
295 ; machine_limits_usage = emit_to_gcode
296 ; machine_max_acceleration_e = 10000
297 ; machine_max_acceleration_extruding = 2000
298 ; machine_max_acceleration_retracting = 1500
299 ; machine_max_acceleration_travel = 1500,1250
300 ; machine_max_acceleration_x = 9000
301 ; machine_max_acceleration_y = 9000
302 ; machine_max_acceleration_z = 500
303 ; machine_max_feedrate_e = 120
304 ; machine_max_feedrate_x = 500
305 ; machine_max_feedrate_y = 500
306 ; machine_max_feedrate_z = 12
307 ; machine_max_jerk_e = 4.5
308 ; machine_max_jerk_x = 10
309 ; machine_max_jerk_y = 10
310 ; machine_max_jerk_z = 0.2
311 ; machine_min_extruding_rate = 0
312 ; machine_min_travel_rate = 0
313 ; max_fan_speed = 100

```

```

314 ; max_layer_height = 0.25
315 ; max_print_height = 200
316 ; max_print_speed = 100
317 ; max_volumetric_speed = 0
318 ; min_fan_speed = 100
319 ; min_layer_height = 0.07
320 ; min_print_speed = 15
321 ; min_skirt_length = 4
322 ; mmu_segmented_region_max_width = 0
323 ; notes =
324 ; nozzle_diameter = 0.4
325 ; only_retract_when_crossing_perimeters = 0
326 ; ooze_prevention = 0
327 ; output_filename_format = {input_filename_base
    }_{layer_height}mm_{filament_type[0]}_{
    printer_model}_{print_time}.gcode
328 ; overhangs = 1
329 ; parking_pos_retraction = 92
330 ; pause_print_gcode = M601
331 ; perimeter_acceleration = 800
332 ; perimeter_extruder = 1
333 ; perimeter_extrusion_width = 0.45
334 ; perimeter_speed = 60
335 ; perimeters = 0
336 ; physical_printer_settings_id =
337 ; post_process =
338 ; print_settings_id = XRD
339 ; printer_model = MK2.5
340 ; printer_notes = Don't remove the following
    keywords! These keywords are used in the "
    compatible printer" condition of the print
    and filament profiles to link the
    particular print and filament profiles to
    this printer profile.\
    nPRINTER_VENDOR_PRUSA3D\nPRINTER_MODEL_MK2\
    n
341 ; printer_settings_id = Original Prusa i3 MK2.5
342 ; printer_technology = FFF
343 ; printer_variant = 0.4
344 ; printer_vendor =
345 ; raft_contact_distance = 0.2
346 ; raft_expansion = 1.5
347 ; raft_first_layer_density = 90%
348 ; raft_first_layer_expansion = 3
349 ; raft_layers = 0
350 ; remaining_times = 1
351 ; resolution = 0
352 ; retract_before_travel = 1
353 ; retract_before_wipe = 0%
354 ; retract_layer_change = 1
355 ; retract_length = 0.8
356 ; retract_length_toolchange = 4
357 ; retract_lift = 0.4
358 ; retract_lift_above = 0
359 ; retract_lift_below = 199
360 ; retract_restart_extra = 0
361 ; retract_restart_extra_toolchange = 0
362 ; retract_speed = 35
363 ; seam_position = nearest
364 ; silent_mode = 0
365 ; single_extruder_multi_material = 0
366 ; single_extruder_multi_material_priming = 1
367 ; skirt_distance = 2
368 ; skirt_height = 3
369 ; skirts = 0
370 ; slice_closing_radius = 0.049
371 ; slicing_mode = regular
372 ; slowdown_below_layer_time = 15
373 ; small_perimeter_speed = 60
374 ; solid_infill_below_area = 0
375 ; solid_infill_every_layers = 0
376 ; solid_infill_extruder = 1
377 ; solid_infill_extrusion_width = 0.45
378 ; solid_infill_speed = 60
379 ; spiral_vase = 0
380 ; standby_temperature_delta = -5
381 ; start_filament_gcode = "M900 K{if
    printer_notes=~/. *PRINTER_MODEL_MINI ./ and
    nozzle_diameter[0]==0.6}0.12{elseif
    printer_notes=~/. *PRINTER_MODEL_MINI ./ and
    nozzle_diameter[0]==0.8}0.06{elseif
    printer_notes=~/. *PRINTER_MODEL_MINI
    .*/}0.2{elseif nozzle_diameter[0]==0.8}0.01{
    elseif nozzle_diameter[0]==0.6}0.04{else
    }0.05{endif} ; Filament gcode LA 1.5\n{if
    printer_notes=~/. *PRINTER_MODEL_MINI ./};{
    elseif printer_notes=~/. *PRINTER_HAS_BOWDEN
    .*/}M900 K200{elseif nozzle_diameter
    [0]==0.6}M900 K18{elseif nozzle_diameter
    [0]==0.8};{else}M900 K30{endif} ; Filament
    gcode LA 1.0"
382 ; start_gcode = M862.3 P "[printer_model]" ;
    printer_model check\nM862.1 P[
    nozzle_diameter] ; nozzle diameter check\
    nM115 U3.11.0 ; tell printer latest fw
    version\nG90 ; use absolute coordinates\
    nM83 ; extruder relative mode\nM104 S[
    first_layer_temperature] ; set extruder
    temp\nM140 S[first_layer_bed_temperature] ;
    set bed temp\nM190 S[
    first_layer_bed_temperature] ; wait for bed
    temp\nM109 S[first_layer_temperature] ;
    wait for extruder temp\nG28 W ; home all
    without mesh bed level\nG80 ; mesh bed
    leveling\nG1 Z0.2 F720\nG1 Y-3 F1000 ; go
    outside print area\nG92 E0\nG1 X60 E9 F1000
    ; intro line\nG1 X100 E12.5 F1000 ; intro
    line\nG92 E0
383 ; support_material = 0
384 ; support_material_angle = 0
385 ; support_material_auto = 1
386 ; support_material_bottom_contact_distance = 0
387 ; support_material_bottom_interface_layers = 0
388 ; support_material_buildplate_only = 0
389 ; support_material_closing_radius = 2
390 ; support_material_contact_distance = 0.2
391 ; support_material_enforce_layers = 0
392 ; support_material_extruder = 0
393 ; support_material_extrusion_width = 0.35
394 ; support_material_interface_contact_loops = 0
395 ; support_material_interface_extruder = 0
396 ; support_material_interface_layers = 2
397 ; support_material_interface_pattern =
    rectilinear
398 ; support_material_interface_spacing = 0.2
399 ; support_material_interface_speed = 80%
400 ; support_material_pattern = rectilinear
401 ; support_material_spacing = 2
402 ; support_material_speed = 60
403 ; support_material_style = grid
404 ; support_material_synchronize_layers = 0
405 ; support_material_threshold = 50
406 ; support_material_with_sheath = 0
407 ; support_material_xy_spacing = 60%
408 ; temperature = 210
409 ; template_custom_gcode =
410 ; thick_bridges = 0
411 ; thin_walls = 0
412 ; threads = 12
413 ; thumbnails =
414 ; toolchange_gcode =
415 ; top_fill_pattern = alignedrectilinear
416 ; top_infill_extrusion_width = 0.45
417 ; top_solid_infill_speed = 60
418 ; top_solid_layers = 6
419 ; top_solid_min_thickness = 0.7
420 ; travel_speed = 180
421 ; travel_speed_z = 12
422 ; use_firmware_retraction = 0
423 ; use_relative_e_distances = 1
424 ; use_volumetric_e = 0
425 ; variable_layer_height = 1
426 ; wipe = 1
427 ; wipe_into_infill = 0
428 ; wipe_into_objects = 0
429 ; wipe_tower = 1
430 ; wipe_tower_bridging = 10
431 ; wipe_tower_brim_width = 2
432 ; wipe_tower_no_sparse_layers = 0
433 ; wipe_tower_rotation_angle = 0
434 ; wipe_tower_width = 60
435 ; wipe_tower_x = 170
436 ; wipe_tower_y = 140
437 ; wiping_volumes_extruders = 70,70
438 ; wiping_volumes_matrix = 0
439 ; xy_size_compensation = 0
440 ; z_offset = 0
441 ; prusaslicer_config = end

```

5. The resulting g-code
from layer_stacking.m
block_4layers_0.2mm_incr.gcode

```

1 ; generated by PrusaSlicer 2.4.2+win64 on
  2022-09-05 at 12:52:59 UTC
2
3 ;
4
5 ; external perimeters extrusion width = 0.45mm
6 ; perimeters extrusion width = 0.45mm
7 ; infill extrusion width = 0.45mm
8 ; solid infill extrusion width = 0.45mm
9 ; top infill extrusion width = 0.45mm
10 ; first layer extrusion width = 0.42mm
11
12 M73 P0 R0
13 M201 X9000 Y9000 Z500 E10000 ; sets maximum
  accelerations, mm/sec^2
14 M203 X500 Y500 Z12 E120 ; sets maximum
  feedrates, mm / sec
15 M204 P2000 R1500 T2000 ; sets acceleration (P,
  T) and retract acceleration (R), mm/sec^2
16 M205 X10.00 Y10.00 Z0.20 E4.50 ; sets the jerk
  limits, mm/sec
17 M205 S0 T0 ; sets the minimum extruding and
  travel feed rate, mm/sec
18 M107
19 ;TYPE:Custom
20 M862.3 P "MK2.5" ; printer model check
21 M862.1 P0.4 ; nozzle diameter check
22 M115 U3.11.0 ; tell printer latest fw version
23 G90 ; use absolute coordinates
24 M83 ; extruder relative mode
25 M104 S215 ; set extruder temp
26 M140 S60 ; set bed temp
27 M190 S60 ; wait for bed temp
28 M109 S215 ; wait for extruder temp
29 G28 W ; home all without mesh bed level
30 G80 ; mesh bed leveling
31 G1 Z0.2 F720
32 G1 Y-3 F1000 ; go outside print area
33 G92 E0
34 G1 X60 E9 F1000 ; intro line
35 G1 X100 E12.5 F1000 ; intro line
36 G92 E0
37 G21 ; set units to millimeters
38 G90 ; use absolute coordinates
39 M83 ; use relative distances for extrusion
40 M900 K0.05 ; Filament gcode LA 1.5
41 M900 K30 ; Filament gcode LA 1.0
42 M107
43 ;LAYER_CHANGE
44 ;Z:0.2
45 ;HEIGHT:0.2
46 ;BEFORE_LAYER_CHANGE
47 G92 E0.0
48 ;0.2
49
50
51 M73 P11 R0
52 G1 E-.8 F2100
53 M73 P19 R0
54 G1 Z.4 F720
55 ;AFTER_LAYER_CHANGE
56 ;0.2
57
58 ; begin layer 1
59 G1 Z0.2 F720
60
61 ; printing object block.STL id:0 copy 0
62 G1 X105.219 Y109.608 F10800
63 G1 Z.2 F720
64 M73 P21 R0
65 G1 E.8 F2100
66 M204 S800
67 ;TYPE:Solid infill
68 ;WIDTH:0.42692
69 G1 F3600
70 G1 X144.611 Y109.608 E1.2578
71 G1 X144.611 Y109.224 E.01226
72 M73 P23 R0
73 G1 X105.389 Y109.224 E1.25238
74 M73 P24 R0
75 G1 X105.389 Y108.84 E.01226
76 M73 P26 R0
77 G1 X144.611 Y108.84 E1.25238
78 G1 X144.611 Y108.456 E.01226
79 M73 P28 R0
80 G1 X105.389 Y108.456 E1.25238
81 G1 X105.389 Y108.072 E.01226
82 M73 P30 R0
83 G1 X144.611 Y108.072 E1.25238
84 G1 X144.611 Y107.688 E.01226
85 M73 P32 R0
86 G1 X105.389 Y107.688 E1.25238
87 M73 P33 R0
88 G1 X105.389 Y107.304 E.01226
89 M73 P35 R0
90 G1 X144.611 Y107.304 E1.25238
91 G1 X144.611 Y106.92 E.01226
92 M73 P37 R0
93 G1 X105.389 Y106.92 E1.25238
94 G1 X105.389 Y106.536 E.01226
95 M73 P39 R0
96 G1 X144.611 Y106.536 E1.25238
97 G1 X144.611 Y106.152 E.01226
98 M73 P41 R0
99 G1 X105.389 Y106.152 E1.25238
100 M73 P42 R0
101 G1 X105.389 Y105.768 E.01226
102 M73 P44 R0
103 G1 X144.611 Y105.768 E1.25238
104 G1 X144.611 Y105.384 E.01226
105 M73 P46 R0
106 G1 X105.389 Y105.384 E1.25238
107 G1 X105.389 Y105 E.01226
108 M73 P48 R0
109 G1 X144.611 Y105 E1.25238
110 G1 X144.611 Y104.616 E.01226
111 M73 P50 R0
112 G1 X105.389 Y104.616 E1.25238
113 M73 P51 R0
114 G1 X105.389 Y104.232 E.01226
115 M73 P53 R0
116 G1 X144.611 Y104.232 E1.25238
117 G1 X144.611 Y103.848 E.01226
118 M73 P55 R0
119 G1 X105.389 Y103.848 E1.25238
120 G1 X105.389 Y103.464 E.01226
121 M73 P57 R0
122 G1 X144.611 Y103.464 E1.25238
123 G1 X144.611 Y103.08 E.01226
124 M73 P59 R0
125 G1 X105.389 Y103.08 E1.25238
126 M73 P60 R0
127 G1 X105.389 Y102.696 E.01226
128 M73 P62 R0
129 G1 X144.611 Y102.696 E1.25238
130 G1 X144.611 Y102.312 E.01226
131 M73 P64 R0
132 G1 X105.389 Y102.312 E1.25238
133 G1 X105.389 Y101.928 E.01226
134 M73 P66 R0
135 G1 X144.611 Y101.928 E1.25238
136 G1 X144.611 Y101.544 E.01226
137 M73 P68 R0
138 G1 X105.389 Y101.544 E1.25238
139 M73 P69 R0
140 G1 X105.389 Y101.16 E.01226
141 M73 P71 R0
142 G1 X144.611 Y101.16 E1.25238
143 G1 X144.611 Y100.776 E.01226
144 M73 P73 R0
145 G1 X105.389 Y100.776 E1.25238
146 G1 X105.389 Y100.392 E.01226
147 M73 P75 R0
148 G1 X144.781 Y100.392 E1.2578
149 M204 S1000
150 ; stop printing object block.STL id:0 copy 0
151 ;WIPE_START
152 G1 F8640 ;_WIPE
153 M73 P77 R0
154 G1 X141.49 Y100.392 E-.76
155 ;WIPE_END
156 G1 E-.04 F2100
157 M73 P78 R0
158 G1 Z.6 F720
159 M107
160
161 ; end layer 1

```

```
162 ; begin layer 2.000000
163 G1 Z0.4 F720
164
165 ; printing object block.STL id:0 copy 0
166 G1 X105.219 Y109.608 F10800
167 G1 Z0.4 F720
168 M73 P21 R0
169 G1 E.8 F2100
170 M204 S800
171 ;TYPE:Solid infill
172 ;WIDTH:0.42692
173 G1 F3600
174 G1 X144.611 Y109.608 E1.2578
175 G1 X144.611 Y109.224 E.01226
176 M73 P23 R0
177 G1 X105.389 Y109.224 E1.25238
178 M73 P24 R0
179 G1 X105.389 Y108.84 E.01226
180 M73 P26 R0
181 G1 X144.611 Y108.84 E1.25238
182 G1 X144.611 Y108.456 E.01226
183 M73 P28 R0
184 G1 X105.389 Y108.456 E1.25238
185 G1 X105.389 Y108.072 E.01226
186 M73 P30 R0
187 G1 X144.611 Y108.072 E1.25238
188 G1 X144.611 Y107.688 E.01226
189 M73 P32 R0
190 G1 X105.389 Y107.688 E1.25238
191 M73 P33 R0
192 G1 X105.389 Y107.304 E.01226
193 M73 P35 R0
194 G1 X144.611 Y107.304 E1.25238
195 G1 X144.611 Y106.92 E.01226
196 M73 P37 R0
197 G1 X105.389 Y106.92 E1.25238
198 G1 X105.389 Y106.536 E.01226
199 M73 P39 R0
200 G1 X144.611 Y106.536 E1.25238
201 G1 X144.611 Y106.152 E.01226
202 M73 P41 R0
203 G1 X105.389 Y106.152 E1.25238
204 M73 P42 R0
205 G1 X105.389 Y105.768 E.01226
206 M73 P44 R0
207 G1 X144.611 Y105.768 E1.25238
208 G1 X144.611 Y105.384 E.01226
209 M73 P46 R0
210 G1 X105.389 Y105.384 E1.25238
211 G1 X105.389 Y105 E.01226
212 M73 P48 R0
213 G1 X144.611 Y105 E1.25238
214 G1 X144.611 Y104.616 E.01226
215 M73 P50 R0
216 G1 X105.389 Y104.616 E1.25238
217 M73 P51 R0
218 G1 X105.389 Y104.232 E.01226
219 M73 P53 R0
220 G1 X144.611 Y104.232 E1.25238
221 G1 X144.611 Y103.848 E.01226
222 M73 P55 R0
223 G1 X105.389 Y103.848 E1.25238
224 G1 X105.389 Y103.464 E.01226
225 M73 P57 R0
226 G1 X144.611 Y103.464 E1.25238
227 G1 X144.611 Y103.08 E.01226
228 M73 P59 R0
229 G1 X105.389 Y103.08 E1.25238
230 M73 P60 R0
231 G1 X105.389 Y102.696 E.01226
232 M73 P62 R0
233 G1 X144.611 Y102.696 E1.25238
234 G1 X144.611 Y102.312 E.01226
235 M73 P64 R0
236 G1 X105.389 Y102.312 E1.25238
237 G1 X105.389 Y101.928 E.01226
238 M73 P66 R0
239 G1 X144.611 Y101.928 E1.25238
240 G1 X144.611 Y101.544 E.01226
241 M73 P68 R0
242 G1 X105.389 Y101.544 E1.25238
243 M73 P69 R0
244 G1 X105.389 Y101.16 E.01226
245 M73 P71 R0
246 G1 X144.611 Y101.16 E1.25238
247 G1 X144.611 Y100.776 E.01226
248 M73 P73 R0
249 G1 X105.389 Y100.776 E1.25238
250 G1 X105.389 Y100.392 E.01226
251 M73 P75 R0
252 G1 X144.781 Y100.392 E1.2578
253 M204 S1000
254 ; stop printing object block.STL id:0 copy 0
255 ;WIPE_START
256 G1 F8640;_WIPE
257 M73 P77 R0
258 G1 X141.49 Y100.392 E-.76
259 ;WIPE_END
260 G1 E-.04 F2100
261 M73 P78 R0
262 G1 Z0.8 F720
263 M107
264
265 ; end layer 2.000000
266 ; begin layer 3.000000
267 G1 Z0.6 F720
268
269 ; printing object block.STL id:0 copy 0
270 G1 X105.219 Y109.608 F10800
271 G1 Z0.6 F720
272 M73 P21 R0
273 G1 E.8 F2100
274 M204 S800
275 ;TYPE:Solid infill
276 ;WIDTH:0.42692
277 G1 F3600
278 G1 X144.611 Y109.608 E1.2578
279 G1 X144.611 Y109.224 E.01226
280 M73 P23 R0
281 G1 X105.389 Y109.224 E1.25238
282 M73 P24 R0
283 G1 X105.389 Y108.84 E.01226
284 M73 P26 R0
285 G1 X144.611 Y108.84 E1.25238
286 G1 X144.611 Y108.456 E.01226
287 M73 P28 R0
288 G1 X105.389 Y108.456 E1.25238
289 G1 X105.389 Y108.072 E.01226
290 M73 P30 R0
291 G1 X144.611 Y108.072 E1.25238
292 G1 X144.611 Y107.688 E.01226
293 M73 P32 R0
294 G1 X105.389 Y107.688 E1.25238
295 M73 P33 R0
296 G1 X105.389 Y107.304 E.01226
297 M73 P35 R0
298 G1 X144.611 Y107.304 E1.25238
299 G1 X144.611 Y106.92 E.01226
300 M73 P37 R0
301 G1 X105.389 Y106.92 E1.25238
302 G1 X105.389 Y106.536 E.01226
303 M73 P39 R0
304 G1 X144.611 Y106.536 E1.25238
305 G1 X144.611 Y106.152 E.01226
306 M73 P41 R0
307 G1 X105.389 Y106.152 E1.25238
308 M73 P42 R0
309 G1 X105.389 Y105.768 E.01226
310 M73 P44 R0
311 G1 X144.611 Y105.768 E1.25238
312 G1 X144.611 Y105.384 E.01226
313 M73 P46 R0
314 G1 X105.389 Y105.384 E1.25238
315 G1 X105.389 Y105 E.01226
316 M73 P48 R0
317 G1 X144.611 Y105 E1.25238
318 G1 X144.611 Y104.616 E.01226
319 M73 P50 R0
320 G1 X105.389 Y104.616 E1.25238
321 M73 P51 R0
322 G1 X105.389 Y104.232 E.01226
323 M73 P53 R0
324 G1 X144.611 Y104.232 E1.25238
325 G1 X144.611 Y103.848 E.01226
326 M73 P55 R0
327 G1 X105.389 Y103.848 E1.25238
328 G1 X105.389 Y103.464 E.01226
329 M73 P57 R0
330 G1 X144.611 Y103.464 E1.25238
331 G1 X144.611 Y103.08 E.01226
332 M73 P59 R0
333 G1 X105.389 Y103.08 E1.25238
334 M73 P60 R0
335 G1 X105.389 Y102.696 E.01226
```

```
336 M73 P62 R0
337 G1 X144.611 Y102.696 E1.25238
338 G1 X144.611 Y102.312 E.01226
339 M73 P64 R0
340 G1 X105.389 Y102.312 E1.25238
341 G1 X105.389 Y101.928 E.01226
342 M73 P66 R0
343 G1 X144.611 Y101.928 E1.25238
344 G1 X144.611 Y101.544 E.01226
345 M73 P68 R0
346 G1 X105.389 Y101.544 E1.25238
347 M73 P69 R0
348 G1 X105.389 Y101.16 E.01226
349 M73 P71 R0
350 G1 X144.611 Y101.16 E1.25238
351 G1 X144.611 Y100.776 E.01226
352 M73 P73 R0
353 G1 X105.389 Y100.776 E1.25238
354 G1 X105.389 Y100.392 E.01226
355 M73 P75 R0
356 G1 X144.781 Y100.392 E1.2578
357 M204 S1000
358 ; stop printing object block.STL id:0 copy 0
359 ;WIPE_START
360 G1 F8640;_WIPE
361 M73 P77 R0
362 G1 X141.49 Y100.392 E-.76
363 ;WIPE_END
364 G1 E-.04 F2100
365 M73 P78 R0
366 G1 Z1 F720
367 M107
368
369 ; end layer 3.000000
370 ; begin layer 4.000000
371 G1 Z0.8 F720
372
373 ; printing object block.STL id:0 copy 0
374 G1 X105.219 Y109.608 F10800
375 G1 Z0.8 F720
376 M73 P21 R0
377 G1 E.8 F2100
378 M204 S800
379 ;TYPE:Solid infill
380 ;WIDTH:0.42692
381 G1 F3600
382 G1 X144.611 Y109.608 E1.2578
383 G1 X144.611 Y109.224 E.01226
384 M73 P23 R0
385 G1 X105.389 Y109.224 E1.25238
386 M73 P24 R0
387 G1 X105.389 Y108.84 E.01226
388 M73 P26 R0
389 G1 X144.611 Y108.84 E1.25238
390 G1 X144.611 Y108.456 E.01226
391 M73 P28 R0
392 G1 X105.389 Y108.456 E1.25238
393 G1 X105.389 Y108.072 E.01226
394 M73 P30 R0
395 G1 X144.611 Y108.072 E1.25238
396 G1 X144.611 Y107.688 E.01226
397 M73 P32 R0
398 G1 X105.389 Y107.688 E1.25238
399 M73 P33 R0
400 G1 X105.389 Y107.304 E.01226
401 M73 P35 R0
402 G1 X144.611 Y107.304 E1.25238
403 G1 X144.611 Y106.92 E.01226
404 M73 P37 R0
405 G1 X105.389 Y106.92 E1.25238
406 G1 X105.389 Y106.536 E.01226
407 M73 P39 R0
408 G1 X144.611 Y106.536 E1.25238
409 G1 X144.611 Y106.152 E.01226
410 M73 P41 R0
411 G1 X105.389 Y106.152 E1.25238
412 M73 P42 R0
413 G1 X105.389 Y105.768 E.01226
414 M73 P44 R0
415 G1 X144.611 Y105.768 E1.25238
416 G1 X144.611 Y105.384 E.01226
417 M73 P46 R0
418 G1 X105.389 Y105.384 E1.25238
419 G1 X105.389 Y105 E.01226
420 M73 P48 R0
421 G1 X144.611 Y105 E1.25238
422 G1 X144.611 Y104.616 E.01226
423 M73 P50 R0
424 G1 X105.389 Y104.616 E1.25238
425 M73 P51 R0
426 G1 X105.389 Y104.232 E.01226
427 M73 P53 R0
428 G1 X144.611 Y104.232 E1.25238
429 G1 X144.611 Y103.848 E.01226
430 M73 P55 R0
431 G1 X105.389 Y103.848 E1.25238
432 G1 X105.389 Y103.464 E.01226
433 M73 P57 R0
434 G1 X144.611 Y103.464 E1.25238
435 G1 X144.611 Y103.08 E.01226
436 M73 P59 R0
437 G1 X105.389 Y103.08 E1.25238
438 M73 P60 R0
439 G1 X105.389 Y102.696 E.01226
440 M73 P62 R0
441 G1 X144.611 Y102.696 E1.25238
442 G1 X144.611 Y102.312 E.01226
443 M73 P64 R0
444 G1 X105.389 Y102.312 E1.25238
445 G1 X105.389 Y101.928 E.01226
446 M73 P66 R0
447 G1 X144.611 Y101.928 E1.25238
448 G1 X144.611 Y101.544 E.01226
449 M73 P68 R0
450 G1 X105.389 Y101.544 E1.25238
451 M73 P69 R0
452 G1 X105.389 Y101.16 E.01226
453 M73 P71 R0
454 G1 X144.611 Y101.16 E1.25238
455 G1 X144.611 Y100.776 E.01226
456 M73 P73 R0
457 G1 X105.389 Y100.776 E1.25238
458 G1 X105.389 Y100.392 E.01226
459 M73 P75 R0
460 G1 X144.781 Y100.392 E1.2578
461 M204 S1000
462 ; stop printing object block.STL id:0 copy 0
463 ;WIPE_START
464 G1 F8640;_WIPE
465 M73 P77 R0
466 G1 X141.49 Y100.392 E-.76
467 ;WIPE_END
468 G1 E-.04 F2100
469 M73 P78 R0
470 G1 Z1.2 F720
471 M107
472
473 ; end layer 4.000000
474 ; begin layer 5.000000
475 G1 Z1 F720
476
477 ; printing object block.STL id:0 copy 0
478 G1 X105.219 Y109.608 F10800
479 G1 Z1 F720
480 M73 P21 R0
481 G1 E.8 F2100
482 M204 S800
483 ;TYPE:Solid infill
484 ;WIDTH:0.42692
485 G1 F3600
486 G1 X144.611 Y109.608 E1.2578
487 G1 X144.611 Y109.224 E.01226
488 M73 P23 R0
489 G1 X105.389 Y109.224 E1.25238
490 M73 P24 R0
491 G1 X105.389 Y108.84 E.01226
492 M73 P26 R0
493 G1 X144.611 Y108.84 E1.25238
494 G1 X144.611 Y108.456 E.01226
495 M73 P28 R0
496 G1 X105.389 Y108.456 E1.25238
497 G1 X105.389 Y108.072 E.01226
498 M73 P30 R0
499 G1 X144.611 Y108.072 E1.25238
500 G1 X144.611 Y107.688 E.01226
501 M73 P32 R0
502 G1 X105.389 Y107.688 E1.25238
503 M73 P33 R0
504 G1 X105.389 Y107.304 E.01226
505 M73 P35 R0
506 G1 X144.611 Y107.304 E1.25238
507 G1 X144.611 Y106.92 E.01226
508 M73 P37 R0
509 G1 X105.389 Y106.92 E1.25238
```

```

510 G1 X105.389 Y106.536 E.01226
511 M73 P39 R0
512 G1 X144.611 Y106.536 E1.25238
513 G1 X144.611 Y106.152 E.01226
514 M73 P41 R0
515 G1 X105.389 Y106.152 E1.25238
516 M73 P42 R0
517 G1 X105.389 Y105.768 E.01226
518 M73 P44 R0
519 G1 X144.611 Y105.768 E1.25238
520 G1 X144.611 Y105.384 E.01226
521 M73 P46 R0
522 G1 X105.389 Y105.384 E1.25238
523 G1 X105.389 Y105 E.01226
524 M73 P48 R0
525 G1 X144.611 Y105 E1.25238
526 G1 X144.611 Y104.616 E.01226
527 M73 P50 R0
528 G1 X105.389 Y104.616 E1.25238
529 M73 P51 R0
530 G1 X105.389 Y104.232 E.01226
531 M73 P53 R0
532 G1 X144.611 Y104.232 E1.25238
533 G1 X144.611 Y103.848 E.01226
534 M73 P55 R0
535 G1 X105.389 Y103.848 E1.25238
536 G1 X105.389 Y103.464 E.01226
537 M73 P57 R0
538 G1 X144.611 Y103.464 E1.25238
539 G1 X144.611 Y103.08 E.01226
540 M73 P59 R0
541 G1 X105.389 Y103.08 E1.25238
542 M73 P60 R0
543 G1 X105.389 Y102.696 E.01226
544 M73 P62 R0
545 G1 X144.611 Y102.696 E1.25238
546 G1 X144.611 Y102.312 E.01226
547 M73 P64 R0
548 G1 X105.389 Y102.312 E1.25238
549 G1 X105.389 Y101.928 E.01226
550 M73 P66 R0
551 G1 X144.611 Y101.928 E1.25238
552 G1 X144.611 Y101.544 E.01226
553 M73 P68 R0
554 G1 X105.389 Y101.544 E1.25238
555 M73 P69 R0
556 G1 X105.389 Y101.16 E.01226
557 M73 P71 R0
558 G1 X144.611 Y101.16 E1.25238
559 G1 X144.611 Y100.776 E.01226
560 M73 P73 R0
561 G1 X105.389 Y100.776 E1.25238
562 G1 X105.389 Y100.392 E.01226
563 M73 P75 R0
564 G1 X144.781 Y100.392 E1.2578
565 M204 S1000
566 ; stop printing object block.STL id:0 copy 0
567 ;WIPE_START
568 G1 F8640;_WIPE
569 M73 P77 R0
570 G1 X141.49 Y100.392 E-.76
571 ;WIPE_END
572 G1 E-.04 F2100
573 M73 P78 R0
574 G1 Z1.4 F720
575 M107
576
577 ; end layer 5.000000
578
579 ;TYPE:Custom
580 ; Filament-specific end gcode
581 G1 Z1.2 F720 ; Move print head up
582 G1 X0 Y200 F3600 ; park
583 G1 Z49.2 F720 ; Move print head further up
584 G4 ; wait
585 M104 S0 ; turn off temperature
586 M140 S0 ; turn off heatbed
587 M107 ; turn off fan
588 M900 K0 ; reset LA
589 M84 ; disable motors
590 M73 P100 R0
591 ; filament used [mm] = 31.61
592 ; filament used [cm3] = 0.08
593 ; filament used [g] = 0.09
594 ; filament cost = 0.00
595 ; total filament used [g] = 0.09
596 ; total filament cost = 0.00
597 ; estimated printing time (normal mode) = 32s
598
599 ; prusaslicer_config = begin
600 ; avoid_crossing_perimeters = 0
601 ; avoid_crossing_perimeters_max_detour = 0
602 ; bed_custom_model =
603 ; bed_custom_texture =
604 ; bed_shape = 0x0,250x0,250x210,0x210
605 ; bed_temperature = 60
606 ; before_layer_gcode = ;BEFORE_LAYER_CHANGE\
nG92 E0.0\n;[layer_z]\n\n
607 ; between_objects_gcode =
608 ; bottom_fill_pattern = alignedrectilinear
609 ; bottom_solid_layers = 5
610 ; bottom_solid_min_thickness = 0.5
611 ; bridge_acceleration = 1000
612 ; bridge_angle = 0
613 ; bridge_fan_speed = 100
614 ; bridge_flow_ratio = 1
615 ; bridge_speed = 60
616 ; brim_separation = 0.1
617 ; brim_type = no_brim
618 ; brim_width = 0
619 ; clip_multipart_objects = 1
620 ; color_change_gcode = M600\nG1 E0.4 F1500 ;
prime after color change
621 ; compatible_printers_condition_cumulative = "
printer_notes=~/.*PRINTER_VENDOR_PRUSA3D.*\
and printer_notes=~/.*PRINTER_MODEL_MK2
[^\].*/ and nozzle_diameter[0]=0.4";"
nozzle_diameter[0]!=0.8 and ! (
printer_notes=~/.*PRINTER_VENDOR_PRUSA3D.*\
and printer_notes=~/.*PRINTER_MODEL_MK
(2.5|3).*/ and
single_extruder_multi_material)"
622 ; complete_objects = 0
623 ; cooling = 1
624 ; cooling_tube_length = 5
625 ; cooling_tube_retraction = 91.5
626 ; default_acceleration = 1000
627 ; default_filament_profile = "Prusament PLA"
628 ; default_print_profile = 0.15mm OPTIMAL
629 ; deretract_speed = 0
630 ; disable_fan_first_layers = 1
631 ; dont_support_bridges = 0
632 ; draft_shield = disabled
633 ; duplicate_distance = 6
634 ; elephant_foot_compensation = 0.2
635 ; end_filament_gcode = "; Filament-specific end
gcode"
636 ; end_gcode = {if max_layer_z <
max_print_height}G1 Z{z_offset+min(
max_layer_z+1, max_print_height)} F720 ;
Move print head up{endif}\nG1 X0 Y200 F3600
; park\n{if max_layer_z < max_print_height
}G1 Z{z_offset+min(max_layer_z+49,
max_print_height)} F720 ; Move print head
further up{endif}\nG4 ; wait\nM104 S0 ;
turn off temperature\nM140 S0 ; turn off
heatbed\nM107 ; turn off fan\nM900 K0 ;
reset LA\nM84 ; disable motors
637 ; ensure_vertical_shell_thickness = 1
638 ; external_perimeter_extrusion_width = 0.45
639 ; external_perimeter_speed = 60
640 ; external_perimeters_first = 0
641 ; extra_loading_move = -2
642 ; extra_perimeters = 0
643 ; extruder_clearance_height = 20
644 ; extruder_clearance_radius = 45
645 ; extruder_colour = ""
646 ; extruder_offset = 0x0
647 ; extrusion_axis = E
648 ; extrusion_multiplier = 1
649 ; extrusion_width = 0.45
650 ; fan_always_on = 1
651 ; fan_below_layer_time = 100
652 ; filament_colour = #FF8000
653 ; filament_cooling_final_speed = 3.4
654 ; filament_cooling_initial_speed = 2.2
655 ; filament_cooling_moves = 4
656 ; filament_cost = 27.82
657 ; filament_density = 1.24
658 ; filament_diameter = 1.75
659 ; filament_load_time = 0
660 ; filament_loading_speed = 28
661 ; filament_loading_speed_start = 3
662 ; filament_max_volumetric_speed = 15

```

```

663 ; filament_minimal_purge_on_wipe_tower = 15
664 ; filament_notes = ""
665 ; filament_raming_parameters = "120 100 6.6
    6.8 7.2 7.6 7.9 8.2 8.7 9.4 9.9 10.0| 0.05
    6.6 0.45 6.8 0.95 7.8 1.45 8.3 1.95 9.7
    2.45 10 2.95 7.6 3.45 7.6 3.95 7.6 4.45 7.6
    4.95 7.6"
666 ; filament_settings_id = "Prusa PLA"
667 ; filament_soluble = 0
668 ; filament_spool_weight = 230
669 ; filament_toolchange_delay = 0
670 ; filament_type = PLA
671 ; filament_unload_time = 0
672 ; filament_unloading_speed = 90
673 ; filament_unloading_speed_start = 100
674 ; filament_vendor = Made for Prusa
675 ; fill_angle = 0
676 ; fill_density = 100%
677 ; fill_pattern = alignedrectilinear
678 ; first_layer_acceleration = 800
679 ; first_layer_acceleration_over_raft = 0
680 ; first_layer_bed_temperature = 60
681 ; first_layer_extrusion_width = 0.42
682 ; first_layer_height = 0.2
683 ; first_layer_speed = 60
684 ; first_layer_speed_over_raft = 30
685 ; first_layer_temperature = 215
686 ; full_fan_speed_layer = 4
687 ; fuzzy_skin = none
688 ; fuzzy_skin_point_dist = 0.8
689 ; fuzzy_skin_thickness = 0.3
690 ; gap_fill_enabled = 1
691 ; gap_fill_speed = 60
692 ; gcode_comments = 0
693 ; gcode_flavor = marlin
694 ; gcode_label_objects = 1
695 ; gcode_resolution = 0.0125
696 ; gcode_substitutions =
697 ; high_current_on_filament_swap = 0
698 ; host_type = octoprint
699 ; infill_acceleration = 2000
700 ; infill_anchor = 2.5
701 ; infill_anchor_max = 12
702 ; infill_every_layers = 1
703 ; infill_extruder = 1
704 ; infill_extrusion_width = 0.45
705 ; infill_first = 0
706 ; infill_only_where_needed = 0
707 ; infill_overlap = 0%
708 ; infill_speed = 60
709 ; inherits_cumulative = "0.15mm OPTIMAL";;
710 ; interface_shells = 0
711 ; ironing = 0
712 ; ironing_flowrate = 15%
713 ; ironing_spacing = 0.1
714 ; ironing_speed = 15
715 ; ironing_type = top
716 ; layer_gcode = ;AFTER_LAYER_CHANGE\n;[layer_z]
717 ; layer_height = 0.2
718 ; machine_limits_usage = emit_to_gcode
719 ; machine_max_acceleration_e = 10000
720 ; machine_max_acceleration_extruding = 2000
721 ; machine_max_acceleration_retracting = 1500
722 ; machine_max_acceleration_travel = 1500,1250
723 ; machine_max_acceleration_x = 9000
724 ; machine_max_acceleration_y = 9000
725 ; machine_max_acceleration_z = 500
726 ; machine_max_feedrate_e = 120
727 ; machine_max_feedrate_x = 500
728 ; machine_max_feedrate_y = 500
729 ; machine_max_feedrate_z = 12
730 ; machine_max_jerk_e = 4.5
731 ; machine_max_jerk_x = 10
732 ; machine_max_jerk_y = 10
733 ; machine_max_jerk_z = 0.2
734 ; machine_min_extruding_rate = 0
735 ; machine_min_travel_rate = 0
736 ; max_fan_speed = 100
737 ; max_layer_height = 0.25
738 ; max_print_height = 200
739 ; max_print_speed = 100
740 ; max_volumetric_speed = 0
741 ; min_fan_speed = 100
742 ; min_layer_height = 0.07
743 ; min_print_speed = 15
744 ; min_skirt_length = 4
745 ; mmu_segmented_region_max_width = 0
746 ; notes =
747 ; nozzle_diameter = 0.4
748 ; only_retract_when_crossing_perimeters = 0
749 ; ooze_prevention = 0
750 ; output_filename_format = {input_filename_base
    }_{layer_height}mm_{filament_type[0]}_{
    printer_model}_{print_time}.gcode
751 ; overhangs = 1
752 ; parking_pos_retraction = 92
753 ; pause_print_gcode = M601
754 ; perimeter_acceleration = 800
755 ; perimeter_extruder = 1
756 ; perimeter_extrusion_width = 0.45
757 ; perimeter_speed = 60
758 ; perimeters = 0
759 ; physical_printer_settings_id =
760 ; post_process =
761 ; print_settings_id = XRD
762 ; printer_model = MK2.5
763 ; printer_notes = Don't remove the following
    keywords! These keywords are used in the "
    compatible printer" condition of the print
    and filament profiles to link the
    particular print and filament profiles to
    this printer profile.\
    nPRINTER_VENDOR_PRUSA3D\nPRINTER_MODEL_MK2\
    n
764 ; printer_settings_id = Original Prusa i3 MK2.5
765 ; printer_technology = FFF
766 ; printer_variant = 0.4
767 ; printer_vendor =
768 ; raft_contact_distance = 0.2
769 ; raft_expansion = 1.5
770 ; raft_first_layer_density = 90%
771 ; raft_first_layer_expansion = 3
772 ; raft_layers = 0
773 ; remaining_times = 1
774 ; resolution = 0
775 ; retract_before_travel = 1
776 ; retract_before_wipe = 0%
777 ; retract_layer_change = 1
778 ; retract_length = 0.8
779 ; retract_length_toolchange = 4
780 ; retract_lift = 0.4
781 ; retract_lift_above = 0
782 ; retract_lift_below = 199
783 ; retract_restart_extra = 0
784 ; retract_restart_extra_toolchange = 0
785 ; retract_speed = 35
786 ; seam_position = nearest
787 ; silent_mode = 0
788 ; single_extruder_multi_material = 0
789 ; single_extruder_multi_material_priming = 1
790 ; skirt_distance = 2
791 ; skirt_height = 3
792 ; skirts = 0
793 ; slice_closing_radius = 0.049
794 ; slicing_mode = regular
795 ; slowdown_below_layer_time = 15
796 ; small_perimeter_speed = 60
797 ; solid_infill_below_area = 0
798 ; solid_infill_every_layers = 0
799 ; solid_infill_extruder = 1
800 ; solid_infill_extrusion_width = 0.45
801 ; solid_infill_speed = 60
802 ; spiral_vase = 0
803 ; standby_temperature_delta = -5
804 ; start_filament_gcode = "M900 K{if
    printer_notes="/.*PRINTER_MODEL_MINI.*/ and
    nozzle_diameter[0]==0.6}0.12{elsif
    printer_notes="/.*PRINTER_MODEL_MINI.*/ and
    nozzle_diameter[0]==0.8}0.06{elsif
    printer_notes="/.*PRINTER_MODEL_MINI
    .*/}0.2{elsif nozzle_diameter[0]==0.8}0.01{
    elsif nozzle_diameter[0]==0.6}0.04{else
    }0.05{endif}; Filament gcode LA 1.5\n{if
    printer_notes="/.*PRINTER_MODEL_MINI.*/};{
    elsif printer_notes="/.*PRINTER_HAS_BOWDEN
    .*/}M900 K200{elsif nozzle_diameter
    [0]==0.6}M900 K18{elsif nozzle_diameter
    [0]==0.8};{else}M900 K30{endif}; Filament
    gcode LA 1.0"
805 ; start_gcode = M862.3 P "[printer_model]" ;
    printer model check\nM862.1 P[
    nozzle_diameter]; nozzle diameter check\
    nM115 U3.11.0 ; tell printer latest fw
    version\nG90 ; use absolute coordinates\

```

```

nM83 ; extruder relative mode\nM104 S[
first_layer_temperature] ; set extruder
temp\nM140 S[first_layer_bed_temperature] ;
set bed temp\nM190 S[
first_layer_bed_temperature] ; wait for bed
temp\nM109 S[first_layer_temperature] ;
wait for extruder temp\nG28 W ; home all
without mesh bed level\nG80 ; mesh bed
leveling\nG1 Z0.2 F720\nG1 Y-3 F1000 ; go
outside print area\nG92 E0\nG1 X60 E9 F1000
; intro line\nG1 X100 E12.5 F1000 ; intro
line\nG92 E0
806 ; support_material = 0
807 ; support_material_angle = 0
808 ; support_material_auto = 1
809 ; support_material_bottom_contact_distance = 0
810 ; support_material_bottom_interface_layers = 0
811 ; support_material_buildplate_only = 0
812 ; support_material_closing_radius = 2
813 ; support_material_contact_distance = 0.2
814 ; support_material_enforce_layers = 0
815 ; support_material_extruder = 0
816 ; support_material_extrusion_width = 0.35
817 ; support_material_interface_contact_loops = 0
818 ; support_material_interface_extruder = 0
819 ; support_material_interface_layers = 2
820 ; support_material_interface_pattern =
    rectilinear
821 ; support_material_interface_spacing = 0.2
822 ; support_material_interface_speed = 80%
823 ; support_material_pattern = rectilinear
824 ; support_material_spacing = 2
825 ; support_material_speed = 60
826 ; support_material_style = grid
827 ; support_material_synchronize_layers = 0
828 ; support_material_threshold = 50
829 ; support_material_with_sheath = 0
830 ; support_material_xy_spacing = 60%
831 ; temperature = 210
832 ; template_custom_gcode =
833 ; thick_bridges = 0
834 ; thin_walls = 0
835 ; threads = 12
836 ; thumbnails =
837 ; toolchange_gcode =
838 ; top_fill_pattern = alignedrectilinear
839 ; top_infill_extrusion_width = 0.45
840 ; top_solid_infill_speed = 60
841 ; top_solid_layers = 6
842 ; top_solid_min_thickness = 0.7
843 ; travel_speed = 180
844 ; travel_speed_z = 12
845 ; use_firmware_retraction = 0
846 ; use_relative_e_distances = 1
847 ; use_volumetric_e = 0
848 ; variable_layer_height = 1
849 ; wipe = 1
850 ; wipe_into_infill = 0
851 ; wipe_into_objects = 0
852 ; wipe_tower = 1
853 ; wipe_tower_bridging = 10
854 ; wipe_tower_brim_width = 2
855 ; wipe_tower_no_sparse_layers = 0
856 ; wipe_tower_rotation_angle = 0
857 ; wipe_tower_width = 60
858 ; wipe_tower_x = 170
859 ; wipe_tower_y = 140
860 ; wiping_volumes_extruders = 70,70
861 ; wiping_volumes_matrix = 0
862 ; xy_size_compensation = 0
863 ; z_offset = 0
864 ; prusaslicer_config = end

```

Appendix E: Preliminary study on heat-induced material shrinkage

In the starting phase of the research no specific knowledge on heat-induced shrinkage was available other than that as provided by a sparse amount of literature [1–7]. In order to get familiarized with the topic, and to investigate the influence of different printing and heating parameters on the shrinkage behaviour of printed material, a preliminary test study is performed. The goal of this study is to establish the fundamental knowledge on heat-induced material shrinkage upon which the final research can be based. The method and results of this study are presented in this appendix.

1. Method

In this preliminary study most test samples are printed on an Ender 3 Pro 3D printer (Shenzhen Creality 3D Technology Co, Ltd., Shenzhen, China). Some samples have been printed on a Prusa i3 mk2.5 (Prusa Research, Prague, Czech Republic). For each test result an explicit indication of the printer that is used is provided.

A default sample geometry is used for testing. In this way results of different tests can properly be compared to each other. This sample geometry, together with the assigned dimensions, is shown in figure 1. Two ridges are present on the top side of the sample. These ridges are added such that the samples can be clamped in an aluminium frame. This clamping will be useful for some of the performed tests.

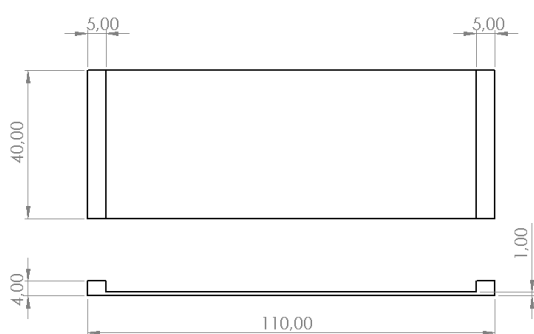


Figure 1: The default sample that is used.

All samples are printed with an FFF printer and subsequently heated in an oven (Silvercrest 9-in-1 Air-fryer). Dimensions of the samples are measured both prior to heating and after heating in order to establish the heat-induced shrinkage strain magnitudes. Measurements are done with a calliper. Each sample has its unique sample name (ID) written at the top left corner on the side where the ridges are present. This

marking functions as a reference point to which all measurement points are defined. The sample ID can also be seen in figure 2. With respect to this ID marking, 8 measurement points are defined and numbered. These measurement points are indicated by blue dots in figure 2. These dots are located on both opposing free edges of the sample and they are located 33.3 mm apart from each other. The dots are manually added to the sample with a permanent marker. Measurement point 1 is defined to be at the corner where the sample name is located. The numbering convention with respect to measurement point 1 is shown in figure 2.

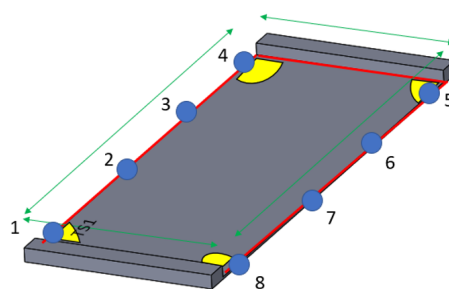


Figure 2: Representation of a sample geometry and measuring the measuring points.

A complete overview of the preliminary tests is shown in table 1. In this overview two sections can be distinguished. In the first section all samples are indicated with sample IDs that either start with TS, HB or FS. Samples with these names all are based on the geometry as presented in figure 2. In the second section all sample IDs start with BP. For these samples comparative tests are performed on varying print speeds. The geometry that is used for these samples can be found in figure 3. Shrinkage strain values are recorded for each of the 6 fingers separately.

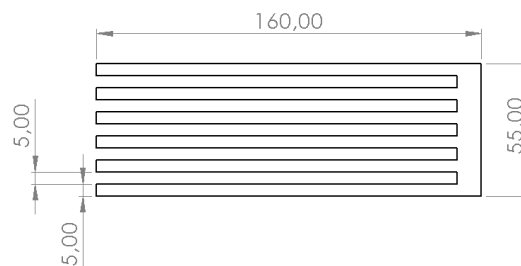


Figure 3: The beam plate sample that is used.

ID	Material	Print speed	Speed profile	Print pattern	Notes	Annealing time	Annealing temp	Printer
TS1	PLA	60	Uniform	Rectilinear (crossed)	Check to see if printer works	45 min	110	Prusa
TS2	PLA	100	Uniform	Rectilinear (crossed)	High speed printing	45 min	110	Prusa
TS3	PLA	20	Uniform	Rectilinear (crossed)	Low speed printing	45 min	110	Prusa
TS4	PLA	60	Uniform	Rectilinear (crossed)	Medium speed shrinkage test, with frame	45 min	110	Prusa
TS5	PLA	100	Uniform	Rectilinear (crossed)	High speed shrinkage test, with frame	45 min	110	Prusa
TS6	PLA	20	Uniform	Rectilinear (crossed)	Slow speed shrinkage test, with frame	45 min	110	Prusa
TS1.5	PLA	60	Uniform	Rectilinear (crossed)	Medium speed shrinkage test	45 min	110	Prusa
TS7	PLA	-	Varying	Rectilinear	Variable speed shrinkage test, fan off	45 min	110	Prusa
TS8	PLA	-	Varying	Rectilinear	Variable speed shrinkage test, fan on	45 min	110	Prusa
TS9	PLA	-	Varying	Rectilinear	Variable speed shrinkage test, fan on, with frame	45 min	110	Prusa
TS10	PLA	5	Uniform	Rectilinear	Extreme low speed shrinkage test	45 min	110	Prusa
TS11	PLA	10	Uniform	Rectilinear	Extreme low speed shrinkage test	45 min	110	Prusa
TS12	PLA	15	Uniform	Rectilinear	Extreme low speed shrinkage test	45 min	110	Prusa
TS13	PLA	20	Uniform	Rectilinear	Extreme low speed shrinkage test	45 min	110	Prusa
TS14	PLA	-	Varying	Rectilinear	Variable speed shrinkage test, fan on, more layers w.r.t. TS8	45 min	110	Prusa
TS42	PLA	60	Uniform	Rectilinear (crossed)	Medium speed shrinkage test, with improved frame	45 min	110	Prusa
TS52	PLA	100	Uniform	Rectilinear (crossed)	High speed shrinkage test, with improved frame	45 min	110	Prusa
TS62	PLA	20	Uniform	Rectilinear (crossed)	Slow speed shrinkage test, with improved frame	45 min	110	Prusa
TS15	PLA	60	Uniform	Rectilinear (crossed)	Short annealing time	5 min	110	Prusa
TS152	PLA	60	Uniform	Rectilinear (crossed)	Short annealing time	5 min	110	Ender
TS16	PLA	60	Uniform	Rectilinear (crossed)	Mid-short annealing time	15 min	110	Prusa
TS162	PLA	60	Uniform	Rectilinear (crossed)	Mid-short annealing time	15 min	110	Ender
TS17	PLA	60	Uniform	Rectilinear (crossed)	Mid annealing time	30 min	110	Prusa
TS172	PLA	60	Uniform	Rectilinear (crossed)	Mid annealing time	30 min	110	Ender
TS18	PLA	60	Uniform	Rectilinear (crossed)	Mid-long annealing time	60 min	110	Prusa
TS182	PLA	60	Uniform	Rectilinear (crossed)	Mid-long annealing time	60 min	110	Ender
TS19	PLA	60	Uniform	Rectilinear (crossed)	Long annealing time	90 min	110	Prusa
TS192	PLA	60	Uniform	Rectilinear (crossed)	Long annealing time	90 min	110	Ender
TS20	PLA	60	Uniform	Rectilinear (crossed)	Sub Tg annealing temp	45 min	40	Ender
TS21	PLA	60	Uniform	Rectilinear (crossed)	Tg annealing temp	45 min	65	Ender
TS22	PLA	60	Uniform	Rectilinear (crossed)	Tg annealing temp	45 min	80	Ender
TS23	PLA	60	Uniform	Rectilinear (crossed)	Low > Tg annealing temp [faulty -> wrong oven settings]	45 min	95 - 110	Ender
TS24	PLA	60	Uniform	Rectilinear (crossed)	High > Tg annealing temp [faulty -> wrong oven settings]	45 min	125 - 110	Ender
TS232	PLA	60	Uniform	Rectilinear (crossed)	Low > Tg annealing temp	45 min	95	Ender
TS242	PLA	60	Uniform	Rectilinear (crossed)	High > Tg annealing temp	45 min	125	Ender
TS27	PLA	60	Uniform	Rectilinear (crossed)	High > Tg annealing temp	45 min	110	Ender
TS28	PLA	60	Uniform	Rectilinear (crossed)	Medium annealing temp, long annealing time	90 min	65	Ender

ID	Material	Print speed	Speed profile	Print pattern	Notes	Annealing time	Annealing temp	Printer
TS25	PLA	60	Uniform	Rectilinear (crossed)	Extremely high > Tg annealing temp	45 min	140	Ender
HB1	PLA	60	Uniform	Rectilinear (crossed)	Heated bed annealing [off]	45 min	110	Ender
HB2	PLA	60	Uniform	Rectilinear (crossed)	Heated bed annealing [on]	45 min	110	Ender
TS1.52	PETG	60	Uniform	Rectilinear (crossed)	PETG annealing test (Tg + 60)	45 min	140	Prusa
TS2.5	PETG	100	Uniform	Rectilinear (crossed)	PETG annealing test (Tg + 60), 90 deg change in filament orientation	45 min	140	Prusa
TS3.5	PETG	20	Uniform	Rectilinear (crossed)	PETG annealing test (Tg + 60)	45 min	140	Prusa
FS1	PLA	60	Uniform	Rectilinear	Fan speed 0%	45 min	110	Ender
FS2	PLA	60	Uniform	Rectilinear	Fan speed 20%	45 min	110	Ender
FS3	PLA	60	Uniform	Rectilinear	Fan speed 40%	45 min	110	Ender
FS4	PLA	60	Uniform	Rectilinear	Fan speed 60%	45 min	110	Ender
FS5	PLA	60	Uniform	Rectilinear	Fan speed 80%	45 min	110	Ender
FS6	PLA	60	Uniform	Rectilinear	Fan speed 100%	45 min	110	Ender
TS26	PLA	60	Uniform	Rectilinear (crossed)	Layer stacking influence	45 min	110	Ender
TS263	PLA	60	Uniform	Rectilinear (crossed)	Layer stacking influence, lengthwise directional strip on top	45 min	110	Ender
TS262	PLA	60	Uniform	Rectilinear (crossed)	Layer stacking influence, test 2 (new printer)	45 min	110	Ender
Layer_test	PLA	60	Uniform	Rectilinear	Test stacking code, check if axial:transverse strain is different	45 min	110	Ender
BP1	PLA	Varying	Varying	Rectilinear	Single side fixed differential shrinkage test - 1 layer	45 min	110	Ender
BP2	PLA	Varying	Varying	Rectilinear	Single side fixed differential shrinkage test - 2 layer	45 min	110	Ender
BP3	PLA	Varying	Varying	Rectilinear	Single side fixed differential shrinkage test - 5 layer	45 min	110	Ender
BP4	PLA	Varying	Varying	Rectilinear	Double side fixed differential shrinkage test - 1 layer	45 min	110	Ender
BP5	PLA	Varying	Varying	Rectilinear	Double side fixed differential shrinkage test - 2 layer	45 min	110	Ender
BP6	PLA	Varying	Varying	Rectilinear	Double side fixed differential shrinkage test - 5 layer	45 min	110	Ender
BP7	PLA	Varying	Varying	Rectilinear	Triple beams differential shrinkage test - 1 layer	45 min	110	Ender
BP8	PLA	Varying	Varying	Rectilinear	Triple beams differential shrinkage test - 2 layer	45 min	110	Ender
BP9	PLA	Varying	Varying	Rectilinear	Triple beams differential shrinkage test - 5 layer	45 min	110	Ender
BP3.5	PLA	Varying	Varying	Rectilinear	Single side fixed differential shrinkage test - 5 layer - 1 [mm/s] to 5 [mm/s] change w.r.t BP3	45 min	110	Ender
BP6.5	PLA	Varying	Varying	Rectilinear	Double side fixed differential shrinkage test - 5 layer - 1 [mm/s] to 5 [mm/s] change w.r.t BP6	45 min	110	Ender
BP4.5	PLA	Varying	Varying	Rectilinear	Double side fixed differential shrinkage test - 1 layer - with constraining frame	45 min	110	Ender
BP5.5	PLA	Varying	Varying	Rectilinear	Double side fixed differential shrinkage test - 2 layer - with constraining frame	45 min	110	Ender
BP6.52	PLA	Varying	Varying	Rectilinear	Double side fixed differential shrinkage test - 5 layer - with constraining frame	45 min	110	Ender
BP10	PLA	Varying	Varying	Rectilinear	Varying nozzle speed vs extrusion speed - ratio 1	45 min	110	Ender
BP11	PLA	Varying	Varying	Rectilinear	Varying nozzle speed vs extrusion speed - ratio 0.95	45 min	110	Ender
BP12	PLA	Varying	Varying	Rectilinear	Varying nozzle speed vs extrusion speed - ratio 0.90	45 min	110	Ender
BP13	PLA	Varying	Varying	Rectilinear	Varying nozzle speed vs extrusion speed - ratio 1.05	45 min	110	Ender
BP14	PLA	Varying	Varying	Rectilinear	Varying nozzle speed vs extrusion speed - ratio 1.10	45 min	110	Ender

ID	Material	Print speed	Speed profile	Print pattern	Notes	Annealing time	Annealing temp	Printer
BP15	PLA		Varying	Rectilinear	Spring steel sample (same as BP9)	45 min	110	Ender
BP152	PLA		Varying	Rectilinear	Spring steel sample (same as BP9)	45 min	110	Ender
BP16	PLA		Varying	Rectilinear	Spring steel sample (same as BP9)	45 min	110	Ender

Printed & annealed
Printed
Is being printed
Is being annealed
Did not work/failed/not needed anymore
Gcode ready

Table 1: Overview of the performed preliminary tests.

2. Results

Results of the preliminary tests are shown in table 2. Result entries that are coloured grey are either faulty, not measured or not applicable for that particular test. For all test sample IDs that start with the prefix BP strains L1 to L6 are recorded. Each of these strains correspond to the strain of one of the fingers in figure 3. In the first section of the results the recorded shrinkage strain between measurement points 1-4, 4-5, 5-8 and 8-1 can be found. When taking the average of the shrinkage between measurement points 1-4 and 5-8, this results in the column **Average shrinkage axial**. The average shrinkage strain between points 4-5 and 8-1 results in **Average shrinkage transverse** N.B. the term strain is here used as a measure for the resulting shrinkage. Positive strain is here defined as shrinkage, negative strain thus indicates lengthening.

3. Differences between Prusa and Creality printers

During the preliminary tests two different FFF printers are used; the Creality Ender 3 Pro and the Prusa i3 mk2.5. During analysis of the preliminary results it was observed that even though the same g-code and oven settings are used, significantly different shrinkage magnitudes were resulting. This is illustrated in figure 4 where the axial material shrinkage as a function of heating time is shown for PLA strips. Here the exact same g-code is used on both printers and no alterations are made to the oven settings.

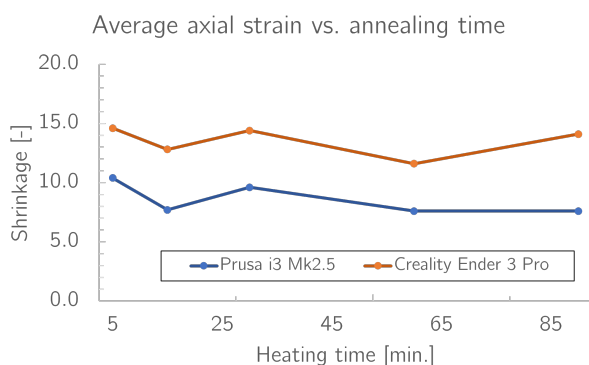


Figure 4: Differences in shrinkage magnitude of test samples printed with the Prusa i3 mk2.5 and the Creality Ender Pro 3.

In figure 4 it can be observed that there is a clear difference between the shrinkage magnitudes of the samples that are printed on the Prusa i3 mk2.5 and the Creality Ender 3 Pro. For all measurement points the heat-induced shrinkage magnitude seems to be consistently higher for the Creality printer than for the Prusa printer. The shrinkage difference is approximately 5% for all setpoint of this measurement set.

When looking at differences between the two printers some remarks can be made.

- The Prusa printer has a direct drive filament feeding system whereas the Creality printer has a bowden-tube filament feed.
- The Prusa printer uses an automatic bed-levelling procedure. For the Creality printer bed levelling must be done manually.
- The Creality printer was bought new whereas the Prusa printer has been used extensively. This might have resulted in wear of components. Especially when the brass nozzle wears down this might have influence on the rheology of the nozzle.
- The firmware for both machines is based on the Marlin Firmware. This baseline firmware is altered in a different manner for it to work on the respective machines. Potentially there is a difference in the interpretation of (some of the) g-code commands.

Although none of the above mentioned differences between the Prusa and Creality machines seems convincing in explaining the significant difference in shrinkage magnitudes on their own, these factors can also not be excluded as potential contributors. As it was deemed to be out the scope of the current study, no further investigation into this shrinkage discrepancy has been done. Future research might focus on the fundamental principles that cause this discrepancy between the two machines. Moreover, a comparative study on this effect could be performed in which more types and brands of FFF printers are included.

References

- [1] A.R. Rajkumar and K. Shanmugam. Additive manufacturing-enabled shape transformations via fff 4d printing. *Journal of Materials Research*, 33(24):4362–4376, 2018.
- [2] Q. Zhang, D. Yan, K. Zhang, and G. Hu. Pattern transformation of heat-shrinkable polymer by three-dimensional (3d) printing technique. *Sci Rep*, 5:8936, 2015.
- [3] Q. Zhang, K. Zhang, and G. Hu. Smart three-dimensional lightweight structures triggered from a thin composite sheet via 3d printing technique. *Sci Rep*, 6:22431, 2016.
- [4] Y. Wang and X. Li. An accurate finite element approach for programming 4d-printed self-morphing structures produced by fused deposition modeling. *Mechanics of Materials*, 151:103628, 2020.
- [5] T. van Manen, S. Janbaz, and A.A. Zadpoor. Programming 2d/3d shape-shifting with hobbyist 3d printers. *Materials Horizons*, 4(6):935–1202, 2017.
- [6] L. Kačergis, R. Mitkus, and M. Sinapius. Influence of fused deposition modeling process parameters on the transformation of 4d printed morphing structures. *Smart Materials and Structures*, 28:105042, 2019.
- [7] B. An, Y. Tao, J. Gu, T. Cheng, X. Chen, X. Zhang, W. Zhao, Y. Do, S. Takahashi, H. Wu, T. Zhang, and L. Yao, editors. *Telemorph: Democratizing 4D Printing of Self-Folding Materials and Interfaces*, CHI Conference on Human Factors in Computing Systems, Montréal, QC, Canada, 2018. Association for Computing Machinery.

ID	Strain 1-4	Strain 4-5	Strain 5-8	Strain 8-1	Average shrinkage axial	Average shrinkage transverse
TS1	0.090	0.065	0.091	0.065	0.091	0.065
TS2	0.089	0.058	0.093	0.055	0.091	0.056
TS3	0.073	0.050	0.072	0.055	0.073	0.053
TS4	0.009	0.023	0.009	0.023	0.009	0.023
TS5	0.006	0.020	0.008	0.025	0.007	0.023
TS6	0.006	0.030	0.009	0.025	0.007	0.028
TS1.5	0.111	0.093	0.111	0.113	0.111	0.103
TS7	0.164	0.078	0.108	0.073	0.136	0.076
TS8	0.126	0.075	0.107	0.080	0.117	0.078
TS9						
TS10	0.048	0.040	0.049	0.063	0.048	0.051
TS11	0.075	0.060	0.076	0.063	0.076	0.061
TS12	0.082	0.068	0.081	0.070	0.082	0.069
TS13	0.089	0.073	0.088	0.075	0.088	0.074
TS14	0.124	0.030	0.110	0.036	0.117	0.033
TS42						
TS52						
TS62						
TS15	0.100	0.110	0.108	0.110	0.104	0.110
TS152	0.154	0.157	0.140	0.160	0.147	0.158
TS16	0.077	0.070	0.077	0.073	0.077	0.071
TS162	0.127	0.101	0.129	0.085	0.128	0.093
TS17	0.096	0.078	0.097	0.085	0.097	0.081
TS172	0.139	0.143	0.148	0.140	0.143	0.141
TS18	0.075	0.068	0.076	0.068	0.076	0.068
TS182	0.121	0.108	0.111	0.108	0.116	0.108
TS19	0.075	0.072	0.077	0.078	0.076	0.075
TS192	0.149	0.121	0.132	0.098	0.140	0.109
TS20	0.010	0.008	0.011	0.010	0.010	0.009
TS21	0.037	0.030	0.037	0.033	0.037	0.031
TS22	0.067	0.050	0.069	0.057	0.068	0.054
TS23						
TS24	0.143	0.155	0.147	0.155	0.145	0.155
TS232	0.062	0.060	0.068	0.068	0.065	0.064
TS242	0.093	0.077	0.102	0.080	0.098	0.079
TS27	0.170	0.164	0.184	0.166	0.177	0.165
TS28	0.052	0.045	0.055	0.043	0.054	0.044
TS25	0.123	0.108	0.121	0.145	0.122	0.126
HB1	0.110	0.083	0.108	0.082	0.109	0.083
HB2	0.000	0.003	0.000	-0.003	0.000	0.000
TS1.52	0.078	0.151	0.089	0.148	0.084	0.150
TS2.5	0.095	0.158	0.101	0.180	0.098	0.169
TS3.5	0.075	0.125	0.066	0.146	0.070	0.136
FS1	0.205	0.043	0.190	0.033	0.198	0.038
FS2	0.205	0.083	0.209	0.025	0.207	0.054
FS3	0.212	0.025	0.199	0.043	0.206	0.034
FS4	0.253	0.055	0.242	0.068	0.247	0.062
FS5	0.258	0.030	0.241	0.058	0.250	0.044
FS6	0.245	0.063	0.245	0.048	0.245	0.055
TS26						
TS263						
TS262						
Layer test	0.210	0.020	0.216	0.043	0.213	0.031
	Strain L1	Strain L2	Strain L3	Strain L4	Strain L5	Strain L6
BP1	0.021	0.050	0.069	0.079	0.075	0.081
BP2	0.015	0.041	0.064	0.075	0.077	0.070
BP3						
BP4	0.029	0.053	0.071	0.079	0.085	0.082
BP5	0.038	0.054	0.067	0.076	0.084	0.081
BP6						
BP7						
BP8	0.078	0.042	0.053			
BP9	0.097	0.052	0.073			
BP3.5						
BP6.5	0.042	0.058	0.068	0.074	0.080	0.082
BP4.5						
BP5.5						
BP6.52	0.052	0.059	0.062	0.063	0.067	0.072
BP10	0.085					
BP11	0.094					
BP12	0.104					
BP13	0.080					
BP14						
BP15	0.024					
BP152	0.071					
BP16						

Table 2: Overview of the results of the performed preliminary tests.

Appendix F: X-Ray Diffraction diffractograms

For determination of the crystallinity fraction as presented in chapter 3, all samples are analysed by the X-ray diffraction (*XRD*) technique. The crystallinity fractions are calculated based on the resulting diffractograms of each sample. These diffractograms are shown in this appendix. The diffractograms are generated with a Bruker D8 Advance diffractometer (Bruker Corporation, Billerica, MA, USA). The settings that are used in the analysis can be found in chapter 3. The XRD data is evaluated in the Bruker DIFFRAC.EVA software. The crystalline phases are extracted from the data by using the ICDD pdf4 database (International Centre For Diffraction Data, Newtown Square, PA, USA).

A total of 13 samples is analysed by the XRD technique. The samples are assigned a unique sample number each, going from XTS1 to XTS13. Each sample has a variation in a single design parameter with respect to the default sample design as presented in chapter 3. The parameters that are varied are the heating time T_a and the printing speed V_p . The varied parameter per sample and its assigned value is shown in table 1. Moreover, in this table it is indicated whether the sample is constrained during heating in the oven. A motivation for sample constraining during oven heating can be found in chapter 3. In table 1 it is also indicated to what sample set of chapter 3 each sample belongs.

Table 1: The variations for each sample.

Sample:	XTS1	XTS2	XTS3	XTS4	XTS5	XTS6	XTS7	XTS8	XTS9	XTS10	XTS11	XTS12	XTS13
Varied parameter:	T_a	T_a	T_a	T_a	T_a	V_p	V_p	V_p	V_p	V_p	V_p	V_p	V_p
Parameter value:	0 s	20 s	300 s	1800 s	3600 s	1 mm/s	30 mm/s	60 mm/s	90 mm/s	1 mm/s	30 mm/s	60 mm/s	90mm/s
Constrained:	No	No	No	No	No	No	No	No	No	Yes	Yes	Yes	Yes
	set 3					set 1				set 2			

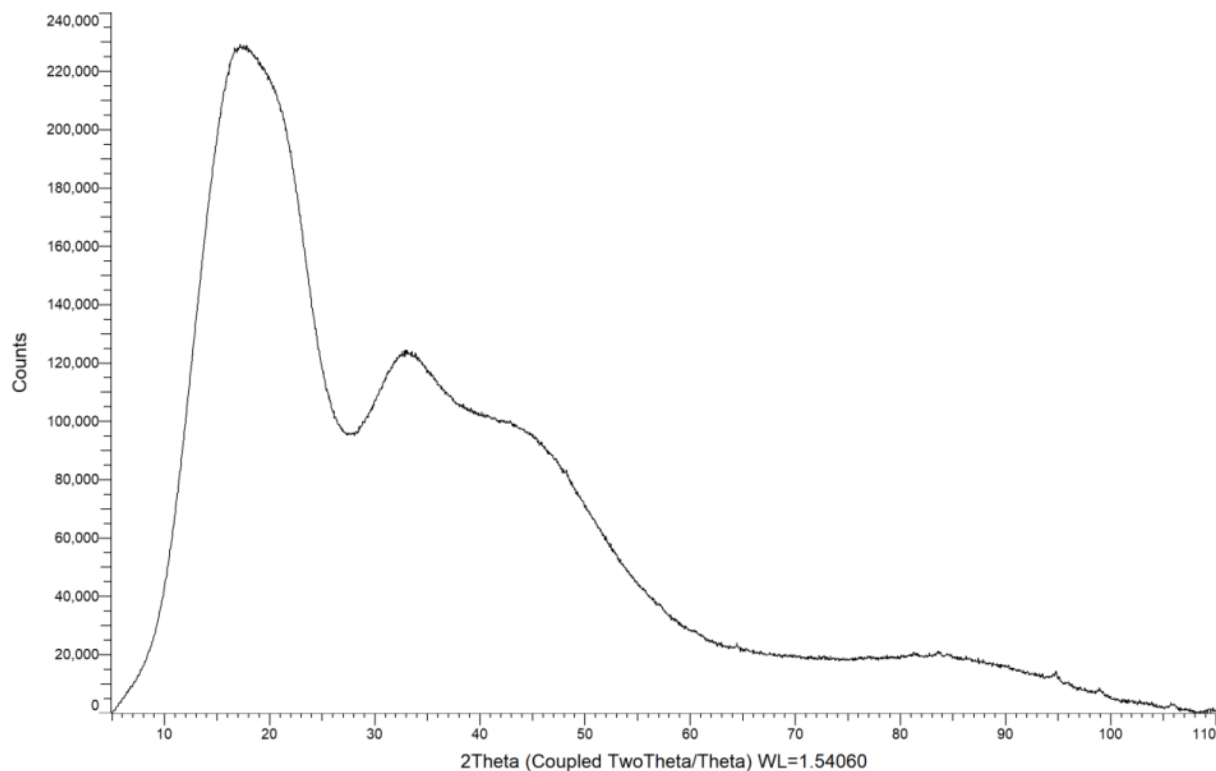


Figure 1: XRD results for sample XTS1.

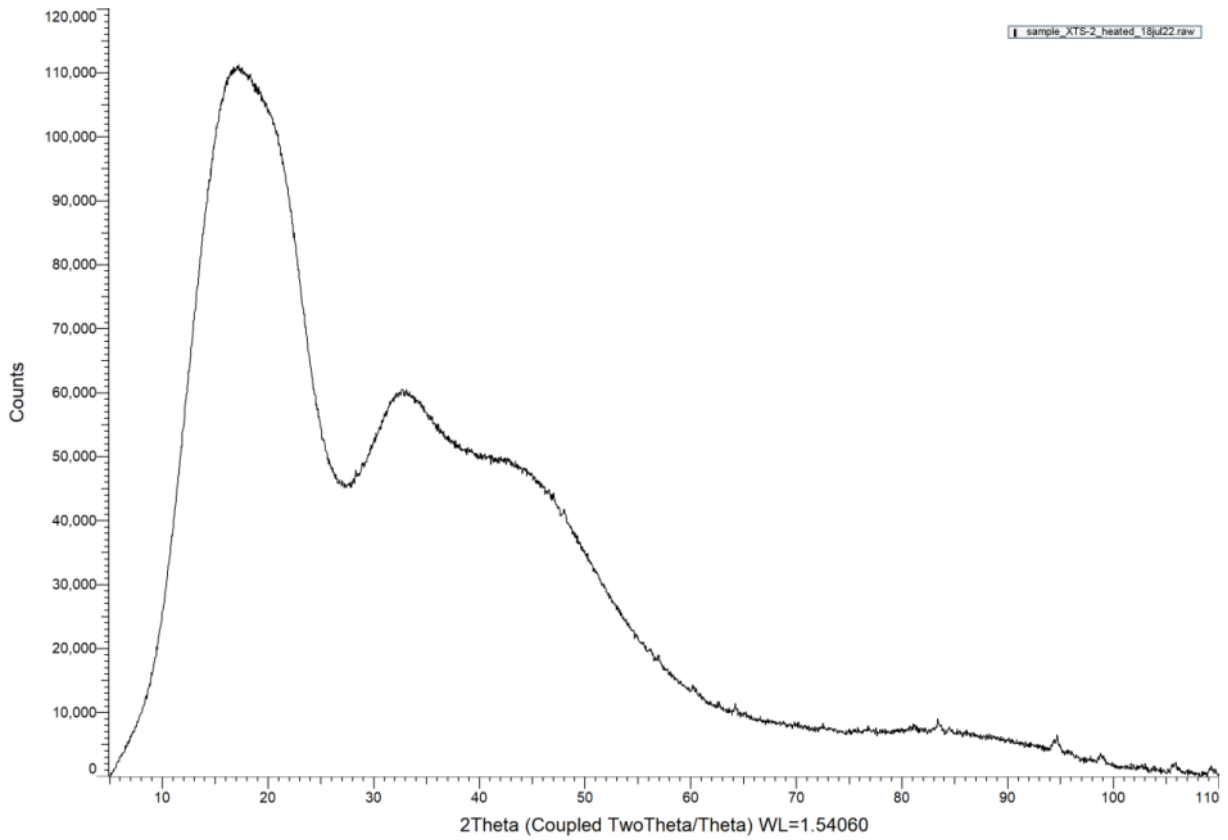


Figure 2: XRD results for sample XTS2.

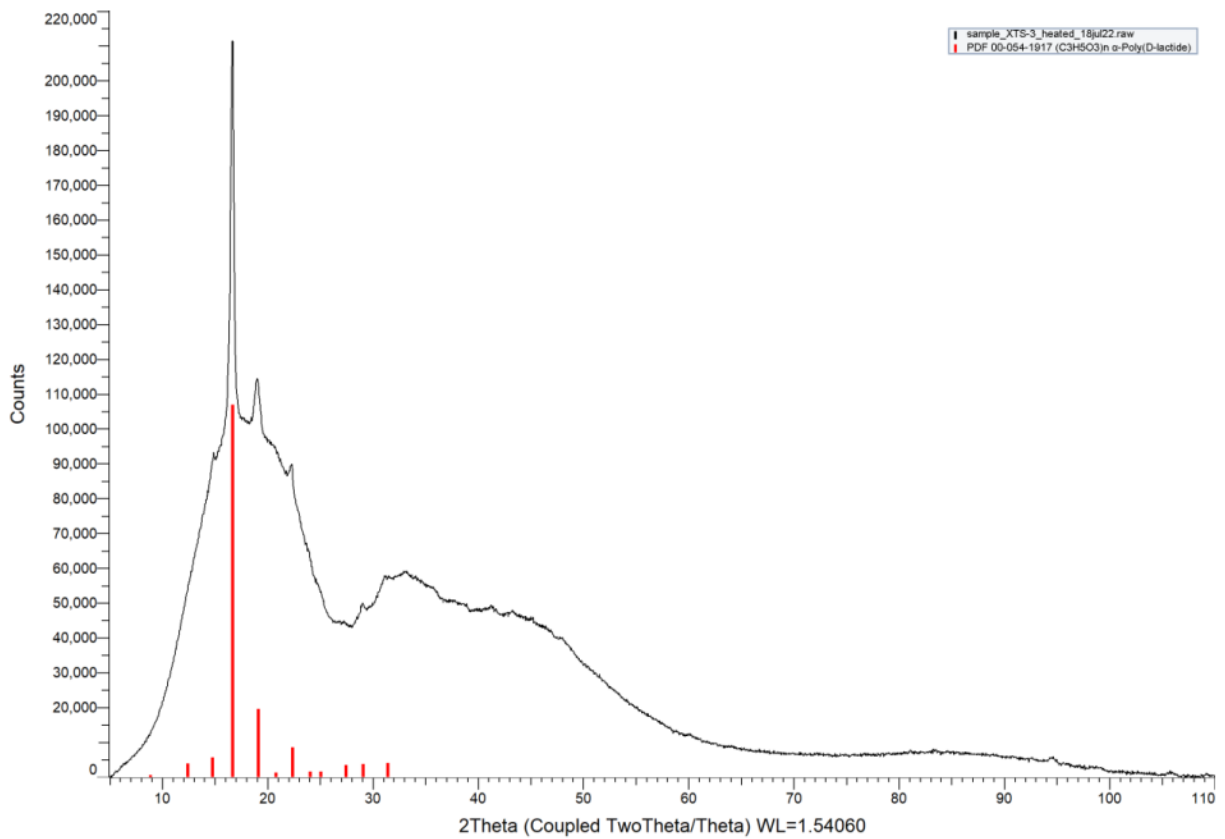


Figure 3: XRD results for sample XTS3.

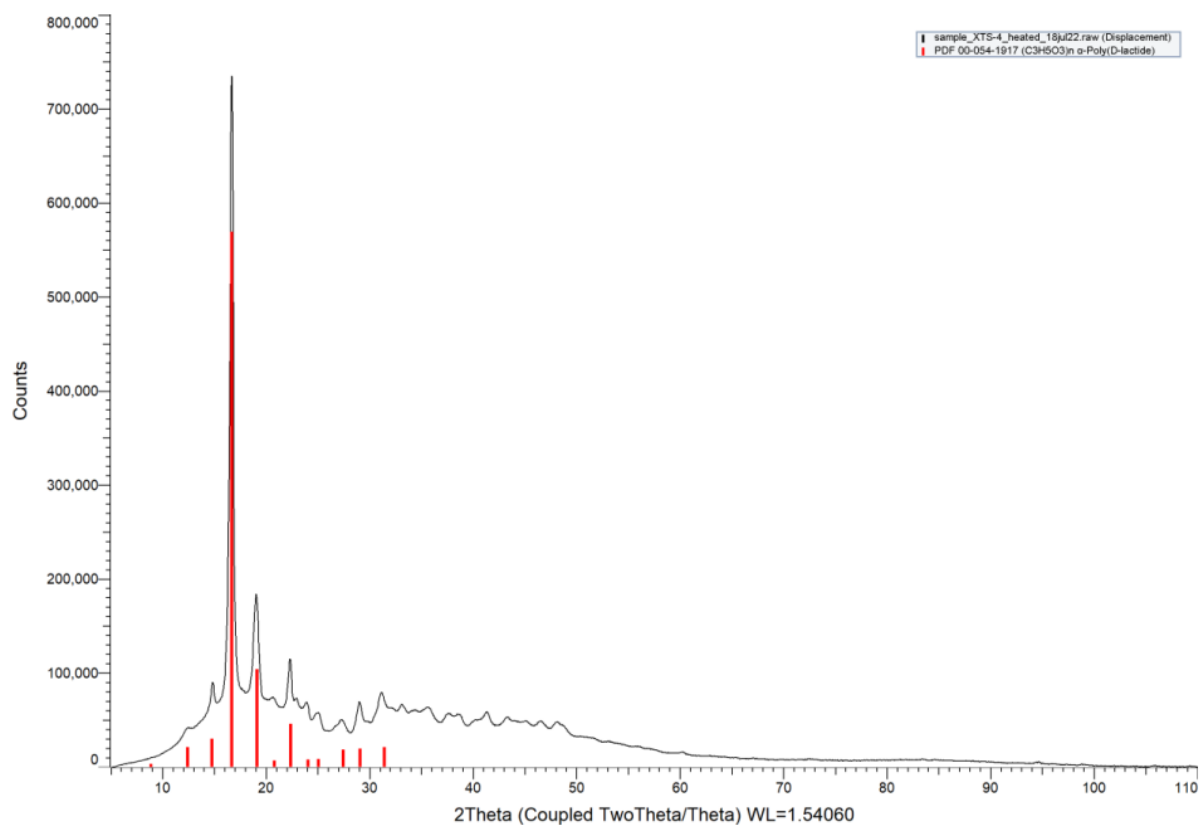


Figure 4: XRD results for sample XTS4.

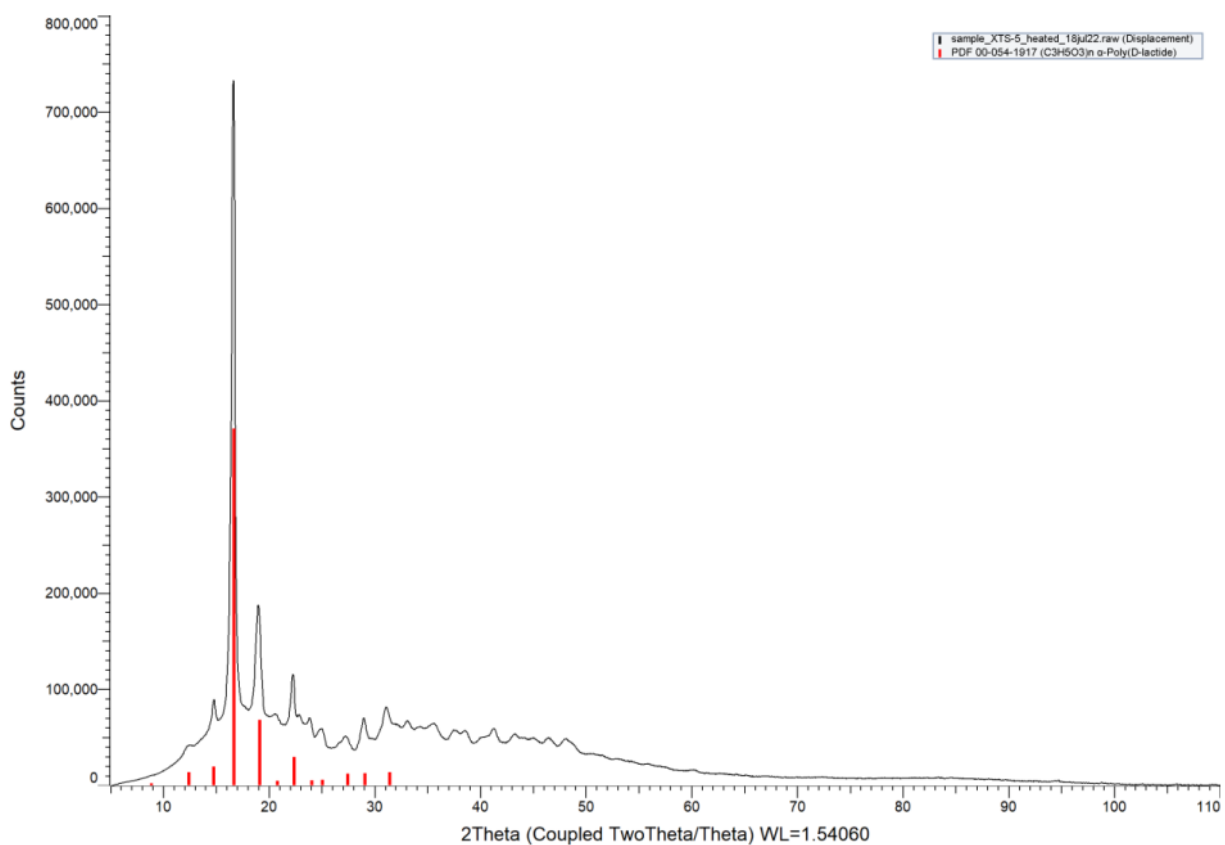


Figure 5: XRD results for sample XTS5.

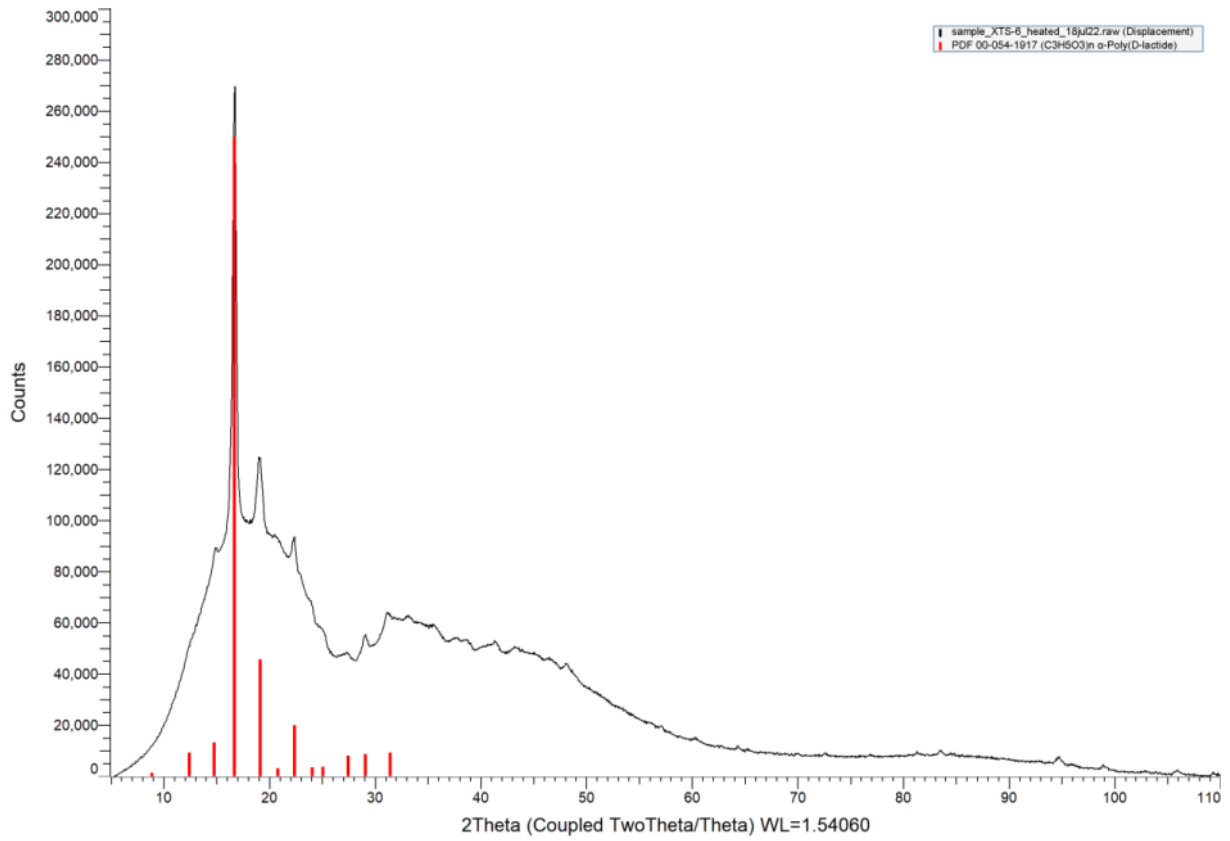


Figure 6: XRD results for sample XTS6.

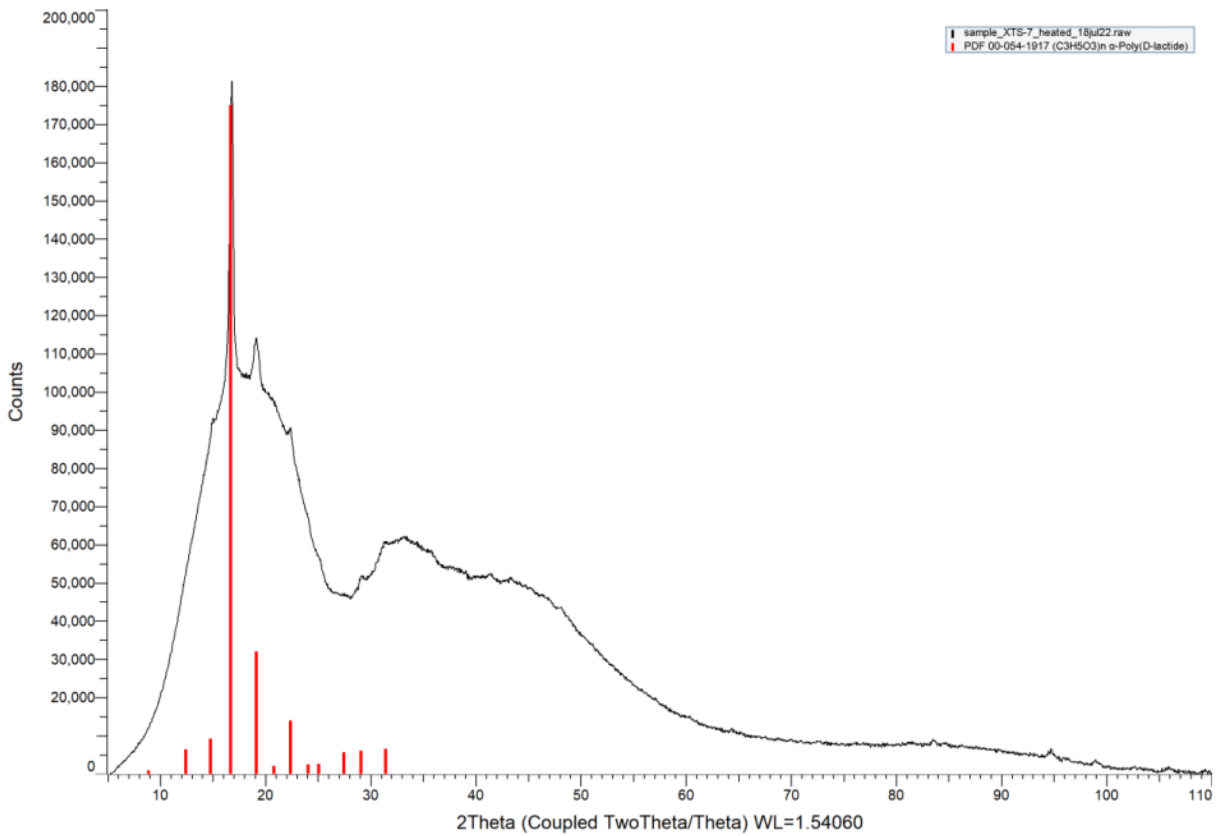


Figure 7: XRD results for sample XTS7.

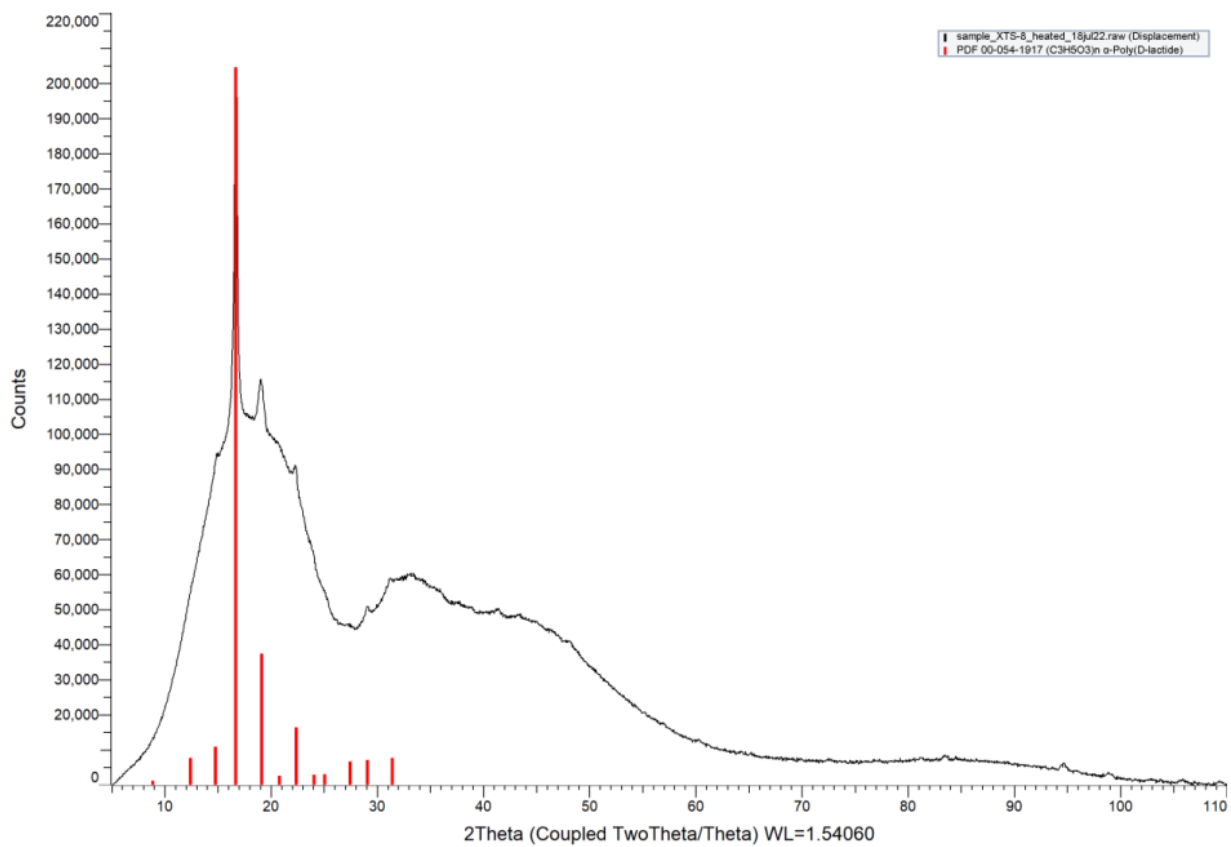


Figure 8: XRD results for sample XTSS.

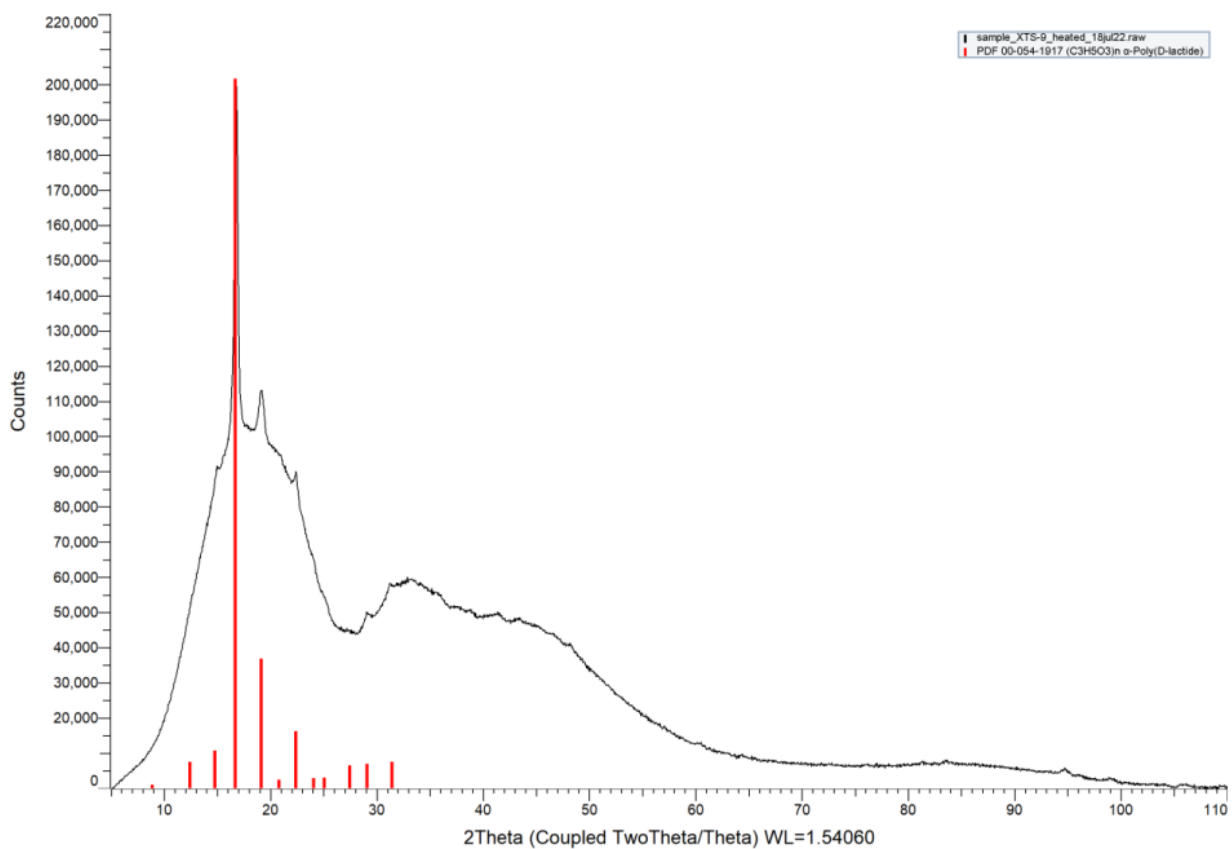


Figure 9: XRD results for sample XTS9.

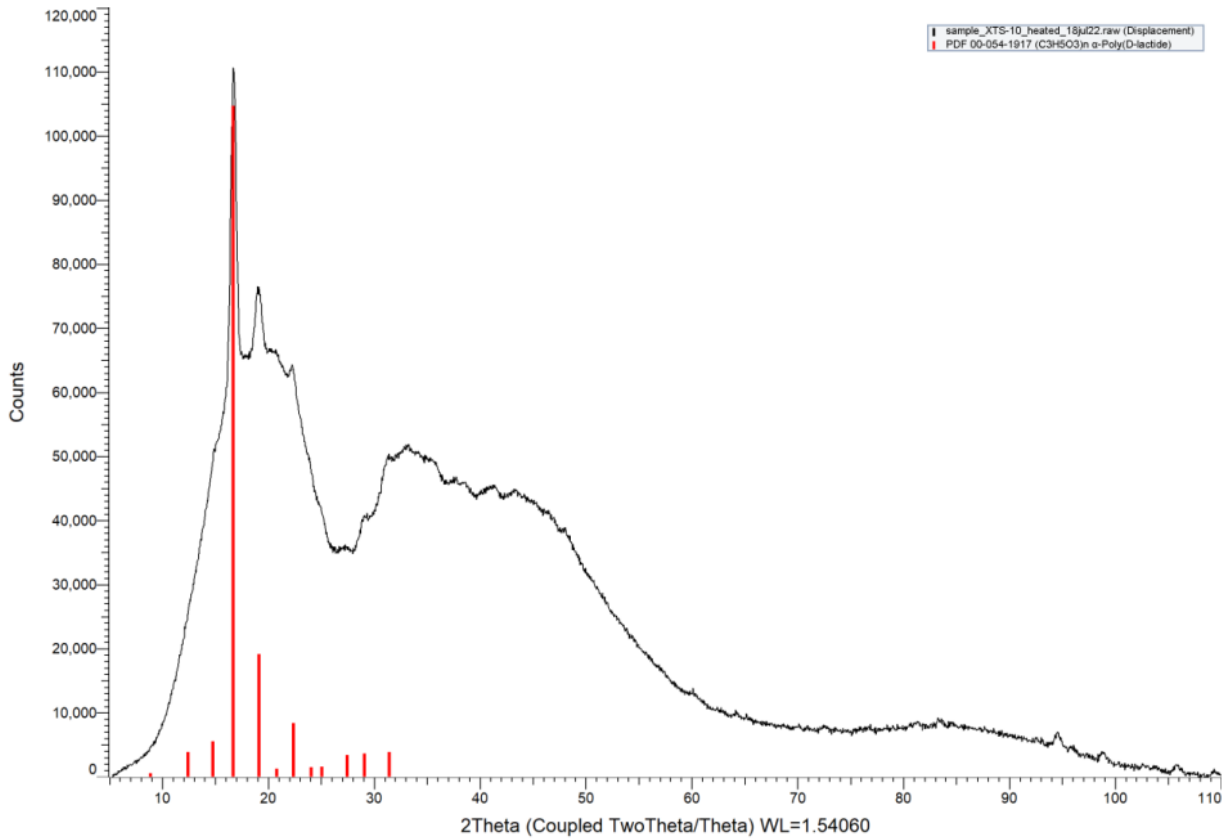


Figure 10: XRD results for sample XTS10.

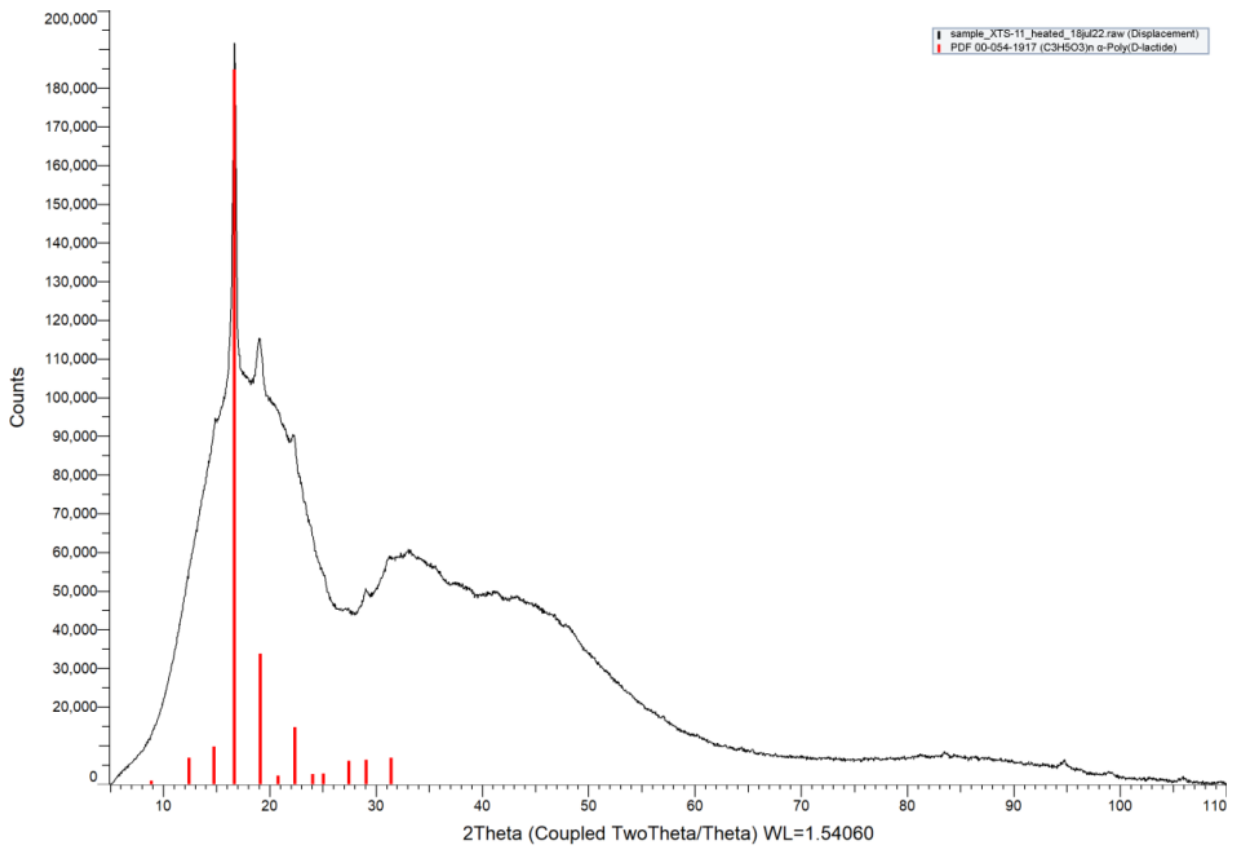


Figure 11: XRD results for sample XTS11.

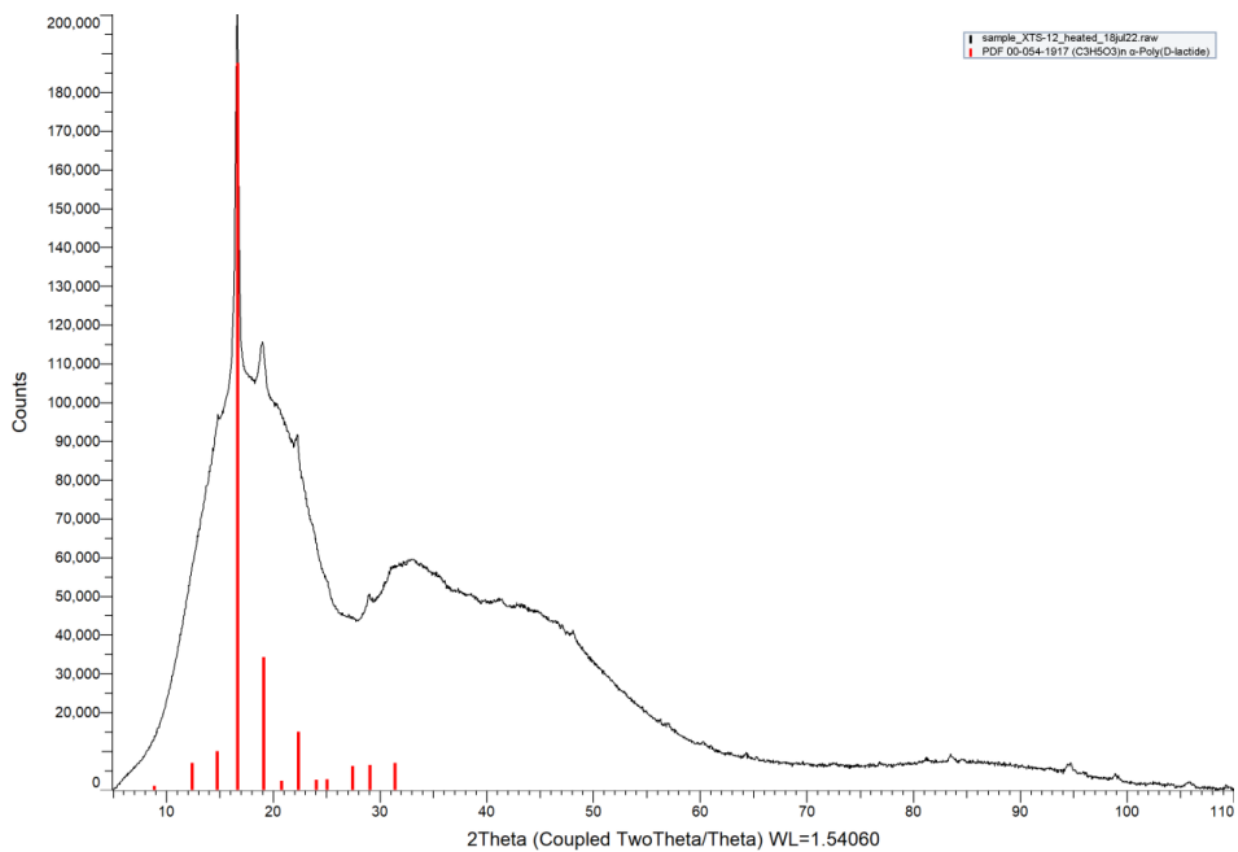


Figure 12: XRD results for sample XTS12.

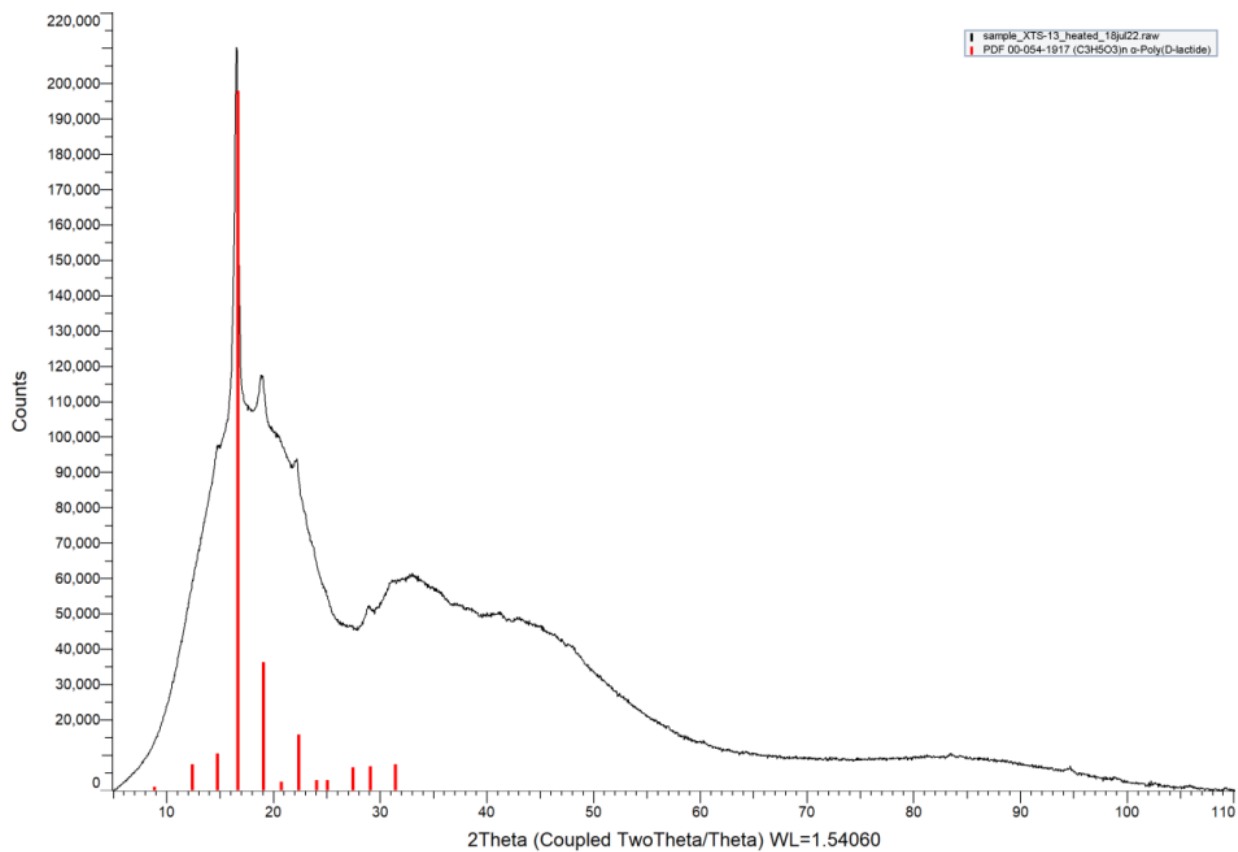


Figure 13: XRD results for sample XTS13.

Based on the diffractograms the crystallinity for each sample is determined with the DIFFRAC.EVA software. Uncertainty on these values is $\pm 0.5\%$. The results of this are shown in table 2.

Table 2: The crystallinity fraction per sample.

Sample:	XTS1	XTS2	XTS3	XTS4	XTS5	XTS6	XTS7	XTS8	XTS9	XTS10	XTS11	XTS12	XTS13
Crystallinity:	0%	0%	3%	19%	18%	5%	2%	3%	2%	3%	3%	4%	3%
	set 3					set 1				set 2			